



A HIGH PERFORMANCE CLOSED-LOOP ANALOG READOUT CIRCUIT FOR  
CAPACITIVE MEMS ACCELEROMETERS

A THESIS SUBMITTED TO  
THE GRADUATE SCHOOL OF NATURAL AND APPLIED SCIENCES  
OF  
MIDDLE EAST TECHNICAL UNIVERSITY

BY

YUNUS TERZİOĞLU

IN PARTIAL FULFILLMENT OF THE REQUIREMENTS  
FOR  
THE DEGREE OF MASTER OF SCIENCE  
IN  
ELECTRICAL AND ELECTRONICS ENGINEERING

SEPTEMBER 2015



Approval of the thesis:

**A HIGH PERFORMANCE CLOSED-LOOP ANALOG READOUT CIRCUIT  
FOR CAPACITIVE MEMS ACELEROMETERS**

submitted by **YUNUS TERZIOĞLU** in partial fulfillment of the requirements for the degree of **Master of Science in Electrical and Electronics Engineering Department, Middle East Technical University** by,

Prof. Dr. Gülbin Dural Ünver  
Dean, Graduate School of **Natural and Applied Sciences**

\_\_\_\_\_

Prof. Dr. Gönül Turhan Sayan  
Head of Department, **Electrical and Electronics Eng.**

\_\_\_\_\_

Prof. Dr. Tayfun Akın  
Supervisor, **Electrical and Electronics Eng. Dept., METU**

\_\_\_\_\_

**Examining Committee Members**

Prof. Dr. Haluk Külâh  
Electrical and Electronics Eng. Dept., METU

\_\_\_\_\_

Prof. Dr. Tayfun Akın  
Electrical and Electronics Eng. Dept., METU

\_\_\_\_\_

Assist. Prof. Dr. Kıvanç Azgın  
Mechanical Eng. Dept., METU

\_\_\_\_\_

Assist. Prof. Dr. Mehmet Ünlü  
Electrical and Electronics Eng. Dept., YBU

\_\_\_\_\_

Assist. Prof. Dr. Mahmud Yusuf Tanrıku  
Electrical and Electronics Eng. Dept., ADANA STU

\_\_\_\_\_

**Date:**

\_\_\_\_\_

**I hereby declare that all information in this document has been obtained and presented in accordance with academic rules and ethical conduct. I also declare that, as required by these rules and conduct, I have fully cited and referenced all referenced material and results that are not original to this work.**

Name, Surname : Yunus Terziođlu

Signature :

# ABSTRACT

## A HIGH PERFORMANCE CLOSED-LOOP ANALOG READOUT CIRCUIT FOR CAPACITIVE MEMS ACCELEROMETERS

Terzioğlu, Yunus

M.S., Department of Electrical and Electronics Engineering

Supervisor: Prof. Dr. Tayfun Akın

September 2015, 135 pages

In this thesis, a closed-loop analog readout circuit for capacitive MEMS accelerometers is introduced. The detailed analysis of the dynamics of the proposed accelerometer is presented along with the associated simulation models. The theoretical investigation of each building block of the accelerometer is also presented in detail and supported by the corresponding formulas. The implemented accelerometer is shown to satisfy the estimated performance parameters with measurements conducted using various test setups. Moreover, two different multi-axis accelerometer applications, which are realized using the proposed readout circuit, are presented as well. The functionality of these two methods are verified with additional tests.

The test results showed that  $5.5 \mu\text{g}/\sqrt{\text{Hz}}$  noise floor,  $5.4 \mu\text{g}$  bias instability,  $0.2 \text{ mg}$  bias repeatability, and  $\pm 35 \text{ g}$  operation range is achieved with the proposed accelerometer.

Keywords: MEMS, Accelerometer, Capacitive, Analog, Readout Circuit, Closed-Loop, High Performance, Modelling, Analysis

# ÖZ

## SIĞASAL MEMS İVMEÖLÇERLER İÇİN YÜKSEK PERFORMANSLI KAPALI DÖNGÜ ANALOG OKUMA DEVRESİ

Terzioğlu, Yunus

Yüksek Lisans, Elektrik ve Elektronik Mühendisliği Bölümü

Tez Yöneticisi: Prof. Dr. Tayfun Akın

Eylül 2015, 135 sayfa

Bu tezde sığasal MEMS ivmeölçerler için tasarlanmış kapalı döngü bir analog okuma devresi sunulmaktadır. Önerilen ivmeölçerin dinamiklerinin detaylı analizi, simülasyon modelleri ile birlikte gösterilmiştir. Sunulan ivmeölçeri oluşturan her bir yapı taşının kuramsal incelenmesi detaylı olarak yapılmış ve ilgili bağıntılarla desteklenmiştir. Gerçeklenen ivmeölçerin performans parametreleri çeşitli test düzenekleri kullanılarak ölçülmüş ve bu parametrelerin üretim öncesi beklenen değerlerde oldukları saptanmıştır. Ayrıca, önerilen okuma devresi kullanılarak gerçekleştirilen iki ayrı çok eksenli ivmeölçer uygulaması sunulmuş ve bu uygulamaların işlevselliği de yine ölçüm sonuçlarıyla doğrulanmıştır.

Ölçüm sonuçlarına göre gerçekleştirilen ivmeölçerin gürültü seviyesi  $5.5 \mu\text{g}/\sqrt{\text{Hz}}$ ; offset kararsızlığı  $5.4 \mu\text{g}$ ; offset tekrarlanabilirliği  $0.2 \text{ mg}$ ; ve ölçüm aralığı  $\pm 35 \text{ g}$  olarak tespit edilmiştir.

Anahtar Kelimeler: MEMS, İvmeölçer, Sığasal, Analog, Okuma Devresi, Kapalı Döngü, Yüksek Performans, Modelleme, Analiz

*To whom,  
who cares.*

## ACKNOWLEDGEMENTS

First of all, I would like to thank my thesis advisor Prof. Dr. Tayfun Akın for his support, understanding, and guidance during my graduate studies.

I would also like to thank Dr. Said Emre Alper and Assist. Prof. Kıvanç Azgın for their support as perfect technical advisors who always show a positive attitude about non-technical topics as well. Their lead is one of the biggest contributors and motivation sources of this study.

I would like to thank every member of METU-MEMS family for creating a family-like environment in which I did not feel alone a second. Among this family, I would specially like to thank Gülşah Demirhan, Ozan Ertürk, Hasan Doğan Gavcar, Başak Kebapçı, and Ferhat Yeşil for their friendship. Additionally I would like to thank former METU-MEMS members Tunjar Askarlı, Burak Eminoğlu, Soner Sönmezoğlu and Onur Yalçın for their great support in the early periods of my M.Sc studies and on.

I could not thank enough to my very special friends Sırma Örgüç, Ulaş Aykutlu, Efecan Bozulu, Talha Köse, Yunus Şener, Gamze Tanık, Emre Topçu, Mesut Uğur. Words are not enough to describe how lucky I am to have met all of these people.

And above all, I would like to thank my family Münevver, Yağmur and Kadir Terzioğlu for their endless support and love throughout my life.

# TABLE OF CONTENTS

ABSTRACT.....	v
ÖZ .....	vi
ACKNOWLEDGEMENTS .....	viii
TABLE OF CONTENTS .....	ix
LIST OF FIGURES .....	xiii
LIST OF TABLES .....	xx
CHAPTERS	
1. INTRODUCTION .....	1
1.1. Important Definitions .....	2
1.2. Overview of MEMS Accelerometers .....	4
1.3. Thesis Objectives and Organization .....	6
2. CLOSED-LOOP ANALOG ACCELEROMETER READOUT THEORY .....	9
2.1. Properties of the MEMS Sensing Element.....	10
2.2. Capacitive Sensing Interface .....	16
2.2.1. Differential Sensing and Capacitive Pre-Amplification .....	16
2.2.2. Signal Rectification by Demodulation and Low-Pass Filtering.....	21
2.2.3. An Open-Loop Analog Accelerometer Readout Circuit.....	23
2.3. Closed-Loop Accelerometer Operation Principles.....	25
2.3.1. Capacitive Actuation .....	28
2.3.2. Differential, Bidirectional Capacitive Actuation .....	30
2.3.3. Electrostatic Spring Effect and the Operation Range Estimation .....	32

2.3.4.	Operation Range Considerations.....	35
2.4.	Simultaneous Differential Sensing and Force-Feedback.....	37
2.4.1.	Simultaneous Sensing and Force-Feedback with a Single Electrode Set .....	38
2.5.	Summary and Conclusions .....	41
3.	SYSTEM-LEVEL DESIGN AND MODELLING .....	43
3.1.	Design and Modelling of the Building Blocks .....	43
3.1.1.	Non-linear Model of the Sensing Element.....	44
3.1.2.	Open-Loop Readout Electronics .....	48
3.2.	Model Linearization .....	50
3.2.1.	Linear Model of the Sensor .....	50
3.2.2.	Linear Model of the Open-Loop Readout Electronics .....	51
3.3.	Controller Considerations.....	53
3.3.1.	Controller Design Approach .....	54
3.3.2.	Controller Design and Stability Analysis.....	56
3.4.	System Level Transient Simulations .....	62
3.4.1.	Open-Loop Accelerometer .....	62
3.4.2.	Closed-Loop Accelerometer .....	65
3.5.	Summary and Conclusions .....	68
4.	CIRCUIT LEVEL DESIGN AND MODELLING .....	71
4.1.	Design of the Electrical Blocks .....	71
4.1.1.	Front-End Electronics .....	72
4.1.2.	Demodulator and Low-Pass Filter.....	74
4.1.3.	PI-Controller.....	75
4.1.4.	Voltage Feedback Topology .....	76
4.1.5.	Voltage Regulation.....	78

4.2.	SPICE Model.....	79
4.2.1.	Front-End Electronics .....	80
4.2.2.	Demodulator and Low-Pass Filter .....	81
4.2.3.	PI-Controller .....	82
4.2.4.	Behavioral Model of the Sensing Element.....	83
4.2.5.	The Complete Accelerometer in SPICE .....	84
4.3.	Electromechanical Noise Analysis .....	86
4.3.1.	Front-End Electronics .....	88
4.3.2.	Low-Pass Filter and the PI-Controller .....	90
4.3.3.	Additional Noise sources .....	91
4.3.4.	Overall Referred-to-Input Noise .....	92
4.4.	Performance Estimation .....	93
4.5.	Summary .....	93
5.	IMPLEMENTATION AND TEST RESULTS .....	95
5.1.	Hybrid-Platform Package Implementation.....	96
5.2.	Interface Circuitry and Auxiliary Tools .....	99
5.2.1.	Test PCB .....	100
5.2.2.	Data Acquisition and Test Automation.....	102
5.2.3.	Rotary Table.....	103
5.2.4.	Shaker Table.....	104
5.3.	Circuit Functionality Tests .....	104
5.4.	Sensor Undercut Characterization.....	105
5.5.	Test Results .....	109
5.5.1.	Power-Up .....	110
5.5.2.	Scale Factor, Off-set and Range.....	111
5.5.3.	Linearity .....	112

5.5.4. Velocity Random Walk and Bias Instability .....	113
5.5.5. Bias Repeatability .....	114
5.6. Summary and Conclusions .....	115
6. FURTHER APPLICATIONS USING AFFRO .....	117
6.1. A Single-Proof Mass, Two-Axis Accelerometer.....	117
6.2. An Out-of-Plane Accelerometer and a New Concept of Hybrid Electrodes... .....	120
6.3. Summary.....	125
7. CONCLUSIONS AND FUTURE WORK .....	127
REFERENCES.....	131

# LIST OF FIGURES

## FIGURES

Figure 2.1: The Scanning Electron Microscope (SEM) image of lower-right quadrant of the sensing element used in the proposed work.....	10
Figure 2.2: The simplified diagram and the equivalent electrical model of the sensing element. Even though the mechanical structure is fully symmetrical, the two electrodes ( $E_p$ , $E_n$ ) and the capacitances ( $C_p$ , $C_n$ ) are denoted as ‘positive’ and ‘negative’ for convenience. Note that the PM node in the electrical model can be visualized as if it can move up and down, changing the parallel plate capacitances of $C_p$ and $C_n$ differentially.....	11
Figure 2.3: The plot demonstrating the relation between the applied acceleration and the capacitance difference between the two complementary electrode capacitances of a typical capacitive accelerometer. Notice the non-linear behavior. ....	15
Figure 2.4: The simplified circuit diagram demonstrating the modulation of the capacitances of the two electrodes and the front end electronics. ‘ $C_p$ ’ and ‘ $C_n$ ’ are the two differential capacitances of the sensing element; ‘PM’ is the proof mass of the sensor; and ‘ $v_{ac}$ ’ is the carrier signal. The operational amplifier G is configured as a capacitive transimpedance amplifier (TIA) for pre-amplification. This stage is followed by a passive high-pass filter, $H(s)$ , and a voltage buffer.....	17
Figure 2.5: A visual summary of the front-end electronics based on non-quantitative sample waveforms. $v_{ac}(t)$ is the carrier signal; $a(t)$ is the applied acceleration; $\Delta C(t)$ is the capacitance difference between the two electrode capacitances; and $v_{fe}(t)$ is the front-end electronics output. ....	20
Figure 2.6: The simplified block diagram demonstrating the demodulation and low-pass filtering steps. The dashed box includes a comparator and a multiplier which basically summarizes the operation of the switching demodulator used in the proposed system.....	21
Figure 2.7: The block diagram of the circuit forming an open-loop accelerometer. .	23

Figure 2.8: The simplified block diagram of the linearized closed-loop, force-balancing capacitive accelerometer in Laplace domain. The blocks in the dashed box are directly related with the electromechanical nature of the MEMS capacitive sensing element. .... 25

Figure 2.9: A demonstration of the electrostatic forces between the two plates of a parallel-plate capacitor. .... 28

Figure 2.10: Simplified electromechanical model of the sensing element demonstrating the application of force-feedback voltages. The feedback voltage  $V_{FB}$  is applied onto the sensor electrodes differentially, accompanied by a fixed DC voltage,  $V_{PM}$ . By using such a configuration, the force-feedback action can be linearized and the acceleration can be counteracted in both directions. The force exerted on the proof mass in  $x$  direction by an external acceleration is counteracted by decreasing the  $V_{FB}$  voltage below zero. Oppositely, if the force by acceleration is applied in  $-x$  direction, then  $V_{FB}$  voltage is increased above zero. .... 30

Figure 2.11: Visual representation of the electrostatic spring softening effect. The slopes of each line at the origin ( $x=0$ ) are equal to the corresponding spring constants. Note that beyond points  $q'$  and  $-q'$ , the net force acting on the proof mass changes its signature indicating a pull-in situation. .... 35

Figure 2.12: Continuous-time, closed-loop accelerometer approach incorporating two sets of differential electrodes. In this configuration, the electrode set composed of  $C_{F,p}$  and  $C_{F,n}$  is used for electrostatic force-feedback while the other set is used for acceleration sensing. .... 37

Figure 2.13: A conceptual circuit diagram for the analog force-feedback accelerometer. By using such a configuration to apply both sensing and feedback voltages on the electrodes, simultaneous differential sensing and force-feedback can be achieved in continuous-time using only one pair of differential electrodes. .... 38

Figure 3.1: The non-linear model of the sensing element (dashed box). The input acceleration is in 'g' units. The two function blocks include non-linear functions of the applied electrostatic forces (Voltage-to-Force) and the capacitance difference between the two electrodes (Displacement-to-deltaC). Output of the sensor is taken as the capacitance difference,  $\Delta C$ , between the two differential electrodes. .... 44

Figure 3.2: The amplitude of residual oscillations of the proof mass as a result of unit amplitude carrier signal under varying frequencies. After the carrier signal frequency exceeds ~20 kHz, the amplitude of the oscillations shrink significantly. ....	46
Figure 3.3: (a) Unit step and (b) ramp responses of the non-linear sensing element model. Output of the system is the capacitance difference between the two electrodes, $\Delta C$ , and the input is acceleration in ‘g’ units. The oscillations on the output are a result of mass residual motion caused by the 20 kHz carrier signal. ....	48
Figure 3.4: The Simulink model of the open-loop readout electronics. ....	48
Figure 3.5: The linearized model of the sensing element (dashed box). ....	51
Figure 3.6: Comparison of the unit step responses of the linearized and the non-linear models of the sensing element. ....	51
Figure 3.7: The linearized envelope model of the open-loop readout electronics. ....	53
Figure 3.8: The comparison of the linearized and the actual model of the open-loop readout electronics. As it can be seen, the linearized model works with a very high accuracy. ....	53
Figure 3.9: Comparison of a sample system’s closed-loop step response for three different I-controller zero locations. Placing the controller zero further away from the plant’s pole (at 100 Hz) on either side causes the settling time to degrade. Additionally, as the zero frequency increases, the stability of the system degrades. Note that for better comparison of settling times, each of the responses are clipped once they are settled in an equal error band. ....	55
Figure 3.10: The linear closed-loop system model created in MATLAB Simulink environment. Note that even though the actual output of the circuit is ‘ $V_{FB}$ ’, using the ‘g output’ node as the output of the system eases the analysis of the system significantly. ....	57
Figure 3.11: (a) Bode plots of the plant and the controller for three different cases of $V_{FB}$ voltages. (b) Bode plots of the open-loop transfer function $H_{OL}(s)$ and the stability margins for all three cases. Note that the gain of the controller is to be tuned yet. ...	58
Figure 3.12: The step responses of the closed-loop system for three different cases of $V_{FB}$ voltage with a unity-gain PI-controller. ....	59

Figure 3.13: The bode plots of the open-loop system after the tuning of the PI-controller is completed. Note that the case where  $V_{FB}=5.5$  V is the worst case scenario for the stability of the system. .... 60

Figure 3.14: The demonstration of the closed-loop response of the system with the given controller parameters. It can be seen in the figure that the bandwidth of the system for all three cases is roughly above 100 Hz. .... 60

Figure 3.15: The step responses of the closed-loop system for all three different scenarios. Note that in the actual system, the peak values of the responses would not be as high as shown in this figure. .... 61

Figure 3.16: The non-linear model of the accelerometer which is used for the system-level simulations in open-loop configuration. .... 62

Figure 3.17: The step response of the accelerometer in open-loop configuration. The settled voltage output of the open-loop readout electronics shows the scale factor of the accelerometer is about 54 mV/g in open-loop configuration. .... 63

Figure 3.18: The demonstration of the pull-in occurring due to excessive amount of proof mass displacement into one direction in response to a ramp input. Note that if the proof mass voltage was not applied to the electrodes, the range would be higher at the cost of less readout gain thus the scale factor. .... 64

Figure 3.19: The ramp response of the accelerometer between -15 and +15 g. Notice the non-linearity due to the non-linear nature of the varying-gap electrode type structure of the sensing element. .... 64

Figure 3.20: Simulated chirp response of the accelerometer in open-loop configuration. -3 dB frequency of the accelerometer in open-loop configuration can be observed to be around 65 Hz by this simulation result. .... 65

Figure 3.21: The non-linear model of the accelerometer which is used for the system-level simulations in closed-loop configuration. .... 66

Figure 3.22: The simulated unit step response of the proposed closed loop accelerometer demonstrated along with the change in the proof mass displacement while the force balancing action takes place. .... 66

Figure 3.23: The ramp response of the proposed closed loop accelerometer in -35 to +35 g range. .... 67

Figure 3.24: The chirp response of the proposed closed loop accelerometer demonstrating the operation bandwidth. ....	67
Figure 3.25: The response of the closed-loop accelerometer to a high-g step input. It can be observed by this figure that, the percent overshoot is not as high as suggested by the linear model as expected. ....	68
Figure 4.1: The circuit schematic of the front-end readout electronics composed of a pre-amplifier, a passive high-pass filter and a voltage buffer. ....	72
Figure 4.2: The multiple-feedback type, second-order Butterworth low-pass filter as used in the implementation of the proposed accelerometer. ....	74
Figure 4.3: The topology of the PI-controller used in the implementation of the proposed circuit. ....	75
Figure 4.4: The topology, constructed using two instrumentation amplifiers, which generates the electrode waveforms in order to achieve simultaneous sensing and feedback using a single set of differential electrodes. ....	77
Figure 4.5: The supply network which is used to feed the proposed circuit. All of the capacitances are in $\mu\text{F}$ ; all of the resistances are in $\text{k}\Omega$ units. ....	79
Figure 4.6: The SPICE circuit diagram of the front-end electronics and its frequency response. ....	80
Figure 4.7: The behavioral model of the switching demodulator AD630 as supplied by the manufacturer, (a); and as created manually in SPICE, (b). ‘sq’ is a unit square wave generated based on the carrier signal, $v_{ac}$ , and it is multiplied by the output of the front-end electronics, $v_{fe}$ , to generate the demodulator output, $v_{demod}$ . ....	81
Figure 4.8: The simulation circuit and the frequency response of the low-pass filter used in the proposed system. -6 dB point of this second-order filter is slightly above 100 Hz. ....	82
Figure 4.9: The simulation circuit and the frequency response of the PI-controller used in the proposed system. The DC gain of the block is limited by the open-loop gain of the OpAmp. ....	83
Figure 4.10: The behavioral model of the sensing element created in SPICE environment. ....	84
Figure 4.11: The SPICE simulation circuit of the proposed accelerometer. ....	85

Figure 4.12: The demonstration of unit-g step responses of the Simulink and SPICE models in comparison. Note that a perfect fit between these responses are already not expected since certain simplifications are made dedicated to each model. .... 85

Figure 4.13: Major noise contributors of the proposed system demonstrated with the linearized closed-loop model. .... 86

Figure 4.14: Noise gains referring the three major noise contributors to the input of the closed-loop accelerometer. As constant multipliers, maximum values of these frequency dependent gains are used. .... 87

Figure 4.15: The electrical-noise circuit model of the front-end electronics. .... 89

Figure 4.16: The electrical-circuit noise model of the low-pass filter and the PI-controller. .... 90

Figure 5.1: The glass-substrate PCB layout used to interconnect all the electrical components of the proposed analog accelerometer. Dashed lines show the components, red solid lines show the wirebonds. Overall board dimensions are 1.45x2.15 cm. Note that ‘AFFRO’ stands for ‘Analog Force-Feedback ReadOut.’ ..... 97

Figure 5.2: The cross-sectional diagram of the hybrid-platform package in which the proposed accelerometer is constructed. .... 98

Figure 5.3: : A completed, ready-to-run analog accelerometer package. .... 98

Figure 5.4: The overview of the core test setup which is used nearly for all the measurements. .... 99

Figure 5.5: The circuit layout of the double-sided test PCB. .... 101

Figure 5.6: The manufactured double-sided test PCB. .... 101

Figure 5.7: The generic block diagram of the automated test setup used in the scope of this thesis. .... 103

Figure 5.8: The Agilent VEE program created to test the accelerometer performance under different values of proof mass voltage. .... 103

Figure 5.9: The circuit configuration in which the functionality of the open-loop readout electronics is tested. .... 104

Figure 5.10: Case study Step 1: The surface governed by the effective spring constant equation as a function of spring and gap undercut values. The solution line in accordance with the measured pull-in voltage is the intersection of this surface with the zero plane. .... 107

Figure 5.11: Case study Step 2: The surface governed by the open-loop scale factor equation as a function of spring and gap undercut values. The solution line is the intersection of this surface with the constant plane of measured scale factor. ....	108
Figure 5.12: Case study Step 3: The two solution lines obtained from the first two steps of the undercut estimation case study. The intersection of both lines gives the solution pair of spring and finger undercut values.....	109
Figure 5.13: The normalized output behavior of the closed-loop accelerometer shortly after power-up. It takes around 20 minutes before the system settles in its nominal operation point. ....	110
Figure 5.14: The linearity performance of the accelerometer demonstrated with an ideal line-fit for the given scale factor. ....	112
Figure 5.15: The deviation of the output of the accelerometer from the ideal line-fit at each point of linearity measurement. ....	113
Figure 5.16: The Allan Deviation plot of the 2-hour-long data collected from the proposed accelerometer demonstrated along with the -0.5 sloped line fit.....	114
Figure 6.1: The block diagram of the two-axis accelerometer using the proposed accelerometer readout circuit. ....	118
Figure 6.2: The data collected from the two-axis accelerometer through a full circular rotation where the xy-plane of the accelerometer is set vertical to the ground and the rotation is along z-axis [43].....	120
Figure 6.3: The cross-sectional view of the sensing element where the lateral comb type electrodes are used to form a differential capacitance pair with the vertical z-electrode placed beneath the proof mass [44]. ....	121
Figure 6.4: The use of AFFRO with the hybrid electrodes concept to sense acceleration in out-of-plane axis [44]. ....	122
Figure 6.5: The linearity performance of the implemented out-of-plane accelerometer presented along the simulation results. ....	124
Figure 6.6: The noise performance of the implemented out-of-plane accelerometer. ....	124

# LIST OF TABLES

## TABLES

Table 3.1: The geometrical design parameters and their values. The properties such as the sensitivity of the sensor, which can be calculated using the parameters given in the table, are not included. ....	45
Table 3.2: The electrical configuration parameters used both in the simulations and the circuit implementation.....	47
Table 3.3: Passive component values used in the creation of the Simulink model for the open-loop electronics. Note that these are the actual values that are used in circuit-level implementation as well. ....	49
Table 3.4: The controller parameters set after the two tuning steps applied on the system.....	59
Table 3.5: Simulated performance summary of the accelerometer in open-loop configuration. ....	65
Table 3.6: Simulated performance summary of the proposed closed-loop accelerometer. ....	67
Table 4.1: The passive components used in the implementation of the front-end electronics.....	74
Table 4.2: The passive components used in the implementation of the low-pass filter. ....	75
Table 4.3: The passive components used in the implementation of the PI-controller. ....	76
Table 4.4: The three major noise contributors and the associated noise gain (NG*) values to refer them to the input in $g/\sqrt{\text{Hz}}$ units. ....	88
Table 4.5: Noise sources of the front-end electronics and the associated noise gains. ....	89

Table 4.6: Noise sources of the low-pass filter and the PI-controller with the associated noise gains to refer to output (NG); and multiplication factors to refer to input (MF). .....	91
Table 4.7: The summary of the noise sources effecting the overall accelerometer and their g-equivalent values. ....	92
Table 4.8: The estimated performance summary of the proposed closed-loop accelerometer. ....	93
Table 5.1: The pin-out of the analog accelerometer package. Note that during closed-loop operation, pins ‘VFB’ and ‘PIOUT’ are connected to each other. ....	96
Table 5.2: The evaluation of bias repeatability performance of the proposed accelerometer based on the data set presented in Figure 5.19. ....	115
Table 5.3: Simulated and measured performance summary of the proposed accelerometer. ....	116



# CHAPTER 1

## INTRODUCTION

With the developments in the silicon-based integrated circuit fabrication techniques, the electrical circuit sizes and costs have been reducing rapidly over the years. Moreover the increasing trend for the integrated circuit demands of the market has effectively contributed to the quality of the manufactured devices and fabrication yields. Over the past few decades, a relatively new field of micro-fabrication has been gaining popularity with the adaptation of several fabrication techniques to manufacture micro-mechanical devices in bulk. These mechanical devices, combined with micro-electronics even on the same chip monolithically, has already been commercialized in several fields of the market under the name “Microelectromechanical Systems” (MEMS). The reliability and the performance of the mass-fabricated MEMS devices has been rapidly increasing since the concept was introduced to the industry. Nowadays, many MEMS devices has already started to replace their bulky predecessors not only in commercial, but also in high-performance applications, having the core qualities of mass-fabrication compatibility, high fabrication repeatability, low material costs, and compactness.

The top application areas of the MEMS technology in 2015 by their market share are mobile, automotive, industry, aerospace, and medical electronics [1]; smart phones, airbag deployment systems, navigation systems are just some of the areas where MEMS is commonly used. In these applications, pressure, humidity, temperature, and gas sensors; InkJet heads, microphones, micro-bolometers, projection systems, compasses, gyroscopes and accelerometers and the combination of these devices such as in an inertial navigation system (INS) are widely used [2] [3] [4]. One of the most common applications of MEMS among the aforementioned topics is the inertial

acceleration sensing. With their relatively simple principles of operation compared to inertial MEMS gyroscopes, the performance of the MEMS accelerometers have been rapidly increasing towards the navigation grade performance. Among various types of MEMS accelerometers, capacitive MEMS accelerometers have improved over the recent years to a point where they can compete with their large-scale counterparts, and also offer a higher level of robustness and reliability.

In scope of this thesis, a high-performance analog accelerometer implemented using a capacitive MEMS sensing element is studied. In Section 1.1, some definitions specifying the performance characteristics of an accelerometer are presented. In Section 2.2, an overview of the literature on MEMS accelerometers is made. Finally in Section 2.3, the objectives and the organization of this thesis are given.

## 1.1. Important Definitions

Some definitions that are used in scope of this thesis are listed below with the associated descriptions as most of which are standardized by IEEE in the standard [5].

**g:** The gravity of the earth. The multiplications of this reference value is used for the accelerometer applications, and it corresponds to an acceleration of  $9.80665 \text{ m/s}^2$  unless specified otherwise.

**Scale Factor:** The value which relates the input acceleration to the output of the accelerometer. The unit of this value is  $V/g$  in scope of this thesis.

**Full Range:** The difference between the maximum and minimum input accelerations that can be detected by the accelerometer within the specified performance parameters. The unit of this term is typically  $g$ .

**Full-Scale Input:** The amplitude of maximum and minimum detectable acceleration input in  $g$ . For example if the accelerometer can operate in the range from  $-35$  to  $+35$   $g$ , then the full-scale input is referred as  $35$   $g$  where full range is  $70$   $g$ .

**Operation Bandwidth:** This term is used to describe the -3 dB frequency of the complete accelerometer in  $Hz$  at which the scale factor of the system is reduced by a factor of  $\sqrt{2}$ .

**Maximum Non-linearity:** Maximum deviation of the accelerometer output from an ideal line that is fitted on the input-output response of the system in the specified range. This term is presented as the percentage with respect to the full range.

**Resolution:** Minimum detectable acceleration. The noise on the output signal and the operation bandwidth of the accelerometer directly affects the minimum detectable acceleration. Because of that, the white noise of the accelerometer in  $g/\sqrt{Hz}$  is used along with the operation bandwidth to define the resolution of the accelerometer.

**Velocity Random Walk:** The error caused by the integration of the noise on the output of an accelerometer. If the noise affecting the accelerometer is assumed white, then this term can be obtained by dividing the white noise level by  $\sqrt{2}$ . The unit for this term is expressed in  $g/\sqrt{Hz}$ .

**Bias Instability:** The random variation of the accelerometer output solely due to parasitic effects on the system for a specified averaging time window represented in  $g$ .

**Dynamic Range:** The ratio of the accelerometer range to its white noise level. The dynamic range is expressed in  $dB$  and is presented both for full range and the full scale input of the accelerometer in scope of this thesis. Note the difference is simply  $\sim 6$  dB.

**Cross-Axis Sensitivity:** The ratio used to relate the deviation at the accelerometer output in one axis of acceleration sensing to the input acceleration in another axis. This term is represented as the percentage with respect to the scale factor of the accelerometer in axis-of-interest.

**Warm-Up Time:** The time interval following the power-up after which the performance of the accelerometer satisfies the specified values. As to say, the data acquired from the system in this interval is not reliable and not within the specified performance ratings.

## 1.2. Overview of MEMS Accelerometers

Over the years, various types of accelerometers incorporating different approaches for both sensing elements and the interface circuitry has been introduced to the literature. Among different sensing element types, capacitive accelerometers have created themselves a solid spot both in the academia and the industry [6], [7]. Compared to their counterparts such as quartz or tunneling type accelerometers, capacitive sensors offer a higher degree of robustness [8], [9] and design flexibility at a lower cost of power consumption [10]. Types of capacitive sensing elements can be grouped by their fabrication methods such as bulk micro-machining, surface micro-machining and silicon-on-insulator processes. Bulk micro-machined devices offer a high inertial mass thus have a lower Brownian noise compared to devices of other processes [11]. However, the fabrication of such devices are rather complicated and consequently costly. Surface micro-machined devices are highly compatible for monolithic integration with an interface circuitry at the cost of reduced sensing element design flexibility [12], [13], [14]. On the other hand the silicon-on-insulator type devices rest in a spot between the two other processes in terms of fabrication simplicity, design flexibility and device performance. As for the sensing principles, regardless of the fabrication processes, all of the capacitive sensing elements follow the same trend with differences in the formation of the capacitances. Some of them, usually referred as *lateral* devices, sense the acceleration in the lateral axes in parallel to the chip substrate taking the advantage of topologies such as interdigitated finger structures to increase the sensitivity [15]; whereas some others, which are referred as *vertical* devices, utilize the gap between a suspended mass and the chip substrate to form the variable capacitance [16] in order to measure the *out-of-plane* acceleration inputs in z-axis. Compared to lateral sensing, vertical acceleration sensing, with a comparable sensitivity as the lateral case, is a more challenging task due to the planar nature of the fabrication processes, and as the typical approaches for capacitive acceleration sensing, combinations of various sensing methods are researched for different purposes such as out-of-plane acceleration sensing using comb type fingers with an asymmetrical inertial mass [17].

Apart from the numerous sensing element topologies, there are two main electrical interface approaches for the MEMS accelerometers: Open- and closed-loop readout circuits. The open-loop accelerometers offer a low circuit complexity and less components and thus they can be implemented for lower costs which makes them suitable for many applications. The fundamental issue related with using an open-loop interface is that the dynamics of the accelerometer are solely based on the properties of the sensing element. Since the critical parameters such as the linearity and the noise floor of such systems are defined by the sensing element itself thus they can lack performance of their closed-loop counterparts. Still, it is possible to see the examples of high-performance open-loop accelerometers in the industry [18]. On the other hand, closed-loop accelerometers can offer much higher linearity and dynamic range values at the cost of design complexity. Even though relatively complicated, closed-loop topologies also offer a much higher degree of customization and calibration in the parameters such as bandwidth, dynamic range, and off-set only through modifications in the circuit design. Compared to the open-loop accelerometers, the main critical considerations related with the closed-loop accelerometers are the system stability and the feedback topology. In some reported works, the force-feedback action can be achieved using dedicated actuating electrodes to counteract the forces exerted on the inertial mass by the applied acceleration [19]. However, this causes the effective sensitivity of the sensor per unit chip area to reduce since only a part of the inertial mass capacitive surface can be utilized for the sensing. A solution to such problem is offered with the introduction of digital feedback to the literature. In such a readout circuit, the operation of the accelerometer is divided into two distinct phases for sensing and feedback. Using switches to alternately connect the sensing element to the front-end electronics in one phase; and to the feedback network in the other, simultaneous sensing and digital feedback can be achieved.  $\Sigma\Delta$  (sigma-delta) readout circuit topology is the most significant example to such closed-loop accelerometers. In addition to simultaneous operation,  $\Sigma\Delta$  circuits incorporate an internal digitizer and can directly output digital data [20]. With these properties,  $\Sigma\Delta$  readout circuits are very popular and widely researched and used [10]. On the other hand, there are also analog readout circuits which achieve simultaneous readout and feedback operation on the same electrode set [21], [22], [23]. The advantage of such topology comes with design

simplicity, the elimination of quantization noise resulting from the digitizing, and continuous operation without switching back and forth between two tasks. Nowadays, many of the accelerometers in the literature and the industry are dominated by multi- or single-axis capacitive accelerometers interfaced using digital readout topologies.

### **1.3. Thesis Objectives and Organization**

The primary objective of this thesis is to design and implement a closed-loop analog accelerometer. Besides a high performance, a high versatility is expected from the targeted accelerometer. The generic topology used for the implemented accelerometer is similar to the one presented in [21], [22] with major differences in the feedback structure which significantly increases the measurement range and reduces the risk of saturating the pre-amplifier under the effects of shock or high acceleration inputs. The objectives overview of the work in this thesis are summarized in the list below:

- A closed-loop analog readout circuit with sufficiently high feedback gain is to be designed so that a highly linear operation in the range of interest can be satisfied. The white noise level of this readout circuit is to be kept below  $10 \mu\text{g}/\sqrt{\text{Hz}}$ .
- The ultimate accelerometer is expected to have an operation bandwidth of  $\sim 100 \text{ Hz}$ ; and an operation range of  $-10 \text{ g}$  to  $+10 \text{ g}$ .
- A feedback topology is to be designed such that the readout and feedback tasks are achieved in continuous time simultaneously. Also the force feedback task is expected to have no effect on the front-end readout signals so that the risk of saturating the electronics loop is eliminated.
- The readout circuit is expected to achieve closed-loop operation using only a single set of differential electrodes. As to say, both readout and feedback tasks are to be carried out without using separate electrode sets for each task.
- The proposed readout circuit is to be compatible for single-mass, multi-axis capacitive acceleration sensing elements.
- A reliable, high-accuracy simulation model is to be prepared for the proposed accelerometer. This way, the proposed circuit is aimed to be a highly versatile

research platform which can be easily adapted to sensing elements of different properties.

- The static and the dynamic behavior of the accelerometer is to be formulated with sufficient amount of precision so that the performance of the accelerometer can be estimated prior to implementation.

The summary of the following chapters in thesis are given in the following paragraphs in a consecutive manner.

In Chapter 2, the theoretical background of the building blocks of the proposed accelerometer is given. The formulas associated with each building block are presented in detail. Using these information, the operation of an open-loop capacitive accelerometer is demonstrated. Based on this presented open-loop accelerometer, the critic of the necessity of closed-loop operation is made. Moreover, the method used to achieve closed-loop operation using a single set of differential electrodes is introduced and critical considerations about this method are described.

In Chapter 3, two different MATLAB simulation models prepared for the proposed accelerometer are presented. One of these models are used to simulate the complete system in time-domain while the other is used for frequency-domain analysis. The reason for using two different models to characterize the system is also discussed. Additionally, the controller design approach is presented with stability considerations.

In Chapter 4, the component-level design steps of the proposed readout circuit are shown. A behavioral electrical model which is created in SPICE environment is also demonstrated. This model is prepared to simulate the proposed readout circuit including the electrical component non-idealities unlike the models created in MATLAB environment.

In Chapter 5, the details about the implementation steps of the proposed accelerometer are presented. Moreover, the test setups used for the performance measurements are introduced. The measurement results demonstrating the performance of the implemented accelerometer are also demonstrated in this chapter.

In Chapter 6, two different multi-axis acceleration sensing applications, which are realized using the proposed accelerometer, are presented. The associated measurement results of these applications are demonstrated as well.

In Chapter 7, a conclusion of the work presented in this study is given. Also a discussion of possible further work, which can be done on the proposed accelerometer, is made.

## **CHAPTER 2**

### **CLOSED-LOOP ANALOG ACCELEROMETER READOUT THEORY**

In this chapter, the building blocks of the proposed closed-loop analog accelerometer will be introduced in a progressive manner. While doing so, the parametric derivations and equations related with each block will be presented in detail. In Section 2.1, the static and the dynamic properties of the capacitive sensing element, which is used for the implementation of the analog accelerometer, will be analyzed. In Section 2.2, the capacitive sensing interface utilizing a transimpedance amplifier (TIA) as the pre-amplifier and the differential sensing method will be presented. The section will continue by introducing the use of a demodulator and a low-pass filter (LPF) after the pre-amplification stage. At the end of the section, the conceptual block diagram of an open-loop analog accelerometer readout circuit will be presented, and its feasibility will be discussed. In Section 2.3, closed-loop operation in capacitive accelerometers will be presented. The capacitive actuation principles, followed by the differential force feedback method, as used in the proposed system, will be analyzed in detail. In Section 2.4, the method, which enables the use of differential sensing and electrostatic force-feedback simultaneously, will be described. Moreover, by the end of this chapter, this method will be further extended to realize a conceptual block diagram for the proposed continuous-time closed-loop analog accelerometer. Finally, in Section 2.5, the theory described in this chapter will be summarized.

## 2.1. Properties of the MEMS Sensing Element

Various types of capacitive MEMS accelerometers are discussed in the introduction chapter. Among these types, a single-axis, single-mass, differential, lateral capacitive accelerometer is used for the implementation of the proposed system. The sensing element was designed at METU-MEMS Center. In Figure 2.1, the Scanning Electron Microscope (SEM) image of one quadrant of this sensing element is given.

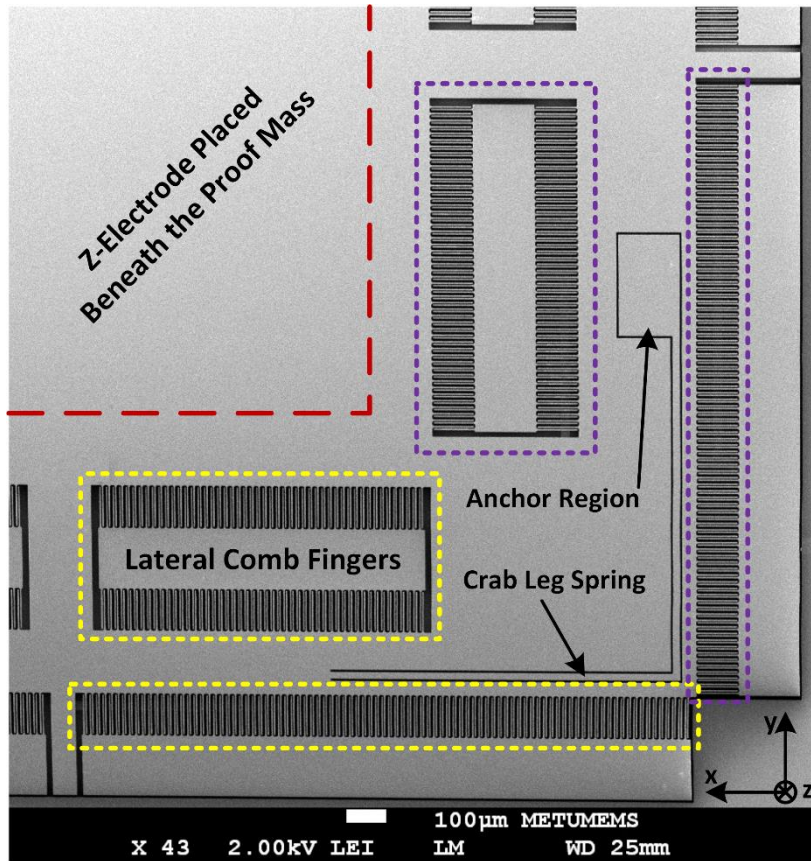


*Figure 2.1: The Scanning Electron Microscope (SEM) image of lower-right quadrant of the sensing element used in the proposed work.*

The utilized sensing element has a total of five electrodes. Two of these electrodes are utilized to sense differentially in x-axis (yellow dashed boxes in Figure 2.1); other two are used to sense differentially in y-axis (purple dashed boxes in Figure 2.1). The last electrode is placed beneath the proof mass and senses acceleration in z-axis (red dashed box in Figure 2.1). Throughout most of this thesis, only the x-electrodes are

used to verify the operation of the proposed readout circuit. As to say, the circuit is studied in a single-axis accelerometer application. Even though in Chapter 6, utilization of z- and y-electrodes are also presented with the proposed multi-axis applications, the sensing element is considered as if it was a single-axis device until Chapter 6. In Figure 2.2, a simplified diagram and the equivalent electrical model of the sensing element are given for a better visualization and understanding of sensor operation in one axis.

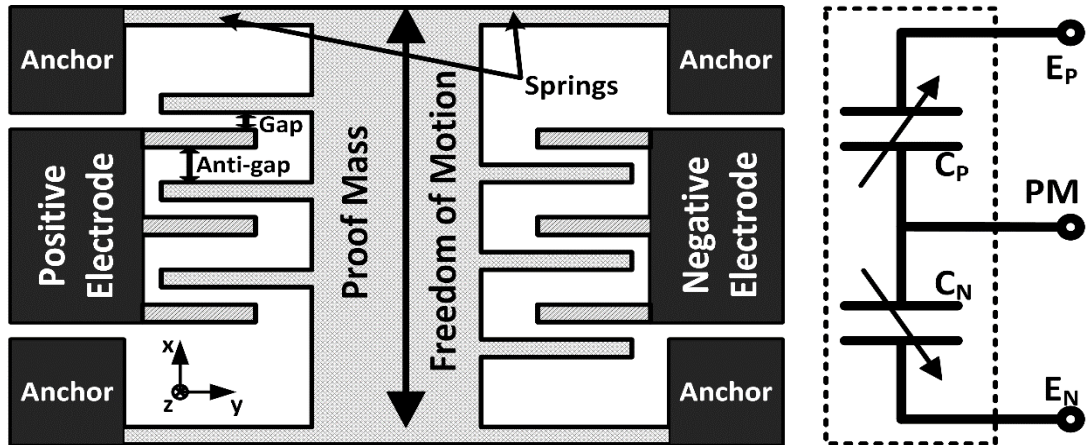


*Figure 2.2: The simplified diagram and the equivalent electrical model of the sensing element. Even though the mechanical structure is fully symmetrical, the two electrodes ( $E_p$ ,  $E_n$ ) and the capacitances ( $C_p$ ,  $C_n$ ) are denoted as ‘positive’ and ‘negative’ for convenience. Note that the PM node in the electrical model can be visualized as if it can move up and down, changing the parallel plate capacitances of  $C_p$  and  $C_n$  differentially.*

Each of the two stationary electrodes of the sensor carry one set of comb fingers. Through these finger sets, the electrodes are capacitively coupled to the proof mass’s comb finger sets forming two differential, parallel-plate, varying-gap capacitances between each electrode and the proof mass. The proof mass of this sensor is suspended slightly above the glass substrate on the anchors via the cantilever beam type springs. The springs provide the proof mass a freedom of motion in one axis as also shown in Figure 2.2, while mostly restraining any movement of the mass in other axes. These springs yield a significant role in the dynamic behavior of the sensing element as it will be discussed further in this section.

Once an external acceleration is applied on the sensing element in one direction along the x-axis, the proof mass will move towards the other direction by Newton's Second Law of Motion. This motion will cause an increase in one capacitance, and a decrease in the other. This way, a differential operation between the two complementary capacitances ( $C_p$ ,  $C_n$ ) will be achieved.

The formulas relating the parallel-plate capacitance and the motion of the proof mass in x-direction are as follows:

$$C_p = (N) * \left( \frac{\epsilon * A_{ea}}{d_{gap} - x} \right) + (N - 1) * \left( \frac{\epsilon * A_{ea}}{d_{a-gap} + x} \right) \quad (2.1)$$

$$C_n = (N) * \left( \frac{\epsilon * A_{ea}}{d_{gap} + x} \right) + (N - 1) * \left( \frac{\epsilon * A_{ea}}{d_{a-gap} - x} \right) \quad (2.2)$$

where, 'x' is the displacement of the proof mass along x-axis; 'N' is the number of fingers on each electrode; ' $\epsilon$ ' is the permittivity of air; ' $A_{ea}$ ' is the overlap area of each finger pair; ' $d_{gap}$ ' and ' $d_{a-gap}$ ' are the finger separations in gap and anti-gap regions respectively.

When speaking of a capacitive accelerometer, the amount of change in the capacitance of each electrode as the response to an external acceleration is, obviously, important. This response of the sensing element is usually referred as the *sensitivity* of the sensor. Even though there are a number of different ways to denote such term, the sensitivity will be referred as "*the amount of capacitance change per unit displacement of the proof mass*" throughout this thesis. Such definition is useful for it leaves the *inertial mass* (mass of the proof mass) out of the sensitivity equations as another design criteria. The sensitivity,  $dC/dx$ , of an electrode's capacitance can be formulated as follows:

$$\frac{dC_p}{dx} = \frac{d \left[ (N) * \left( \frac{\epsilon * A_{ea}}{d_{gap} - x} \right) + (N - 1) * \left( \frac{\epsilon * A_{ea}}{d_{a-gap} + x} \right) \right]}{dx} \quad (2.3)$$

$$\frac{dC_p}{dx} = + \frac{\epsilon * N * A_{ea}}{(d_{gap} - x)^2} - \frac{\epsilon * (N - 1) * A_{ea}}{(d_{a-gap} + x)^2} \quad (2.4)$$

Similarly,

$$\frac{dC_n}{dx} = -\frac{\epsilon * N * A_{ea}}{(d_{gap} + x)^2} + \frac{\epsilon * (N - 1) * A_{ea}}{(d_{a-gap} - x)^2} \quad (2.5)$$

Note that the change in the capacitances formed by the anti-gap regions oppose trend of the change in capacitances formed by the gap regions for each electrode at it can be seen in Equations 2.1 and 2.2. As to say, as the mass moves towards one direction, if the gap capacitances increase; the anti-gap capacitances decrease or vice versa. The effect of such behavior can also be seen by the sensitivity equations of each electrode as given in Equations 2.4 and 2.5. The anti-gap regions counter the gap regions sensitivity-wise, and if both openings are of equal separations, the sensor will have no sensitivity around its *rest position* ( $x \approx 0$ ) at all. In order to prevent such consequence, the sensing element is designed and fabricated so that the anti-gap separations are much larger than the gap separations. This way the anti-gap capacitance will yield a much smaller value, and its effect on both the electrical behavior and the sensitivity of the total electrode capacitance is significantly reduced. Considering this, the capacitance and the sensitivity formulas can be simplified and used in the form as shown in Equations 2.7-2.10 for the sake of notation simplicity. Note that while modelling the actual system in a simulation environment, such simplifications are not used.

$$N * A_{ea} = A_{tot} \quad (2.6)$$

$$C_p \cong \frac{\epsilon * A_{tot}}{d_{gap} - x} \quad (2.7)$$

$$C_n \cong \frac{\epsilon * A_{tot}}{d_{gap} + x} \quad (2.8)$$

and,

$$\frac{dC_p}{dx} = +\frac{\epsilon * A_{tot}}{(d_{gap} - x)^2} \quad (2.9)$$

$$\frac{dC_n}{dx} = -\frac{\epsilon * A_{tot}}{(d_{gap} + x)^2} \quad (2.10)$$

Note that when the sensor is at rest position, i.e. no external acceleration or force is applied on it, the value of the two differential complementary capacitors,  $C_p$  and  $C_n$  are ideally equal with equal sensitivities of opposite signs .

Combining the effect of the acceleration on the proof mass's displacement and on the difference between two capacitances, the static response of the sensing element to acceleration can be summarized with the following formulas.

$$F_{EXT} = m * a_{ext} = k * x \quad (2.11)$$

$$x = \frac{m}{k} * a_{ext} \quad (2.12)$$

where ' $F_{ext}$ ' is the external force applied on the sensing element by an external acceleration; ' $m$ ' is the inertial mass; ' $a_{ext}$ ' is the external acceleration applied on the sensing element; ' $k$ ' is the mechanical spring constant of the sensing element; and ' $x$ ' is the displacement of the proof mass.

$$\Delta C = C_p - C_n = \left( \frac{\epsilon * A_{tot}}{d_{gap} - x} \right) - \left( \frac{\epsilon * A_{tot}}{d_{gap} + x} \right) \quad (2.13)$$

thus, the relation between the applied acceleration and the capacitance difference between the two complementary capacitances is:

$$\Delta C = \left( \frac{\epsilon * A_{tot}}{d_{gap} - \frac{m}{k} * a_{ext}} \right) - \left( \frac{\epsilon * A_{tot}}{d_{gap} + \frac{m}{k} * a_{ext}} \right) \quad (2.14)$$

As it can be seen in the Equation 2.14, the capacitance difference between the two capacitances are strictly related with the only variable in the equation: the applied acceleration. However it must be noted that this relation is highly *non-linear*. In Figure 2.3, this relation is visualized in a plot for a better understanding. Note that the values in Figure 2.3 are of a typical capacitive accelerometer.

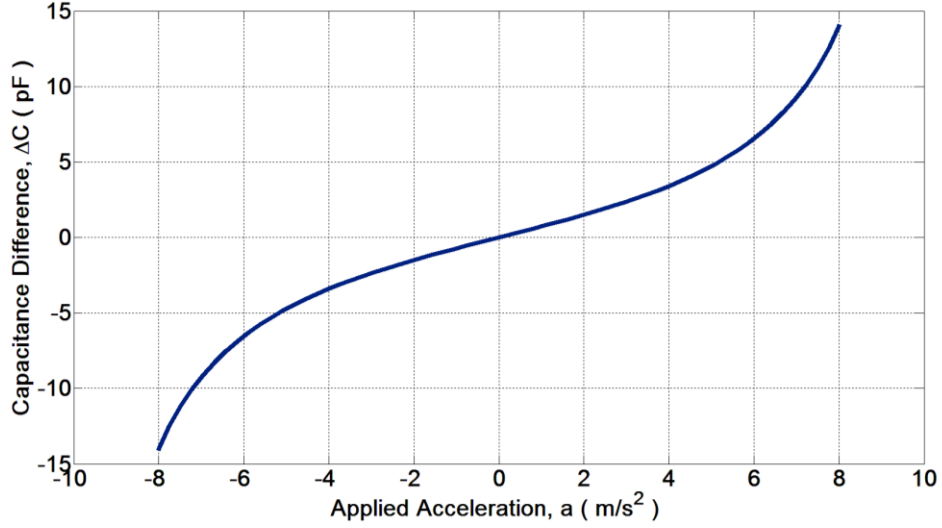


Figure 2.3: The plot demonstrating the relation between the applied acceleration and the capacitance difference between the two complementary electrode capacitances of a typical capacitive accelerometer. Notice the non-linear behavior.

The relations above summarize the static behavior of the sensing element mostly, but says little about the dynamic response of it. As it is described in detail in [24], [25], micro-machined accelerometers behave as second-order mass-spring-damper systems. The generic s-domain transfer function,  $K(s)$ , of the accelerometer used in the proposed system can be formulated as follows:

$$K(s) = \frac{X(s)}{F(s)} = \frac{1/m}{s^2 + \frac{b}{m}s + \frac{k}{m}} \quad (2.15)$$

where, ‘ $X$ ’ and ‘ $F$ ’ are the Laplace transforms of the proof mass displacement and the force applied on the proof mass by either acceleration or electrostatic actuation respectively; ‘ $m$ ’ is the mass of the suspended proof mass; ‘ $k$ ’ is the mechanical spring constant; and ‘ $b$ ’ is the damping coefficient. Note that the damping in varying-gap capacitive MEMS micro-structures is mostly dominated by the phenomenon referred as *squeezed-film damping* [26], [27].

Unlike resonant MEMS devices [28] with high *quality factors* ( $Q = \sqrt{k * m}/b$ ), which behave as mechanical band-pass filters, the device used in this work behaves as a mechanical low-pass filter. As to say, the actuation force components ( $F(s)$ ) at higher

frequencies are filtered out mechanically, and their effect on the proof mass displacement ( $X(s)$ ) is significantly reduced.

At this point, it is convenient to point out the contrast in the mechanical and the electrical dynamic behaviors of the sensing element. On the contrary to the mechanical filtering behavior of the sensing element, the two differential electrodes are actually electrical RC high-pass filters in terms of the current generated by a voltage applied on one electrode, flowing through one capacitance towards the proof mass. As it will be discussed further in Section 2.4, Simultaneous Differential Sensing and Force-Feedback, this contrast between the mechanical and electrical filtering properties of the sensor is what makes continuous-time closed-loop operation of the analog accelerometer possible.

## **2.2. Capacitive Sensing Interface**

The operation principles of the differential capacitive MEMS acceleration sensing element is introduced in the previous section. The theory behind the interface between the sensing element and the readout electronics are discussed in following sub-sections.

### **2.2.1. Differential Sensing and Capacitive Pre-Amplification**

As discussed earlier, the capacitance difference between the two complementary electrodes of the sensing element is strictly related to the applied acceleration. In order to surpass this capacitance difference information, resulting from the motion of the proof mass, into electrical domain, two *AC carrier signals* at opposite phases are used. These signals modulate the capacitance value of each complementary capacitor into an electrical current, and the difference of these currents are directed to the front-end electronics for pre-amplification. Figure 2.4 shows the simplified circuit diagram of the front-end electronics, and also demonstrates the modulation. If an external acceleration is applied onto the sensing element so that the capacitance of the positive electrode ( $C_p$ ) is larger than the capacitance of the negative electrode ( $C_n$ ), then the positive electrode current,  $i_p$ , will be larger than the negative electrode current,  $i_n$ . Thus,

there will be an excess current flowing towards the pre-amplifier at the same phase as the  $v_{ac}$  signal (solid lines). On the other hand, if the acceleration is applied in the opposite direction so that ' $C_n$ ' is larger than the ' $C_p$ ', this time the current flowing towards the pre-amplifier will be at the same phase as the ' $-v_{ac}$ ' signal (dashed lines). This way, not only the difference between the two capacitances will be modulated, but also the *direction* of the applied acceleration will be passed onto the electronics readout as the phase (or sign) information.

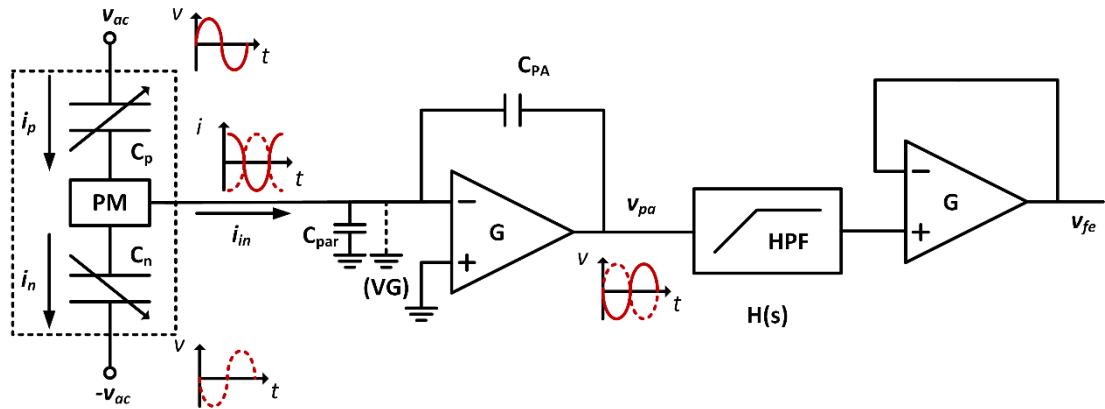


Figure 2.4: The simplified circuit diagram demonstrating the modulation of the capacitances of the two electrodes and the front end electronics. ' $C_p$ ' and ' $C_n$ ' are the two differential capacitances of the sensing element; ' $PM$ ' is the proof mass of the sensor; and ' $v_{ac}$ ' is the carrier signal. The operational amplifier  $G$  is configured as a capacitive transimpedance amplifier (TIA) for pre-amplification. This stage is followed by a passive high-pass filter,  $H(s)$ , and a voltage buffer.

The modulation of the acceleration information on the sensing element can be formulated as shown in the equations below.

The carrier signal has the following form:

$$v_{ac} = \alpha * \sin(\omega t) \quad (2.16)$$

Assuming the proof mass node is virtually grounded by the amplifier,  $G$ , the currents flowing through the positive and negative electrode capacitances are:

$$i_p \cong C_p(t) * \frac{d(v_{ac})}{dt} \quad (2.17)$$

$$i_n \cong C_n(t) * \frac{d(v_{ac})}{dt} \quad (2.18)$$

thus the input current,  $i_{in}$ , of the amplifier stage is:

$$i_{in} = i_p - i_n = (C_p(t) - C_n(t)) * \frac{d(v_{ac})}{dt} \quad (2.19)$$

$$i_{in} = \Delta C(t) * (\alpha * w * \cos(\omega t)) \quad (2.20)$$

As it can be seen in Equation 2.20, the capacitance difference between the two electrodes,  $\Delta C$ , is modulated onto a current,  $i_{in}$ , by the derivative of the carrier signal,  $v_{ac}$ . Also the sign of ' $\Delta C$ ' specifies the sign of the current ' $i_{in}$ ' so that the direction of the applied acceleration can be determined. Note that if no external acceleration is applied, the net current flowing towards the pre-amplifier is ideally zero.

After this point it is rather convenient to use the Laplace transforms for the sake of notation simplicity. Equation 2.20 can be rewritten in the following simplified form in s-domain assuming the sensing element is in steady state:

$$I_{in} = \Delta C * s * V_{ac} \quad (2.21)$$

In order to amplify this current, flowing towards the front-end electronics, and convert it to voltage, a transimpedance amplifier (TIA) is used as the pre-amplifier as also shown in Figure 2.4. The TIA used in the proposed system is configured as a *capacitive amplifier*.

There are three main reasons for using a capacitive TIA as the pre-amplifier stage. The first reason is the topology's immunity to the parasitic capacitances occurring between the proof mass and the inverting input of the amplifier. These capacitances form mainly due to the wire-bonds and interconnecting paths that run side-by-side. In Figure 2.4,  $C_{par}$  denotes the equivalent capacitance of these parasitic components in a single element. Assuming the open-loop gain of the operational amplifier is high enough, the inverting input of it can be considered as a virtual ground node and thus

the parasitic capacitances will be effectively eliminated between the virtual ground and the actual circuit ground.

The second advantage of using capacitive amplification is its superior noise performance compared with resistive amplification. Unlike some low frequency applications where the feedback capacitor is solely used for stability compensation and a large feedback resistor is used for amplification [29], in the proposed system the feedback capacitor's value is the dominant term for determining the pre-amplifier gain. Using such approach, the value of the feedback resistor can be kept at a lower value, effectively reducing its thermal noise contribution to the system; and the feedback capacitor, which is comparably a less-noisy component, can be set to achieve the desired gain. Noise consideration of the pre-amplifier stage will be re-visited in Section 4.3 in more detail.

The third advantage of capacitive amplification is its capability of cancelling the frequency dependence of the readout current flowing into the pre-amplifier. This dependence is shown in Equation 2.20. For a certain, well-defined range of carrier signal frequencies, capacitive amplification can maintain a constant gain between the input carrier signal  $v_{ac}$ , and the pre-amplifier voltage output  $v_{pa}$ . This way, possible fluctuations that might occur in the carrier signal frequency can easily be tolerated without causing any inconsistency in the front-end readout characteristics. This property is investigated below along with the transfer characteristics of the capacitive pre-amplifier.

The s-domain transfer function of the pre-amplifier,  $G(s)$ , including the effect of the capacitance difference between the two differential electrode capacitors,  $\Delta C$ , can be expressed as follows:

$$G(s) = \frac{I_{in}}{V_{ac}} * \frac{V_{pa}}{I_{in}} = \frac{V_{pa}}{V_{ac}} = (s * \Delta C) * \left( \frac{1}{s * C_{pa}} \right) \quad (2.22)$$

where, ' $C_{pa}$ ' is the feedback capacitance of the pre-amplifier.

Thus,

$$G(s) = \frac{V_{pa}}{V_{ac}} = \frac{\Delta C}{C_{pa}} \quad (2.23)$$

As it is simply denoted in Equation 2.23 above, using capacitive TIA, the frequency dependence of the current fed to the pre-amplifier can be eliminated. Moreover, without using a very large gain resistor at the pre-amplifier feedback and degrading the noise performance, a large gain can be achieved by using a small capacitance at the feedback network.

As it will be introduced later on, in addition to the carrier signals, low-frequency and DC voltages are also applied on the sensing element in order to achieve closed-loop operation. These voltages can cause leakage currents through the sensing element towards the pre-amplifier causing undesired low-frequency offset voltages at the output of the pre-amplifier. In order to reduce the effects of such parasitic low-frequency currents, and maintain the front-end readout consistency, the pre-amplifier output,  $v_{pa}$ , is high-pass filtered before generating the final front-end electronics output,  $v_{fe}$ . A passive RC high-pass filter followed by a voltage buffer is decided to be sufficient for this stage.

As a visual summary, the input-output waveforms of the front-end electronics are demonstrated in Figure 2.5 in a non-quantitative plot.

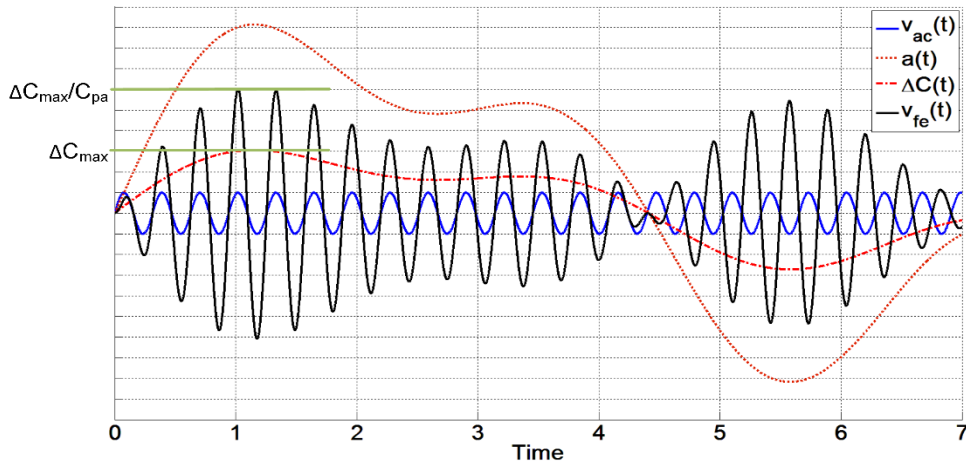


*Figure 2.5: A visual summary of the front-end electronics based on non-quantitative sample waveforms.  $v_{ac}(t)$  is the carrier signal;  $a(t)$  is the applied acceleration;  $\Delta C(t)$  is the capacitance difference between the two electrode capacitances; and  $v_{fe}(t)$  is the front-end electronics output.*

### 2.2.2. Signal Rectification by Demodulation and Low-Pass Filtering

After the pre-amplification, the modulated voltage signal generated by the front-end electronics is demodulated. By demodulation, the acceleration information is converted down to the base-band from the carrier signal frequency. Additionally, the polarity information of the applied acceleration is deciphered at this stage. In Figure 2.6 a simplified block diagram demonstrating the demodulation and low-pass filtering stages is given.

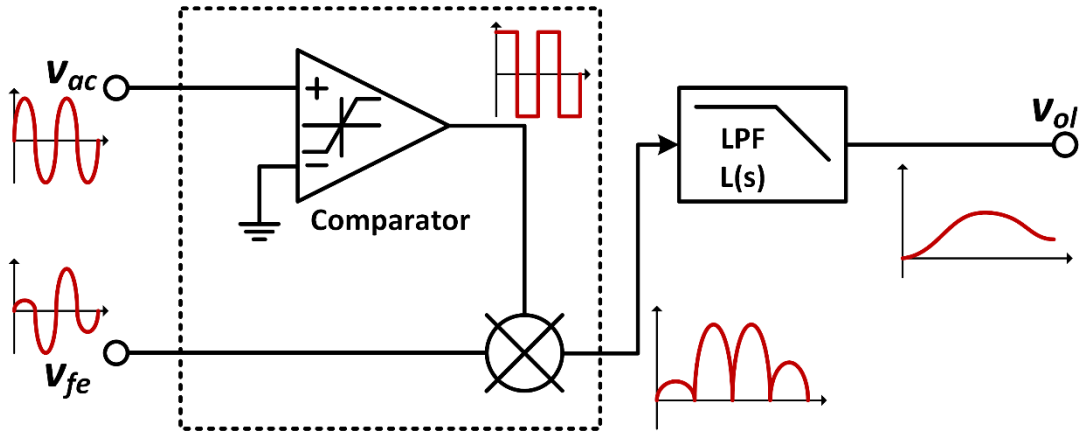


Figure 2.6: The simplified block diagram demonstrating the demodulation and low-pass filtering steps. The dashed box includes a comparator and a multiplier which basically summarizes the operation of the switching demodulator used in the proposed system.

Demodulation is, basically, multiplication of the waveform to be demodulated by a unity square wave (generated based on the  $v_{ac}(t)$  signal for this work), and a square wave ' $sq(t)$ ' can easily be expressed using Fourier Series expansion:

$$sq(t) = \frac{4}{\pi} * \sum_{n=1}^{\infty} \frac{\sin((2n-1)*w_c*t)}{(2n-1)} \quad (2.24)$$

where ' $w_c$ ' is the angular frequency of the carrier signal.

$v_{fe}$  has the following generic form:

$$v_{fe} = a(t) * \sin(w_c * t) \quad (2.25)$$

where ‘ $a(t)$ ’ is the low-frequency *envelope* generated based on the applied acceleration.

Thus the demodulator output voltage,  $v_{demod}(t)$ , can be expressed as follows:

$$v_{demod}(t) = v_{fe}(t) * sq(t) \quad (2.26)$$

$$v_{demod}(t) = a(t) * \sin(w_c * t) * \left[ \frac{4}{\pi} * \sum_{n=1}^{\infty} \frac{\sin((2n-1)*w_c*t)}{(2n-1)} \right] \quad (2.27)$$

$$\begin{aligned} v_{demod}(t) &= \frac{4}{\pi} a(t) \sin(w_c t) * \left[ \frac{\sin(w_c t)}{1} + \frac{\sin(3w_c t)}{3} + \sum_{n=3}^{\infty} \frac{\sin((2n-1)w_c t)}{(2n-1)} \right] \\ &= \frac{4}{\pi} a(t) [\sin(w_c t) \sin(w_c t)] + \frac{4}{\pi} a(t) \sin(w_c t) \left[ \frac{\sin(3w_c t)}{3} + \frac{\sin(5w_c t)}{5} + \dots \right] \end{aligned} \quad (2.28)$$

By trigonometric identities, Equation 2.28 can be transformed into the following form:

$$\begin{aligned} v_{demod}(t) &= \frac{4}{\pi} a(t) \left[ \frac{1}{2} - \frac{1}{2} \cos(2w_c t) \right] \\ &\quad + \frac{4}{\pi} a(t) \sin(w_c t) \left[ \frac{\sin(3w_c t)}{3} + \frac{\sin(5w_c t)}{5} + \dots \right] \\ v_{demod}(t) &= \frac{4}{\pi} a(t) \left[ \frac{1}{2} - \frac{1}{2} \cos(2w_c t) \right] \\ &\quad + \frac{4}{\pi} a(t) \sin(w_c t) \left[ \frac{\sin(3w_c t)}{3} + \frac{\sin(5w_c t)}{5} + \dots \right] \\ v_{demod}(t) &= \frac{2}{\pi} * a(t) \\ &\quad + \left[ -\frac{2}{\pi} a(t) \cos(2w_c t) + \frac{4}{\pi} a(t) \sin(w_c t) \right. \\ &\quad \left. * \left( \frac{\sin(3w_c t)}{3} + \frac{\sin(5w_c t)}{5} + \dots \right) \right] \end{aligned} \quad (2.29)$$

The frequency of the carrier signal,  $w_c$ , is set to be much higher than the maximum allowed frequency of the input acceleration. Since the envelope signal,  $a(t)$ , directly follows the fashion of the applied acceleration, maximum frequency of ‘ $a(t)$ ’ will also

be much smaller than the carrier signal frequency. The terms inside the square brackets in Equation 2.29 above are at a frequency of at least two times the carrier signal's ( $2\omega_c$ ). Thus, they can be filtered out by a low-pass filter placed after the demodulator as shown in Figure 2.6 without affecting the envelope signal significantly. Resultantly the signal,  $v_{ol}$ , at the output of the unity-gain low-pass filter can be approximated as follows:

$$v_{ol}(t) \cong \frac{2}{\pi} * a(t) \quad (2.30)$$

As the Equation 2.30 implies, the low-frequency acceleration envelope,  $a(t)$ , is extracted from the modulated waveform,  $v_{fe}$ , by demodulation and low-pass filtering.

### 2.2.3. An Open-Loop Analog Accelerometer Readout Circuit

As discussed earlier, the signal acquired at the output of the low-pass filter is shaped by the applied acceleration. In other words, the electronic blocks up to the low-pass filter, as taken into account so far, form an open-loop accelerometer readout circuit. Figure 2.7 demonstrates the simplified block diagram of this circuit.

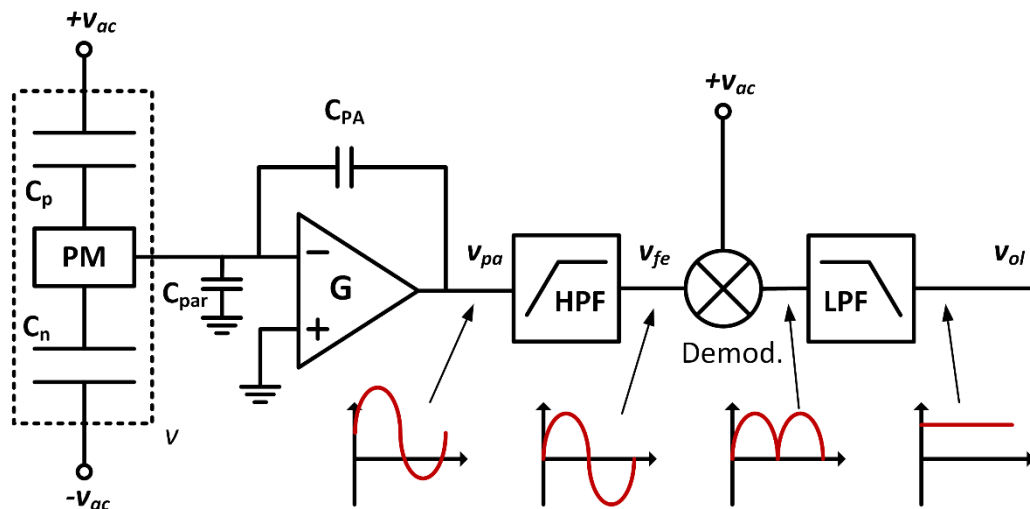


Figure 2.7: The block diagram of the circuit forming an open-loop accelerometer.

Even though the circuit demonstrated in Figure 2.7 is actually a fully functional accelerometer, there are a number of issues that would limit the maximum performance that can be obtained from such system. The first and the most important limiting factor is the linearity performance. Since the varying-gap MEMS accelerometer used in this work is a highly non-linear block (Equation 2.14), the output of this circuit,  $v_{ol}$ , will also yield a non-linear behavior, especially for large acceleration inputs (Figure 2.3). Linearity is one of the most fundamental features of a sensor, and the open-loop circuit is not a feasibly practical solution for acceleration sensing since in open-loop configuration, overall performance of the accelerometer will be dominated by the sensing element [10].

Another performance-limiting issue of such system is the dilemma between the maximum operation range and the noise performance. If there is no mechanical limitation (gap separation, pull-in, etc.), the operation range of such system is basically limited with the supply rails of the circuit; especially the pre-amplifier's. The capacitance difference between the two electrode capacitors ( $\Delta C$ ) are inversely proportional to the proof mass displacement (Equation 2.13), thus the applied acceleration. This results in a sharp increase at the  $\Delta C$  value after a certain amount of acceleration input, and it eventually diverges to infinity. Since the peak value of the pre-amplifier output signal ( $v_{pa}$ ) is directly proportional to  $\Delta C$ ,  $v_{pa}$  will be clipped after a certain amount of acceleration input causing distortion at the circuit output. A solution to such problem is to tune the pre-amplifier gain to a lower value. But as a trade-off, such action will cause the noise performance of the circuit to degrade.

The issues discussed above can be overcome using a closed-loop system. By doing so, the circuit performance can be increased tremendously matching the performance of the high-quality sensing element.

In the next sections, the closed-loop readout circuit based on this open-loop sensing circuit will be introduced in a step-by-step approach.

### 2.3. Closed-Loop Accelerometer Operation Principles

As in many examples in the literature, a closed-loop accelerometer basically restrains the motion of the proof mass at a certain point, which is usually its rest position. And instead of measuring the capacitance difference between the two electrodes like in the open-loop case; the force required to stop the proof mass motion under the effect of applied acceleration is measured. This counteracting force is usually created through capacitive actuation. In such a case, *the voltage* generating this balancing force is directly related with the applied acceleration by the electromechanical properties of the sensing element. Taking advantage of such relation, the counteracting actuation voltage can be taken into account as the closed-loop output of a force-balancing accelerometer readout circuit. In Figure 2.8, a simplified block diagram for the analog closed-loop force-balancing accelerometer concept is given. Note that with minor differences, this block diagram has the generic form of a typical closed-loop accelerometer as well; either analog or digital.

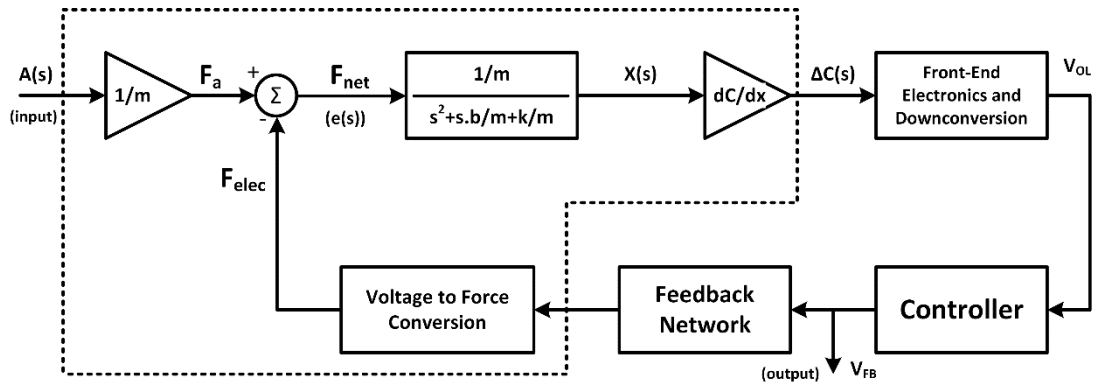


Figure 2.8: The simplified block diagram of the linearized closed-loop, force-balancing capacitive accelerometer in Laplace domain. The blocks in the dashed box are directly related with the electromechanical nature of the MEMS capacitive sensing element.

In Figure 2.8, ‘ $A$ ’ is the applied acceleration; ‘ $F_a$ ’ is the force generated on the proof mass by the applied acceleration; ‘ $F_{elec}$ ’ is the electrostatic force generated on the proof mass by the feedback network of the readout circuit; ‘ $F_{net}$ ’ is the net force acting on the proof mass; ‘ $X$ ’ is the proof mass displacement under the effect of ‘ $F_{net}$ ’; ‘ $\Delta C$ ’ is

the capacitance difference between the two electrode capacitors; ‘ $V_{ol}$ ’ is the output of the front-end readout electronics; ‘ $V_{FB}$ ’ is the feedback voltage used to generate the balancing electrostatic force and also is the output of the closed-loop accelerometer.

As discussed earlier, one of the most fundamental issues related with open-loop accelerometers is their low linearity performance resulting from the inversely proportional relationship between the proof mass displacement and the capacitance difference between the two electrode capacitances. This relation was introduced as the *sensitivity* of the sensor earlier. The sensitivity expressions of each electrode capacitance are re-visited below.

$$\frac{dC_p}{dx} = + \frac{\epsilon * A_{tot}}{(d_{gap} - x)^2} \quad (2.31)$$

$$\frac{dC_n}{dx} = - \frac{\epsilon * A_{tot}}{(d_{gap} + x)^2} \quad (2.32)$$

and,

$$\Delta C = C_p - C_n \quad (2.33)$$

Thus the total sensor sensitivity is:

$$\frac{d\Delta C}{dx} = \frac{\epsilon * A_{tot}}{(d_{gap} - x)^2} + \frac{\epsilon * A_{tot}}{(d_{gap} + x)^2} \quad (2.34)$$

which is a highly non-linear function of proof mass displacement,  $x$ .

Given that the readout circuit provides closed-loop operation by restraining the motion of the proof mass, the proof mass displacement ‘ $x$ ’ will ideally be zero. Even though such precision impractical, this displacement will yield much smaller values compared to the capacitive finger separation ‘ $d_{gap}$ ’ if not precisely zero. Thus, with a safe assumption, the effect of the proof mass displacement on the total sensor sensitivity during closed-loop operation can be neglected. As to say,

$$x \cong 0$$

$$\frac{d\Delta C}{dx} \cong \frac{\epsilon * A_{tot}}{(d_{gap} - 0)^2} + \frac{\epsilon * A_{tot}}{(d_{gap} + 0)^2} \quad (2.35)$$

$$\frac{d\Delta C}{dx} \cong \frac{2 * \epsilon * A_{tot}}{d_{gap}^2} \quad (2.36)$$

similarly,

$$\frac{dC}{dx} = \frac{dC_p}{dx} = \frac{dC_n}{dx} \cong \frac{\epsilon A_{tot}}{d_{gap}^2} \quad (2.37)$$

As Equations 2.36 and 2.37 imply, each electrode capacitance's sensitivity,  $dC/dx$ ; and the total sensitivity of the sensing element,  $d\Delta C/dx$ , can be assumed to be *constant* given that it is operated using a closed-loop readout circuit. This principle of operation is what linearizes the response of closed-loop analog accelerometer as presented in this thesis, and it also justifies the linearized system model in Figure 2.8.

Moreover, since the proof mass displacement and thus the capacitance difference between the two electrodes are negligibly small during operation, the gain of the pre-amplifier can be increased further without any concerns about the operation range and the supply rails of the system. This way, the noise contributions of the electrical blocks following the pre-amplification stage can be suppressed further. Eventually, the overall noise performance of the readout circuit will also be improved without any reduction in the operation range unlike the open-loop case.

Another important aspect of a closed-loop accelerometer that should be noted is related with the state of the suspending springs during operation. During open-loop operation, the total displacement of the proof mass under the effect of acceleration is defined by the stiffness of the mechanical springs that are suspending the proof mass (Section 2.1, Equation 2.12). However, since the proof mass is ideally kept steady at its rest position ( $x \approx 0$ ) during closed-loop operation, the springs will not be loaded at all ( $k \cdot x \approx 0$ ). And since the springs do not exert any force on the proof mass in steady state, they do not take any significant part in the static response of the system.

The advantages of a closed-loop accelerometer against an open-loop one are clear. As discussed earlier, the closed-loop operation in capacitive MEMS accelerometers are usually achieved through capacitive actuation. The fundamental principles of capacitive actuation and the details of the linear, bidirectional electrostatic force-feedback method used in the proposed system are discussed in further sub-sections.

### 2.3.1. Capacitive Actuation

In order to balance the forces exerted on the proof mass by the input acceleration and achieve closed-loop operation, capacitive actuation is used. Electrostatic forces generated between two oppositely charged nodes of a parallel-plate capacitor is what creates this actuation and thus makes the force-balancing action possible.

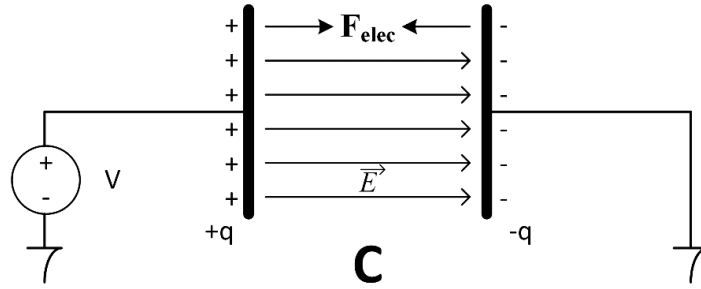


Figure 2.9: A demonstration of the electrostatic forces between the two plates of a parallel-plate capacitor.

The electrostatic force created between two capacitive plates can be formulated using several methods. One of these methods is by the multiplication of the electric charge on either plate and the electric field between the two plates:

$$F_{elec} = Q * \frac{Q}{2 * A * \epsilon} \quad (2.38)$$

and,

$$Q = C * V = \frac{\epsilon A}{d} * V \quad (2.39)$$

where ‘ $Q$ ’ is the charge of either plate; ‘ $A$ ’ is the overlap area of the parallel-plate capacitor; ‘ $\epsilon$ ’ is the permittivity of air; ‘ $C$ ’ is the capacitance generated by the two parallel plates; ‘ $V$ ’ is the voltage applied across the two plates of the capacitor; and ‘ $d$ ’ is the plate separation.

Combining Equation 2.38 and equation 2.39, the force equation can be re-arranged as follows:

$$F_{elec} = \frac{1}{2} * \frac{\epsilon A}{d^2} * V^2 \quad (2.40)$$

Note that the second term in the multiplication in Equation 2.40 is the sensitivity of the parallel-plate capacitor as it was defined earlier. So the electrostatic force expression can be further reduced to the following form:

$$F_{elec} = \frac{1}{2} * \frac{dC}{dx} * V^2 \quad (2.41)$$

Using the voltage generated at the output of the closed-loop circuit ( $V_{FB}$ , Figure 2.8), and using a feedback network to feed this voltage back to the sensing element, such a force can be created. And the motion of the proof mass under the effects of an input acceleration can be counteracted. However, even though the sensitivity of the sensor can be assumed constant and the sensing interface can be linearized by closed-loop operation, the quadratic behavior of this electrostatic force causes another source of non-linearity. This can be simply studied as follows.

Given that the force acting on the proof mass input by acceleration ‘ $a$ ’ is

$$F_a = m * a \quad (2.42)$$

and if this force is to be counteracted by one of the electrodes’ capacitances through the voltage  $V_{FB}$ , the force equilibrium expression would be

$$F_a = F_{elec} \quad (2.43)$$

$$m * a = \frac{1}{2} * \frac{dC}{dx} * V_{FB}^2 \quad (2.44)$$

the relation between the input ‘ $a$ ’ and the output ‘ $V_{FB}$ ’ of the system, yet again, becomes non-linear. Additionally, the force generated between two parallel plates can only be used pull the plates closer to each other, and the opposite is not possible. So using only one electrode capacitance will not be sufficient to counteract acceleration input in *either* direction; at least in this configuration.

Note that the mechanical spring loading forces are not included in these force equilibrium expressions since the proof mass displacement ‘ $x$ ’ is zero and thus the spring force  $k*x$  is zero as well.

The solution to the aforementioned linearity and directionality issues will be introduced in the next sub-section.

### 2.3.2. Differential, Bidirectional Capacitive Actuation

In the proposed system, the actuation voltage ' $V_{FB}$ ' is applied onto the two electrodes differentially in a special configuration. This configuration is demonstrated in Figure 2.10. By using such a configuration, the force-feedback action can be linearized. Additionally, this way the electrostatic actuation can be made bidirectional: the acceleration input can be counteracted in both directions.

The proof mass node of the sensing element is assumed to be connected to the ground. This is a solid assumption considering that it is virtually grounded by the inverting input of the pre-amplifier (Figure 2.7). Voltage ' $V_{PM}$ ' in Figure 2.10 is referred as the *proof mass voltage*, and it is applied symmetrically on both electrodes. Resultantly, by the effect of this proof mass voltage, electrostatic pulling forces of equal magnitude and opposite directions are applied on the proof mass through both of the electrode capacitances. Being equal, these *offset* forces do not cause any net force on the proof mass given that the feedback voltage,  $V_{FB}$ , is zero. However, by increasing or decreasing the voltages on either electrode differentially through the  $V_{FB}$  voltage, a non-zero force on either direction can be applied on the proof mass. Thus, bidirectional force-balancing can be achieved.

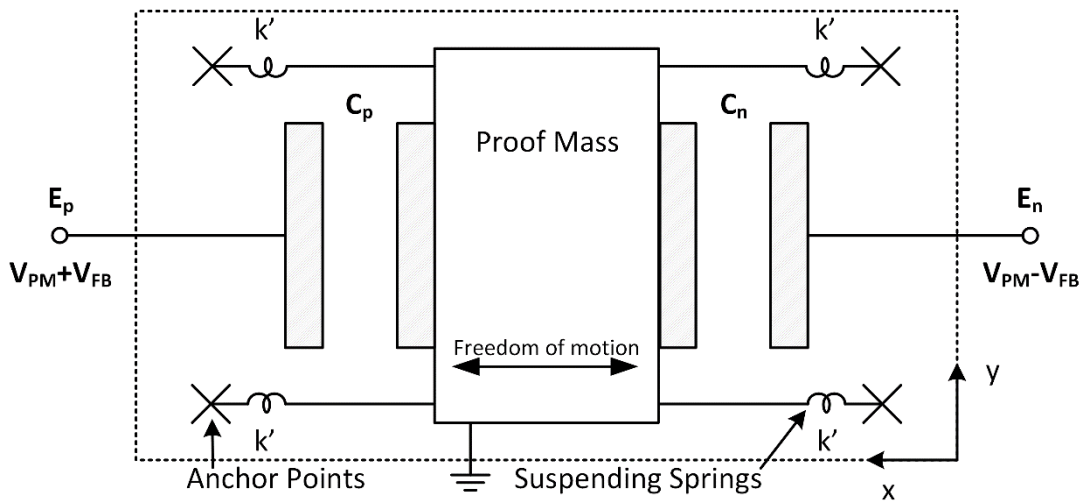


Figure 2.10: Simplified electromechanical model of the sensing element demonstrating the application of force-feedback voltages. The feedback voltage  $V_{FB}$  is applied onto the sensor electrodes differentially, accompanied by a fixed DC voltage,

$V_{PM}$ . By using such a configuration, the force-feedback action can be linearized and the acceleration can be counteracted in both directions. The force exerted on the proof mass in  $x$  direction by an external acceleration is counteracted by decreasing the  $V_{FB}$  voltage below zero. Oppositely, if the force by acceleration is applied in  $-x$  direction, then  $V_{FB}$  voltage is increased above zero.

In order to understand this force-feedback concept better, and to demonstrate its linear behavior, following equations can be used.

The electrostatic forces acting on the proof mass, by the positive ( $E_p$ ) and the negative electrode ( $E_n$ ) respectively, are as follows:

$$F_p = \frac{1}{2} * \frac{dC_p}{dx} * (V_{PM} + V_{FB})^2 \quad (2.45)$$

$$F_n = \frac{1}{2} * \frac{dC_n}{dx} * (V_{PM} - V_{FB})^2 \quad (2.46)$$

Assuming both electrodes have the same sensitivity,  $dC/dx$ , the net electrostatic force applied on the proof mass is

$$F_{e,net} = \frac{1}{2} * \frac{dC}{dx} * [(V_{PM} + V_{FB})^2 - (V_{PM} - V_{FB})^2] \quad (2.47)$$

$$F_{e,net} = \frac{1}{2} * \frac{dC}{dx} * [2V_{PM} * 2V_{FB}] \quad (2.48)$$

$$F_{e,net} = 2 \frac{dC}{dx} V_{PM} * V_{FB} \quad (2.49)$$

Considering this net electrostatic force in Equation 2.49 is used to counteract an external force applied by an acceleration input 'a', the force equilibrium expression can be written as follows:

$$F_{a,ext} = F_{e,net} \quad (2.50)$$

$$m * a = 2 \frac{dC}{dx} V_{PM} * V_{FB} \quad (2.51)$$

Thus the relation between the input, 'a', and the output ' $V_{FB}$ ' is

$$\frac{V_{FB}}{a} = \frac{m}{2 \frac{dC}{dx} V_{PM}} \quad (2.52)$$

The terms in the right-hand-side in Equation 2.52 are all at constant values. This implies a completely linear relation between the input and the output of the system as desired. Note that this constant on the right-hand-side is nothing but the *scale factor* of the system.

### 2.3.3. Electrostatic Spring Effect and the Operation Range Estimation

As discussed earlier, the spring stiffness does not have a significant role on the static response of the system. However, it actually is a critically important design parameter when it comes to accomplishing the loop stability. In addition to the stiffness of the mechanical springs suspending the proof mass, the phenomenon referred as *electrostatic spring softening* should also be taken into account. This softening effect occurs as a result of the electrostatic forces exerted on the proof mass through the electrodes. It is not easy to comprehend this effect while assuming the displacement of the proof mass during closed-loop operation as zero because such assumption simply leaves the mechanical spring constant out of the equation.

In order to visualize the electrostatic spring softening effect, a force equilibrium expression including the spring loads is more than useful. While writing this expression, a virtual external force  $F_{ext}$  is assumed to be applied on the proof mass in +x-direction. Note that all the signs and terms used in this expression are in accordance with the denotation in Figure 2.10.

$$F_{ext} + |F_{e,p}| = k_{mech} * x + |F_{e,n}| \quad (2.53)$$

where ' $|F_{e,p}|$ ' and ' $|F_{e,n}|$ ' are the amplitudes of the electrostatic forces applied on the proof mass by the positive and the negative electrodes respectively; ' $k_{mech}$ ' is the mechanical spring constant of all the suspending springs combined; ' $x$ ' is the proof mass displacement.

Equation 2.53 can be extended and re-arranged as follows:

$$F_{ext} = k_{mech} * x + |F_{e,n}| - |F_{e,p}| \quad (2.54)$$

$$F_{ext} = k_{mech}x + \left| \frac{1}{2} \frac{dC_n}{dx} (V_{PM} - V_{FB})^2 \right| - \left| \frac{1}{2} \frac{dC_p}{dx} (V_{PM} + V_{FB})^2 \right| \quad (2.55)$$

where,

$$C_n(x) = \frac{\epsilon A}{(d+x)} \quad \text{and} \quad C_p(x) = \frac{\epsilon A}{(d-x)} \quad (2.56-57)$$

Inserting Equations 2.56-57 into Equation 2.55,

$$F_{ext} = k_{mech}x + \frac{1}{2} \frac{\epsilon A}{(d+x)^2} (V_{PM} - V_{FB})^2 - \frac{1}{2} \frac{\epsilon A}{(d-x)^2} (V_{PM} + V_{FB})^2 \quad (2.58)$$

$F_{ext}$  can be assumed to have the following form where  $k_{eff}$  is a constant:

$$F_{ext} = k_{eff} * x \quad (2.59)$$

Then,

$$k_{eff} * x = k_{mech}x + \frac{1}{2} \frac{\epsilon A}{(d+x)^2} (V_{PM} - V_{FB})^2 - \frac{1}{2} \frac{\epsilon A}{(d-x)^2} (V_{PM} + V_{FB})^2 \quad (2.60)$$

If both sides of Equation 2.60 are differentiated by  $x$ ,

$$k_{eff} = k_{mech} - \frac{\epsilon A}{(d+x)^3} (V_{PM} - V_{FB})^2 - \frac{\epsilon A}{(d-x)^3} (V_{PM} + V_{FB})^2 \quad (2.61)$$

,and Equation 2.61 is evaluated at  $x=0$ , which is the operation point of the accelerometer in closed-loop.

$$k_{eff} = k_{mech} - 2 \frac{\epsilon A}{d^3} (V_{PM}^2 + V_{FB}^2) \quad (2.62)$$

By taking the derivative of the virtual external force with respect to the displacement, a term analogous to the spring constant is obtained. As also seen in the Equation 2.62, this constant is not equal to the mechanical spring constant,  $k_{mech}$ . Even if the feedback voltage is zero and the proof mass is pulled from both of the electrodes equally by  $V_{PM}$ , the outcome of the derivation is still different from  $k_{mech}$ . This new spring constant value,  $k_{eff}$ , is less than the mechanical spring constant and is a result of the electrostatic spring softening phenomenon.

The decrement in the mechanical spring constant will be referred as the *electrostatic spring constant* of the sensing element:

$$k_{elec} = 2 \frac{\epsilon A}{d^3} (V_{PM}^2 + V_{FB}^2) \quad (2.63)$$

The overall spring constant,  $k_{eff}$ , affecting the dynamic behavior of the sensing element will be referred as *effective spring constant*:

$$k_{eff} = k_{mech} - k_{elec} \quad (2.64)$$

Thus the transfer function of the sensing element,  $K(s)$ , can be re-written as follows:

$$K(s) = \frac{X(s)}{F(s)} = \frac{1/m}{s^2 + \frac{b}{m}s + \frac{k_{eff}}{m}} \quad (2.65)$$

As long as the proof mass voltage is kept sufficiently high compared to the feedback voltage, the effect of the feedback voltage on the effective spring constant value can be neglected. Based on this approach, the dominant term setting the value of the electrostatic spring constant is considered as the proof mass voltage throughout this work. However, if the frequency response of the accelerometer under the effects of high acceleration inputs (meaning high values for  $V_{FB}$ ) is to be studied, then such approximation critically insufficient, and should not be used.

The modification in the spring constant naturally alters dynamic behavior the of the accelerometer, affecting critical properties such as loop gain and quality factor. Thus the closed-loop response and the loop stability should be considered taking the *effective spring constant* into account. At this point it is better be noted that by changing the proof mass voltage value, the phase margin of the overall system can be tuned since it directly affects the loop gain. Additionally, by forcing the effective spring constant to smaller values, the noise performance can also be increased by exploiting the increase in the sensor's base-band gain.

Besides these considerations, increasing proof mass voltage,  $V_{PM}$ , above a certain value causes the effective spring constant to drop below zero. Such situation causes a response like a positive feedback system, and results in *pull-in* [30] in the sensing element, and saturates the output of the loop. The critical proof mass voltage value

resulting in a zero ' $k_{eff}$ ' is expressed below, and the relation in Equation 2.67 should always be satisfied. Note that when calculating the maximum operation range of the accelerometer, the effect of the feedback voltage,  $V_{FB}$ , on spring softening should also be considered since it will have values comparable to  $V_{PM}$  then.

$$V_{PM,crit} = \sqrt{k_{mech} * \frac{d^3}{2\epsilon A}} \quad (2.66)$$

$$V_{PM} < V_{PM,crit} \quad (2.67)$$

Figure 2.11 demonstrates the magnitudes of the spring loading force, electrostatic force and the net force acting on the proof mass when it is moved by an external force along x-axis. The slopes of each line at the origin shows the mechanical, electrostatic and the effective spring constants respectively.

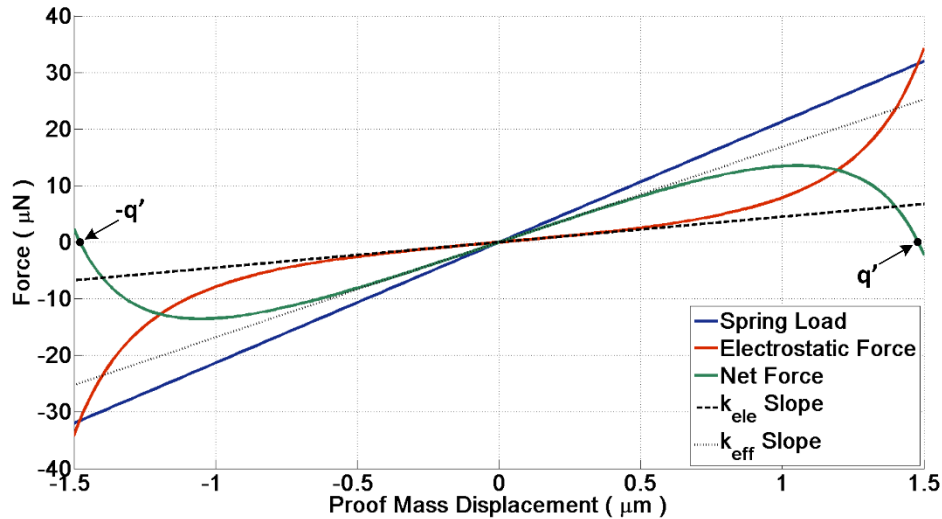


Figure 2.11: Visual representation of the electrostatic spring softening effect. The slopes of each line at the origin ( $x=0$ ) are equal to the corresponding spring constants. Note that beyond points  $q'$  and  $-q'$ , the net force acting on the proof mass changes its signature indicating a pull-in situation.

### 2.3.4. Operation Range Considerations

The strong relation between the electrostatic spring constant, the value of the proof mass voltage, and the scale factor of the system (Equation 2.52) is a defining factor for

the *absolute maximum* operation range of the closed-loop accelerometer. Additionally, as by the principles behind differential force-feedback, the maximum value the feedback voltage,  $V_{FB}$ , can get is equal to the proof mass voltage,  $V_{PM}$ . Because then, the actuation voltage on one electrode becomes zero, and increasing  $V_{FB}$  further disrupts the trend of the force applied through the associated electrode. Analyzing these considerations, the operation range, ‘ $R$ ’, and the absolute maximum value for the range can be derived with the following equations:

$$R = \frac{V_{FB,max}}{SF} = \frac{V_{PM}}{SF} \quad (m/s^2) \quad (2.68)$$

where, ‘ $SF$ ’ is the scale factor of the system. As derived before (Equation 2.52) it is:

$$SF = \frac{m}{2\frac{dC}{dx}V_{PM}} \left( V / \frac{m}{s^2} \right) \quad (2.69)$$

Substituting Equation 2.69 into Equation 2.68:

$$V_{PM}^2 = \frac{R*m}{2\frac{dC}{dx}} \quad (2.70)$$

In order not to cause the effective spring constant to drop below zero assuming the maximum acceleration input is applied, the following relation should as well be satisfied (Equation 2.63):

$$V_{PM}^2 + V_{FB,max}^2 < k_{mech} * \frac{d^3}{2\epsilon A} \quad (2.71)$$

where,

$$V_{FB,max} = V_{PM} \quad (2.72)$$

Thus, Equation 2.71 can be rearranged as follows demonstrating the absolute maximum possible range of operation:

$$R < \frac{k_{mech}d}{2m} \quad (2.73)$$

## 2.4. Simultaneous Differential Sensing and Force-Feedback

Approaches for capacitive differential sensing and differential force-feedback topics are discussed in detail so far. The method for fusing these aspects of the analog accelerometer in continuous-time operation is to be introduced in this section.

One approach, as also seen in the literature, is by using dedicated differential capacitance sets for each task. In other words, two differential electrodes can be used for sensing while another two can be used for force-feedback. Figure 2.12 demonstrates the configuration for such approach.

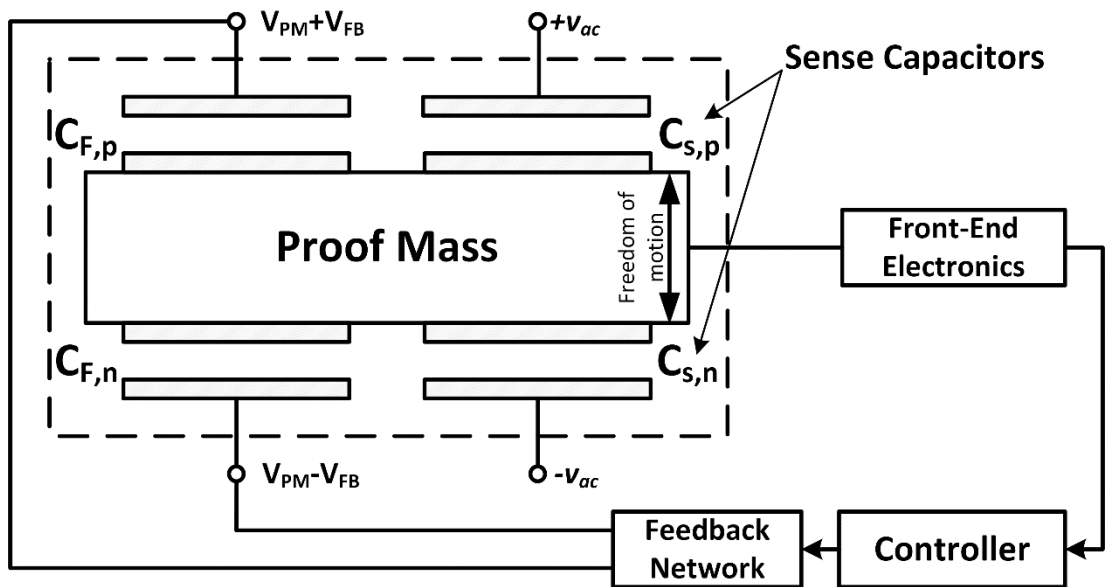


Figure 2.12: Continuous-time, closed-loop accelerometer approach incorporating two sets of differential electrodes. In this configuration, the electrode set composed of  $C_{F,p}$  and  $C_{F,n}$  is used for electrostatic force-feedback while the other set is used for acceleration sensing.

Using dedicated electrode sets for either task is a neat and straight-forward approach. However, it can be considered costly in terms of *effective acceleration sensitivity per unit chip area*. This is because a part of the sensing element will only be used for force-feedback in such case, and the acceleration sensing electrodes will be limited with a smaller chip area compared to a case in which the chip was composed of sensing electrodes only.

In the following sub-sections, the solution which offers continuous-time closed-loop acceleration sensing without any reduction in the effective sensitivity per chip area is introduced.

### 2.4.1. Simultaneous Sensing and Force-Feedback with a Single Electrode Set

It is mentioned earlier by the end of Section 2.1 that the sensing element is actually an electrical high-pass filter and a mechanical low-pass filter: As the frequency of the electrical signals applied on the electrodes increase, more current can flow through the electrode capacitances; and if a very low-frequency voltage is applied on them, the current will be mostly blocked by the capacitors. This is why the sensor is referred as an electrical high-pass filter. On the other hand, as the frequency of the force applied on the proof mass increases, the output proof mass displacement will start to decrease rapidly after a certain *corner frequency* (Equation 2.15). Recall that the input force can be applied on the proof mass electrically. This electromechanical property of the sensing element is exploited to achieve simultaneous sensing and force-feedback using a single pair of differential electrodes.

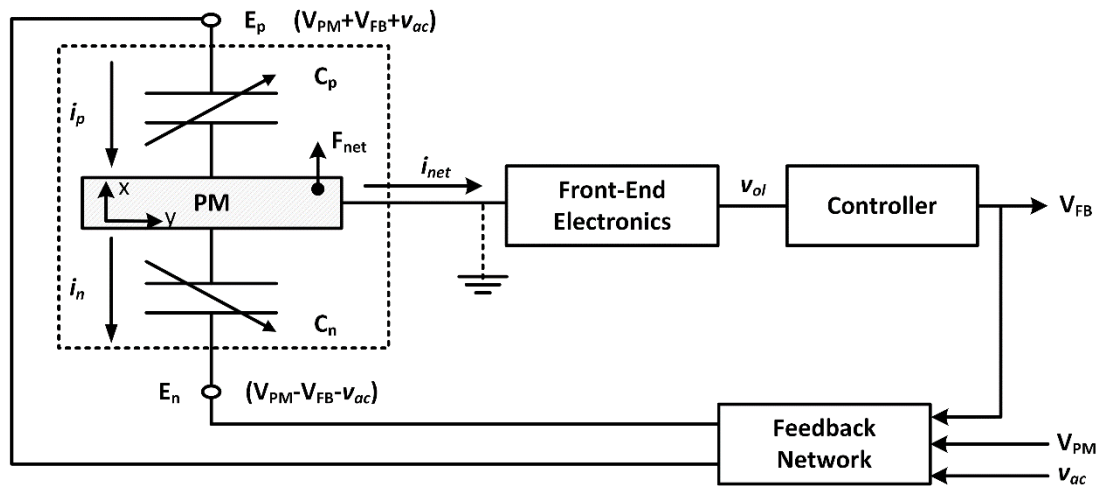


Figure 2.13: A conceptual circuit diagram for the analog force-feedback accelerometer. By using such a configuration to apply both sensing and feedback voltages on the electrodes, simultaneous differential sensing and force-feedback can be achieved in continuous-time using only one pair of differential electrodes.

In Figure 2.13, voltages applied on the electrodes for simultaneous sensing and force-feedback purpose is demonstrated along with the complete conceptual circuit diagram of the proposed system. Taking either one of the electrode capacitances and having a closer look at the current flowing through it; and electrostatic forces exerted on the proof mass by it, simultaneous operation can be observed easily.

To start with the sensing part of the approach, the current flowing through the positive capacitance is

$$i_p = C_p(t) \frac{d(v_p)}{dt} \quad (2.74)$$

$$i_p = C_p(t) \left( \frac{d(V_{PM})}{dt} + \frac{d(V_{FB})}{dt} + \frac{d(v_{ac})}{dt} \right) \quad (2.75)$$

Since ‘ $V_{PM}$ ’ is a fixed voltage with zero time-derivative,

$$i_p = C_p(t) \left( \frac{d(V_{FB})}{dt} + \frac{d(v_{ac})}{dt} \right) \quad (2.76)$$

For an acceleration applied at the maximum operating frequency, ‘ $w_{max}$ ’, feedback voltage ‘ $V_{FB}$ ’ can be assumed to have the following form:

$$V_{FB} = p * \sin(w_{max}t + \varphi_f) \quad (2.77)$$

, and the carrier signal,  $v_{ac}$ , is

$$v_{ac} = a * \sin(w_c t + \varphi_c) \quad (2.78)$$

Then Equation 2.76 becomes

$$i_p = C_p(t) [k w_{max} \cos(w_{max}t + \varphi_f) + a w_c \cos(w_c t + \varphi_c)] \quad (2.79)$$

Before continuing on with the simplification of the expression in Equation 2.79, a couple of considerations can be done. First and the most important of all, the frequency of the carrier signal,  $w_c$ , is set to be much higher than the maximum operation frequency,  $w_{max}$ . Also the scaling factor,  $p$ , can be smaller than the amplitude of the carrier signal,  $a$ . Thus the first term of the summation inside brackets can be considered to be much smaller than the second term.

Additionally, the high-pass filter following the pre-amplification step is set to filter the signals at lower frequencies compared to the carrier frequency. This effectively

reduces the significance of the first term further. Moreover, the low-frequency signal components entering the demodulation phase cannot be down-converted to base-band during demodulation. On the contrary, they are modulated up to higher frequencies, and during the low-pass filtering after demodulation, these signals are filtered out again. This can be observed by inserting  $\cos(w_{max}t + \varphi_f)$  into Equation 2.27 in the stead of the carrier signal. So it is be safe to make the following assumption:

$$i_p \cong aw_c \cos(w_c t + \varphi_c) C_p(t) \quad (2.80)$$

Similarly,

$$i_n \cong aw_c \cos(w_c t + \varphi_c) C_n(t) \quad (2.81)$$

So the actuating feedback voltage and the proof mass voltage can be effectively assumed to have no contribution to the net readout current,  $i_{net}$ .

On the other hand, the total net electrostatic feedback force acting on the proof mass can be formulated as follows:

$$F_{net,e} = \frac{1}{2} \frac{dC_p}{dx} (V_{PM} + V_{FB} + v_{ac})^2 - \frac{1}{2} \frac{dC_n}{dx} (V_{PM} - V_{FB} - v_{ac})^2 \quad (2.82)$$

$$F_{net,e} = \frac{1}{2} \frac{dC}{dx} [(V_{PM} + V_{FB} + v_{ac})^2 - (V_{PM} - V_{FB} - v_{ac})^2] \quad (2.83)$$

$$F_{net,e} = \frac{1}{2} \frac{dC}{dx} [(2V_{FB} + 2v_{ac})(2V_{PM})] \quad (2.84)$$

$$F_{net,e} = 2 \frac{dC}{dx} V_{PM} V_{FB} + 2 \frac{dC}{dx} V_{PM} v_{ac} \quad (2.85)$$

As it is seen in Equation 2.85 the carrier signal,  $v_{ac}$ , also has an undesirable contribution to the net electrostatic force acting on the proof mass. The effect of this parasitic high-frequency force component on the sensing element causes undesired vibrations on the proof mass referred as *mass residual motion*. If the frequency of the carrier signal is set to be much higher than the corner frequency of the sensing element's mechanical transfer function, then the effects of this residual the force and thus vibrations, can be suppressed significantly. Thus the net electrostatic force can be assumed to be

$$F_{net,e} \cong 2 \frac{dC}{dx} V_{PM} V_{FB} \quad (2.86)$$

As it is also demonstrated by the Equations 2.80-81 and 2.86, using the configuration as demonstrated in Figure 2.13, force-feedback and sensing can be achieved using only one pair of differential electrodes in continuous-time.

## **2.5. Summary and Conclusions**

Theoretical approach for a force-balancing closed-loop accelerometer readout circuit, which works in continuous-time, is introduced, and the details of the operation principles are discussed throughout this chapter.

The functionality and the feasibility of each building block is verified theoretically. The building blocks starting from modulation in the sensing element followed by pre-amplification, high-pass filtering and buffering, demodulation, and ending with low-pass filtering are shown to form an open-loop accelerometer, which can be extended to a closed-loop system by using a controller and a feedback network to counteract the force exerted on the proof mass by the acceleration. A number of important aspects like the mass residual motion, operation range, and the electrostatic spring softening are introduced as points to be paid attention to. In conclusion, it can be said that by using such a closed-loop system, the acceleration can be sensed linearly with minimal system complexity.

In the next chapter, the system-level modelling of the approach as presented in this chapter is introduced in a numerical fashion.



## **CHAPTER 3**

### **SYSTEM-LEVEL DESIGN AND MODELLING**

The operation principles of the proposed closed-loop accelerometer are introduced and discussed in the previous chapter. Before going on with the implementation of the system, MATLAB Simulink models of the complete system are created. In this chapter, these models and the simulation results based on them are introduced along with the related design parameters. The simplification and linearization methods used during creation of these models and the controller design approach are also discussed in this chapter. In Section 3.1, the non-linear simulation models of the building blocks of the sensing element and the open-loop readout electronics are introduced. In Section 3.2, the design of the linear model, which is necessary for frequency domain analyses steps, is introduced in detail. Section 3.3, the design approach for the controller to be used to close the accelerometer loop is presented followed by stability considerations for the proposed system. Section 3.4 focuses on the demonstration of the accelerometer both in open- and closed-loop configurations. The chapter ends with a brief conclusion in Section 3.5.

#### **3.1. Design and Modelling of the Building Blocks**

In the following sub-sections, the design procedure of the models for both the sensing element and the open-loop readout electronics are introduced and discussed in detail. The models introduced in this section are designed as accurate as the complete mathematical relations affecting the operation of the modelled blocks without any simplification or assumptions. Because of this, the transient time simulations are also based on the models as presented in this section.

### 3.1.1. Non-linear Model of the Sensing Element

Even though certain simplifications and assumptions are made to estimate the response of the sensing element as presented in Chapter 2, a non-linear model including all the details affecting the operation is useful for such model would reveal overlooked aspects if there are any. These details include spring softening by the contribution of the feedback voltage and the carrier signal, effect of the anti-gap capacitances, and the non-linear behavior of the sensor. In Figure 3.1, the non-linear model of the sensing element is presented.

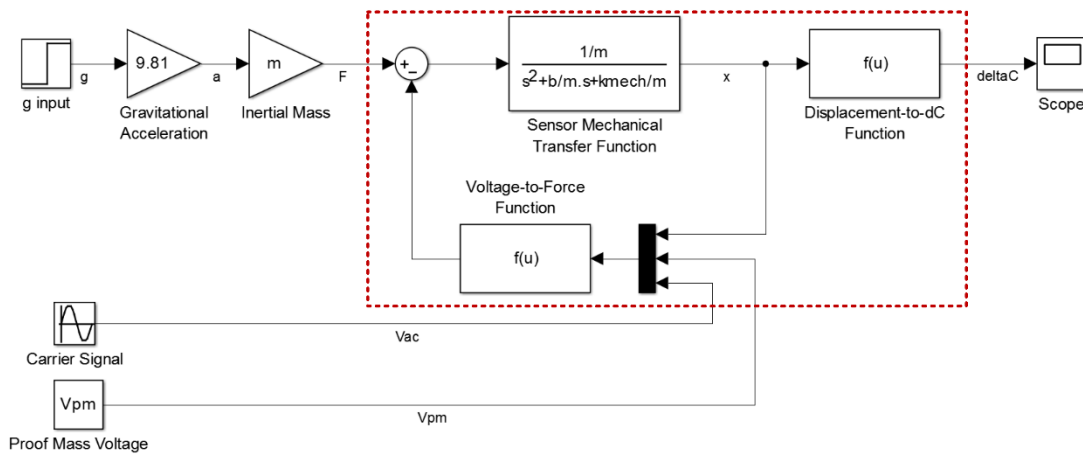


Figure 3.1: The non-linear model of the sensing element (dashed box). The input acceleration is in ‘g’ units. The two function blocks include non-linear functions of the applied electrostatic forces (Voltage-to-Force) and the capacitance difference between the two electrodes (Displacement-to-deltaC). Output of the sensor is taken as the capacitance difference, deltaC ( $\Delta C$ ), between the two differential electrodes.

The ‘Displacement-to- $\Delta C$ ’ function block contains the formula for calculating the capacitance difference between the two differential electrodes including the effects of the anti-gap separations. The ‘Voltage-to-Force’ block contains the formula for calculating the net electrostatic force exerted on the proof mass as a function of proof mass displacement,  $x$ , and the electrode potentials  $V_{PM} + V_{ac}$  and  $V_{PM} - V_{ac}$ . Note that by using such a feedback block, the electrostatic spring softening effect can directly be simulated since it already is a phenomenon resulting from the change in the net electrostatic force exerted on the mass with the changing proof mass displacement

(Chapter 2, Section 2.3.3). This way the transfer function modelling the mechanical dynamic response of the sensing element can be prepared based solely on the mechanical spring constant,  $k_{mech}$ , but the spring softening effect can still be included in the simulations. Equations inside the two function blocks are presented below for the sake of completeness.

$$V\text{-to-}F(x, V_{PM}, v_{ac}) = \frac{\epsilon A}{2} \left[ \left( \frac{1}{(d_{gap} - x)^2} - \frac{1}{(d_{a-gap} + x)^2} \right) (V_{PM} + v_{ac})^2 - \left( \frac{1}{(d_{gap} + x)^2} - \frac{1}{(d_{a-gap} - x)^2} \right) (V_{PM} - v_{ac})^2 \right]$$

$$x\text{-to-}\Delta C(x) = \epsilon A * \left[ \left( \frac{1}{d_{gap} - x} + \frac{1}{d_{a-gap} + x} \right) - \left( \frac{1}{d_{gap} + x} + \frac{1}{d_{a-gap} - x} \right) \right]$$

In Table 3.1, the geometrical design values of the sensing element is presented along with the constants used in the simulations.

*Table 3.1: The geometrical design parameters and their values. The properties such as the sensitivity of the sensor, which can be calculated using the parameters given in the table, are not included.*

Parameter	Description	Value	Parameter	Description	Value
t	Microstructure thickness	40 $\mu\text{m}$	w <sub>s</sub>	Spring width	18 $\mu\text{m}$
d <sub>gap</sub>	Gap separation	2 $\mu\text{m}$	l <sub>s</sub>	Spring length	850 $\mu\text{m}$
d <sub>a-gap</sub>	Anti-gap separation	6 $\mu\text{m}$	N <sub>s</sub>	Number of springs	4
l <sub>f</sub>	Finger overlap length	95 $\mu\text{m}$	f <sub>R</sub>	Resonance frequency	3.7 kHz
N <sub>f</sub>	Number of fingers (each electrode)	258	m	Inertial mass	0.3 mg
$\epsilon$	Permittivity of air	8.85 pF/m	b	Damping coefficient	0.0023 Ns/m
E	Young's modulus	169 GPa	k <sub>mech</sub>	Mechanical spring constant	160 N/m

Apart from the geometrical properties of the sensing element, there three electrical configuration parameters which should be decided: the proof mass voltage, the frequency of the carrier signal, and the amplitude of the carrier signal.

The critical proof mass voltage that causes a zero effective spring constant is calculated as shown in Equation 3.1. Note that this is the maximum value the proof mass voltage should be set to.

$$V_{PM,crit} = \sqrt{\frac{k_{mech}}{2\varepsilon A \left( \frac{1}{d_{gap}^3} + \frac{1}{d_{a-gap}^3} \right)}} \cong 8.4 \text{ V} \quad (3.1)$$

The proof mass voltage value for the initial tests was chosen to be 5 V. After the system implementation, the optimum value for the proof mass voltage value is decided to be 5.5 V taking the noise and the range performance tests conducted under different values of  $V_{PM}$  into account. The simulations presented in this chapter is based on this value rather than the initial value.

As it is discussed in Chapter 2-Section 2.4.1, the force component, which is generated by the carrier signal, causing residual motions on the proof mass is:

$$F_{resi} = 2 \frac{dc}{dx} V_{PM} v_{ac} \quad (3.2)$$

The magnitude response of the sensing element is multiplied with the amplitude of this residual force expression to observe the amplitude of the proof mass oscillations with respect to the varying carrier signal frequencies. In Figure 3.2, the resultant plot of this multiplication for a unit carrier signal is shown.

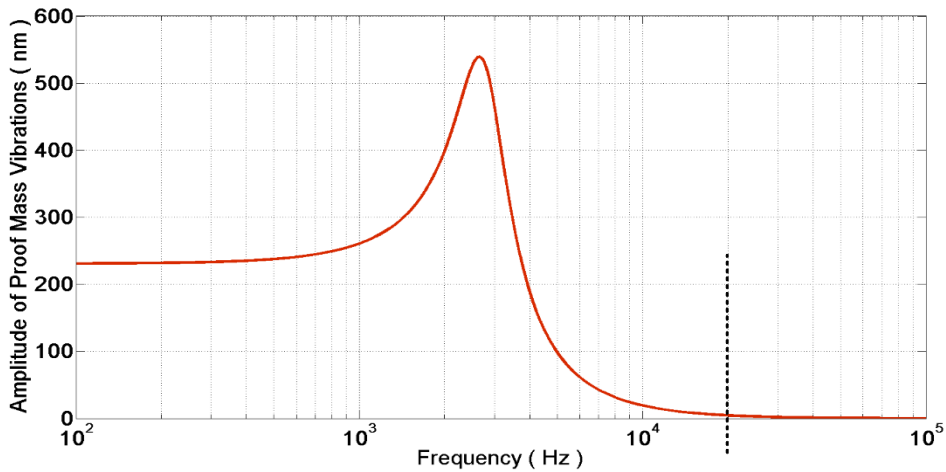


Figure 3.2: The amplitude of residual oscillations of the proof mass as a result of unit amplitude carrier signal under varying frequencies. After the carrier signal frequency exceeds ~20 kHz, the amplitude of the oscillations shrink significantly.

As it can be observed in Figure 3.2 that once the frequency of the carrier signal exceeds around 20 kHz, the amplitude of the mass residual motion oscillations gets significantly small. For this reason, the carrier signal frequency is chosen to be at least 20 kHz, and the tests showed that increasing it further does not have a noticeable effect on the accelerometer performance even degrade the noise performance slightly. Eventually, the final value for the carrier signal frequency is decided to be 20 kHz.

The amplitude of the carrier signal is a neat parameter that can be used to tune the loop gain. Moreover, unlike the proof mass voltage which can also be used to alter the loop gain (Chapter 2, Section 2.4), the carrier signal amplitude does not affect the scale factor of the closed-loop accelerometer (Equation 2.69). The initial value  $1 V_{\text{peak}}$  for this parameter is later modified to  $2.5 V_{\text{peak}}$  after performance tests, and this new value is used in the simulations. In Table 3.2, a summary of the electrical configuration parameters are shown. Note that these values are used both in simulations and the implemented system tests.

*Table 3.2: The electrical configuration parameters used both in the simulations and the circuit implementation.*

<b>Parameter</b>	<b>Description</b>	<b>Value</b>
$V_{\text{PM}}$	Proof mass voltage	$5.5 V_{\text{DC}}$
$f_{\text{ac}}$	Frequency of the carrier signal	20 kHz
$ v_{\text{ac}} $	Amplitude of the carrier signal	$2.5 V_{\text{peak}}$

In Figure 3.3, the step and ramp response simulations of the non-linear sensing element model are demonstrated.

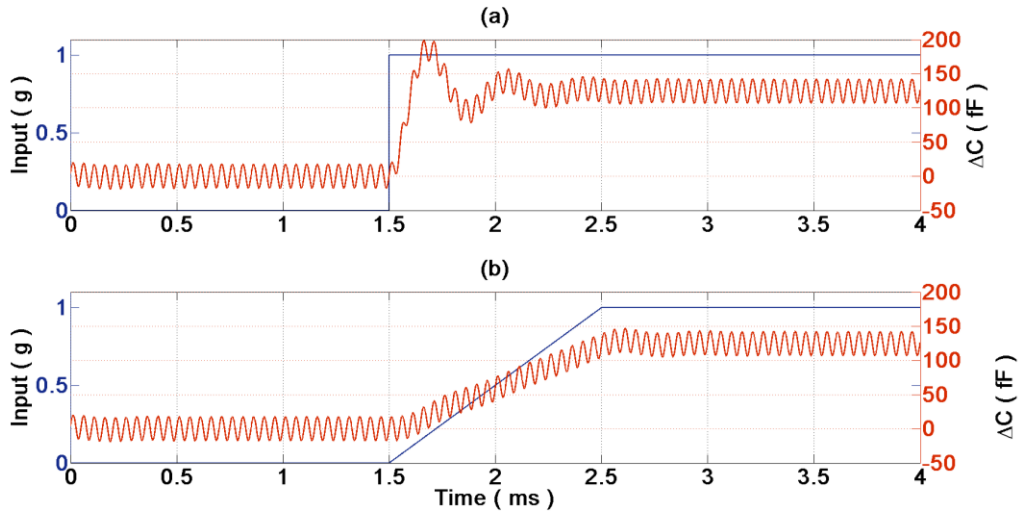


Figure 3.3: (a) Unit step and (b) ramp responses of the non-linear sensing element model. Output of the system is the capacitance difference between the two electrodes,  $\Delta C$ , and the input is acceleration in 'g' units. The oscillations on the output are a result of mass residual motion caused by the 20 kHz carrier signal.

### 3.1.2. Open-Loop Readout Electronics

In addition to pre-amplification, high-pass filtering, demodulation, and low-pass filtering stages, the Simulink model of the front-end readout electronics include the modulation that is taking place on the sensor side as well. In Figure 3.4 this model is presented.

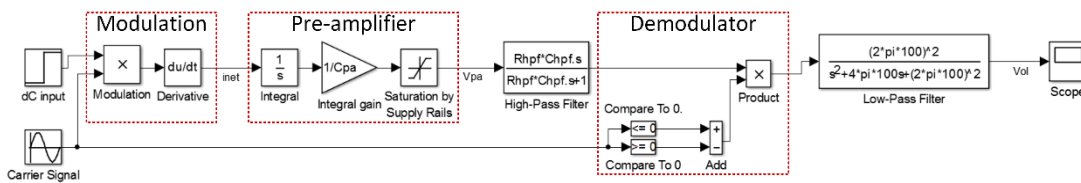


Figure 3.4: The Simulink model of the open-loop readout electronics.

As noted earlier in Chapter 2 Equation 2.19, the net current,  $i_{net}$ , flowing towards the pre-amplification stage is the time derivative of the carrier signal times the capacitance difference between the two electrodes,  $\Delta C$  ( $\Delta C$ ). However during operation, the

changes in  $\Delta C$  can also cause currents leaking through the capacitances, since the net current passing through a capacitor is:

$$i = \frac{d(C(t)*V(t))}{dt} = \frac{dC}{dt} * V + C * \frac{dV}{dt} \quad (3.3)$$

For that reason, even though time derivative of the capacitance does not have a significant effect on the current, it is rather convenient to place the differentiation block in a way that both current components can be observed on the net current,  $i_{net}$ , flowing towards the pre-amplifier.

The pre-amplifier block is created with the combination of an integrator and a gain based on the feedback capacitance. The saturation block following the pre-amplifier output is used to simulate the rail voltages of the operational amplifier which is used to implement the circuit.

The pre-amplification stage is followed by the transfer function of a passive RC high-pass filter with a -3 dB frequency about 500 Hz, and the demodulator. The demodulator block is modelled exactly as it is presented in Figure 2.6 in Chapter 2: A block multiplying the input signal with a unit square-wave. As the final stage of the open-loop electronics following the demodulation stage, a unity-gain, second-order low-pass filter with both poles placed at 100 Hz is used.

In Table 3.3, the component values used both in the model and the implemented circuit of the open-loop electronics is given.

*Table 3.3: Passive component values used in the creation of the Simulink model for the open-loop electronics. Note that these are the actual values that are used in circuit-level implementation as well.*

<b>Component</b>	<b>Description</b>	<b>Value</b>
$C_{PA}$	Pre-amplifier feedback capacitance	3.9 pF
$R_{HPF}$	High-pass filter resistance	36.5 k $\Omega$
$C_{HPF}$	High-pass filter capacitance	10 nF

### 3.2. Model Linearization

The non-linear model as introduced in the previous sub-section, is very useful for simulating the system in time domain with a high accuracy. However, it is not possible to observe the system behavior in frequency domain using such a model for it is composed of several non-linear blocks. Simulations in frequency domain is especially important when a closed-loop system is at stake since the stability of the loop is needs to be ensured by simulations prior to implementation. For this reason, in addition to the non-linear model, an LTI model of the sensing element and the readout electronics is created. In the following sub-sections, these models and the considerations related with them are presented.

#### 3.2.1. Linear Model of the Sensor

The two sources of non-linearity in the model of the sensing element are the *Voltage-to-Force* and the *Displacement-to-deltaC* functions (Figure 3.1). The main reason for these blocks to cause non-linearity in the system is the relation of proof mass displacement,  $x$ , with the varying-gap electrode capacitances. Considering that the accelerometer will be operated in closed-loop, the displacement value can be assumed to be very small, even zero. This way, the non-linearity in the sensing element can be neglected.

*Voltage-to-Force* block introduces non-linearity because it includes non-linear functions of electrostatic forces as a function of proof mass displacement,  $x$ . This block can be eliminated if the mechanical spring constant,  $k_{mech}$ , in the transfer function of the sensing element is replaced with the effective spring constant value,  $k_{eff}$ , as it was discussed in Chapter 2, Section 2.3.3. When it comes to the *Displacement-to-deltaC* block, for very small values of,  $x$ , it can simply be replaced with a gain block, multiplying the proof mass displacement value by a factor of total sensor sensitivity,  $2*dC/dx$ . Taking these considerations into account, an LTI model for the sensing element can be created. In Figure 3.5, this model is presented. Additionally, in Figure 3.6, the comparison of this model with the non-linear model is demonstrated with a step response simulation of both models.

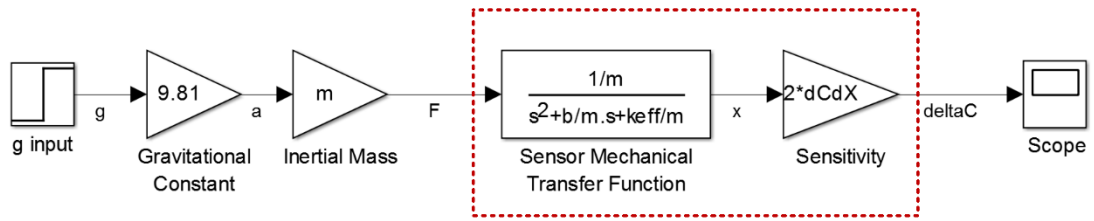


Figure 3.5: The linearized model of the sensing element (dashed box).

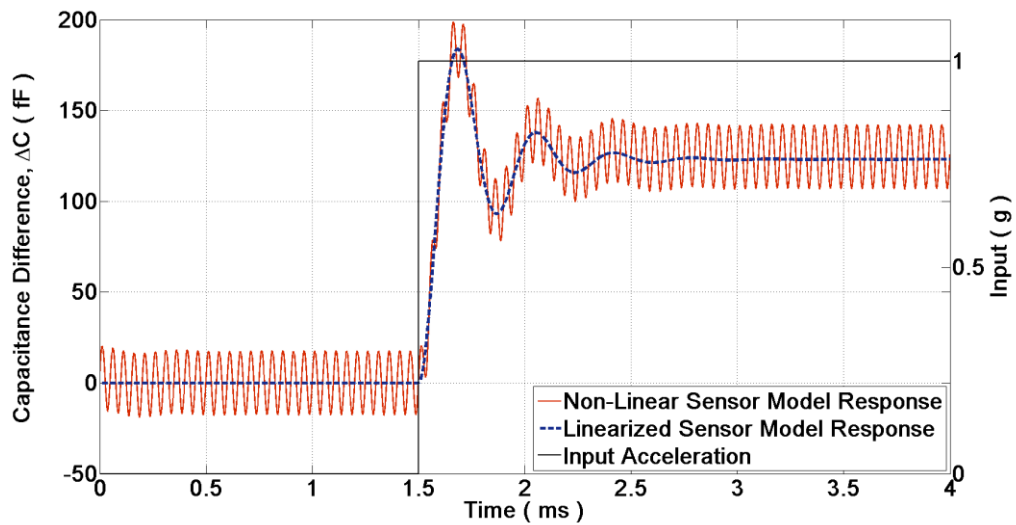


Figure 3.6: Comparison of the unit step responses of the linearized and the non-linear models of the sensing element.

As it can be seen in Figure 3.6, the linearized model is accurate sufficiently. The gain difference between the two models simply is because of the significance of the displacement value under the effect of 1 g acceleration input. If this input is given sufficiently small, then the gains of both models gets much closer to each other.

### 3.2.2. Linear Model of the Open-Loop Readout Electronics

The modulation and demodulation steps as simulated in the non-linear model of the accelerometer needs to be converted into a shape where they can be simulated as an LTI system. In order to make this conversion, it is convenient to recall the gain

expression of the pre-amplifier and the mathematical expression of the demodulation step. As it was presented in Chapter 2, Section 2.2.1, the gain of the pre-amplifier is:

$$G(s) = \frac{V_{pa}}{v_{ac}} = \frac{\Delta C}{C_{pa}} \quad (3.4)$$

and, the carrier signal,  $v_{ac}$ , has the following form:

$$v_{ac} = V_{peak} * \sin(w_c t) \quad (3.5)$$

The output of the front-end electronics for any  $\Delta C$  value can be written as:

$$v_{fe} = \frac{\Delta C(t) * V_{peak}}{C_{pa}} * \sin(w_c t) = a(t) * \sin(w_c t) \quad (3.6)$$

Note that the waveform  $a(t)$  is referred as the *acceleration envelope signal* earlier, and the output of the demodulator has the following form (Chapter 2, Equation 2.29):

$$v_{demod}(t) = \frac{2}{\pi} * a(t) + \left[ -\frac{2}{\pi} a(t) \cos(2w_c t) + \dots \right] \quad (3.7)$$

After the unity-gain low-pass filtering stage, the output of the open loop readout electronics can be expressed as follows:

$$V_{ol}(t) \cong \frac{2}{\pi} * a(t) = \Delta C(t) * \frac{V_{peak}}{C_{pa}} * \frac{2}{\pi} \quad (3.8)$$

As by Equation 3.8, it can be said that the complete open-loop readout electronics can be modelled by a simple gain:

$$G_{ol} = \frac{V_{ol}(t)}{\Delta C(t)} = \frac{V_{peak}}{C_{pa}} * \frac{2}{\pi} \quad (3.9)$$

Additionally, the low-pass filter at the final stage of the open-loop readout circuit is included in the model in order to simulate its contribution to the dynamic behavior of the system. In Figure 3.7, the linearized *envelope model* of the open-loop readout electronics is shown. Also in Figure 3.8, the comparison of this model with the non-linear one is demonstrated with a step response simulation of both models.

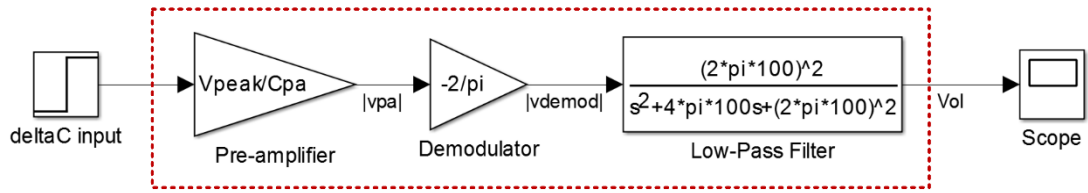


Figure 3.7: The linearized envelope model of the open-loop readout electronics.

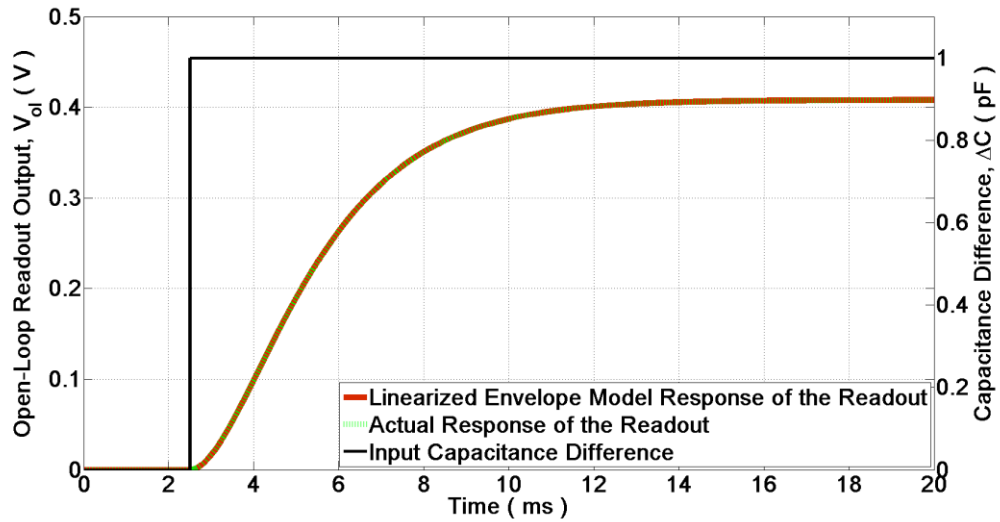


Figure 3.8: The comparison of the linearized and the actual model of the open-loop readout electronics. As it can be seen, the linearized model works with a very high accuracy.

### 3.3. Controller Considerations

There are three basic types of controllers which can be used with the proposed system: Proportional (P), proportional-integral (PI), and proportional-integral-derivative (PID). Among these types, a P-controller would not be sufficient for in that case the linearity response of the loop would degrade because of the steady-state error, and increasing the controller gain further for reduction in the non-linearity would cause stability issues. Including a D-controller into the system would be unnecessary for it would bring extra complications in the linearity response, and the operation band of

the system is not aimed to be improved significantly by controller since it mainly is set by the low-pass filter at the final stage of the open-loop readout electronics.

A PI-controller is chosen to be used with the proposed system because using such a controller, steady-state error can be zeroed (theoretically) thanks to its high DC gain. Thus a highly linear response can be obtained from the closed-loop system without degrading the loop stability. In the following sub-sections, the design methodology for the controller to be used in the system is discussed along with stability considerations.

### 3.3.1. Controller Design Approach

There are several methods for designing a PI-controller such as using Ziegler-Nichols tuning tables [31], [32], or by using time-domain equations to tune the system at desired overshoot and settling time values for the desired phase margin. Using tables to tune the response of the proposed system can get pretty restrictive for such tables are usually created for very generic systems and applications. Moreover, such tuning methods are usually based on the system's time-domain responses. Since the linear s-domain model of the proposed system is readily at hand, neither the use of tables nor the complicated mathematical equations representing the system's response in time domain is necessary.

The open-loop readout electronics, *the plant*, basically has two dominant poles placed around 100 Hz by the low-pass filter. These poles causes the phase of the plant to drop to  $-180^\circ$  after about 10 Hz. The phase is further reduced by the poles mainly created by the mechanical transfer function of the sensor. Additionally, the PI-controller consists of a zero and introduces a  $-90^\circ$  phase shift beginning from very low frequencies (DC), and it will increase the gain of the open-loop transfer function at the frequencies lower than its zero location. Considering these phase and gain issues, placing the PI-controller's zero at a frequency above the dominant pole of the system will cause serious stability problems. On the other hand, placing the zero at lower frequencies than the dominant pole's location will cause degradation in the bandwidth of the closed-loop system. In either case, the settling time of the system will degrade. In Figure 3.9, sample step responses of a closed-loop system with a second-order plant

(100 Hz corner frequency) and an I-controller is demonstrated in three cases: The zero of the controller is placed at 40 Hz; 100 Hz; and 250 Hz. Note that the P gains are unity for all of the three cases.

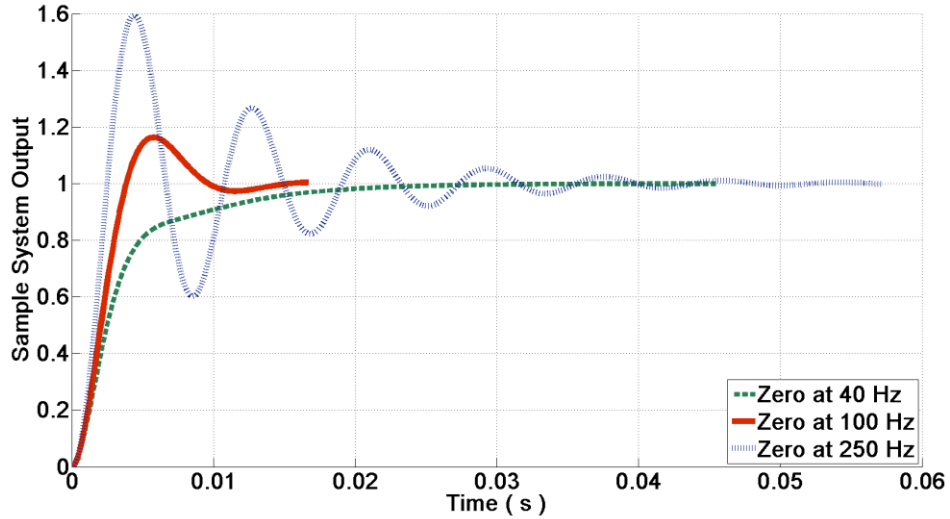


Figure 3.9: Comparison of a sample system's closed-loop step response for three different I-controller zero locations. Placing the controller zero further away from the plant's pole (at 100 Hz) on either side causes the settling time to degrade. Additionally, as the zero frequency increases, the stability of the system degrades. Note that for better comparison of settling times, each of the responses are clipped once they are settled in an equal error band.

Taking the considerations above, the zero of the PI-controller is decided to be placed at the frequency where the plant's phase response drops to  $-45^\circ$ . This way, the phase drop by one of the poles of the low-pass filter will be compensated, making it easier to satisfy the stability criterion. Moreover, the bandwidth of the system will not be degraded. In the following equations, the effect of this first decision is demonstrated.

A PI-controller has the following generic transfer function:

$$PI(s) = K_P + \frac{K_I}{s} = \frac{sK_P + K_I}{s} \quad (3.10)$$

where,  $K_P$  is the proportional gain and  $K_I$  is the integral gain of the controller.

Given that the frequency at which plant's phase response drops to  $-45^\circ$  is  $\omega_{-45^\circ}$ , then the following relation for the controller's zero location should be satisfied:

$$\frac{K_I}{K_P} = \omega_{-45^\circ} \quad (3.11)$$

The first step of design approach is followed by a tuning on either of the gain values while keeping their ratio constant as in Equation 3.11. Basically, both gain values are increased equally until a point where an acceptable amount of overshoot ( $\sim 20\%$ ) and phase margin ( $\sim 45^\circ$ ) is achieved.

### 3.3.2. Controller Design and Stability Analysis

The stability analysis and the parametric design of the controller is based on the linear model created for the open-loop readout electronics. In Figure 3.10, the complete model for the closed-loop system is demonstrated. Note that there are two additional blocks to the open-loop model, which are the *Voltage-to-g* and the *PI-Controller* blocks. The *PI-Controller* block is a transfer function simulating the controller. Whereas the *Voltage-to-g* block is simply a gain block completing the relation between the closed-loop output voltage,  $V_{FB}$ , and the acceleration input. This derivation and the resulting equation of this relation given in Chapter 2, Section 2.3.2, Equation 2.52. The only difference is the conversion of input unit to 'g' instead of 'a' by a factor of 9.81. Also note that, the error signal is directly generated based system input,  $g$ , instead of the force,  $F$ . By doing so, observation of the system response is much easier since the scaling factor between the model output and the input is simply unity.

The open-loop transfer function of the system as used in the stability analysis is the multiplication of all the blocks:

$$H_{OL}(s) = K_g * K_m * K_s * K_{pa} * K_{dm} * K_f * A(s) * L(s) * C(s) \quad (3.12)$$

The terms excluding the controller,  $C(s)$ , is considered as the plant, and noted with the symbol  $H_P(s)$  where,

$$H_{OL}(s) = H_P(s) * C(s) \quad (3.13)$$

Thus the transfer function of the closed-loop system, according to the model in Figure 3.10, is:

$$H_{CL}(s) = \frac{C(s)*H_P(s)}{1+C(s)*H_P(s)} \quad (3.14)$$

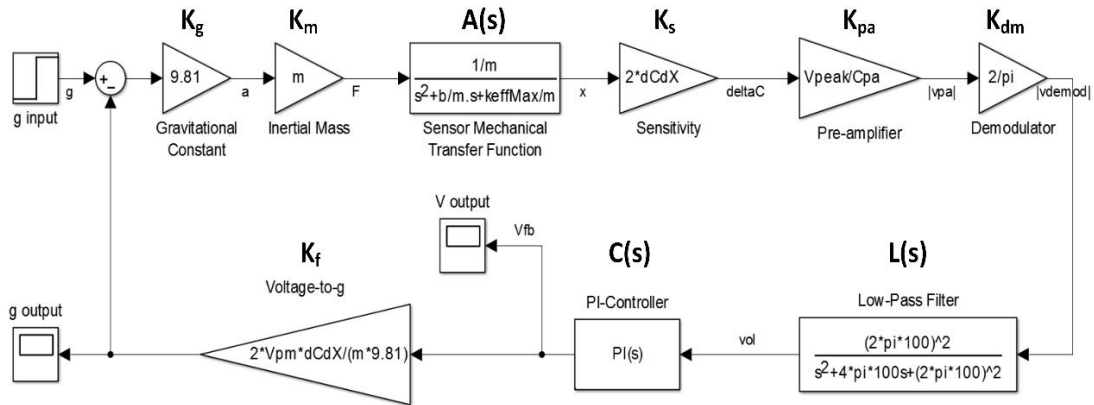


Figure 3.10: The linear closed-loop system model created in MATLAB Simulink environment. Note that even though the actual output of the circuit is ' $V_{FB}$ ', using the ' $g$  output' node as the output of the system eases the analysis of the system significantly.

One important aspect of the linear model that needs to be paid extra attention to is the effective spring constant parameter,  $k_{eff}$ . This term has a direct contribution in the DC gain of the mechanical transfer function, and it is affected by both the proof mass voltage and the feedback voltage (Chapter 2, Section 2.3.3, Equation 2.62). As the magnitude of the applied acceleration increases, the feedback voltage value increases;  $k_{eff}$  decreases; DC gain of the open-loop transfer function increases; thus the phase margin decreases. Because of these chain of events, while setting the parameters for the controller, *the worst case scenario*, in which the feedback voltage is equal to the proof mass voltage, should also be taken into account. For this purpose, while designing the controller for the proposed system, the model is simulated for three different values of feedback voltage: 0 V, 3.9 V (results in an average  $k_{eff}$ ), and 5.5 V (maximum allowed feedback voltage, which actually is the proof mass voltage).

In Figure 3.11, the bode plots of the plant, the controller, and the complete open-loop transfer function for all three cases are demonstrated. Note that the zero location of the controller is set such that the phase responses of both blocks intersect at  $-45^\circ$  as explained in the previous sub-section, and the gain of the controller is yet to be tuned. Additionally in Figure 3.12, the step response of the closed-loop system for the unity gain controller is presented.

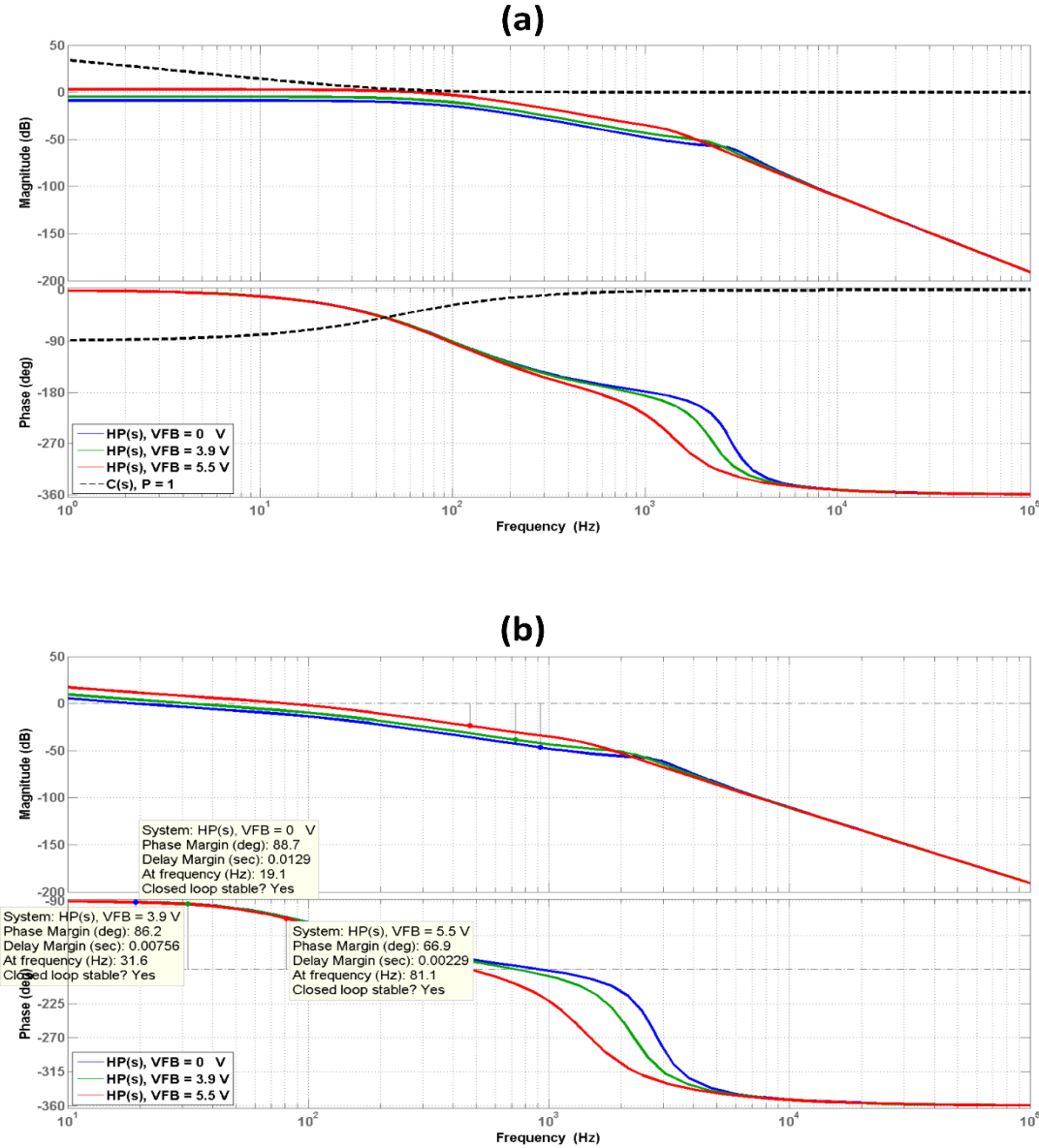


Figure 3.11: (a) Bode plots of the plant and the controller for three different cases of  $V_{FB}$  voltages. (b) Bode plots of the open-loop transfer function  $H_{OL}(s)$  and the stability margins for all three cases. Note that the gain of the controller is to be tuned yet.

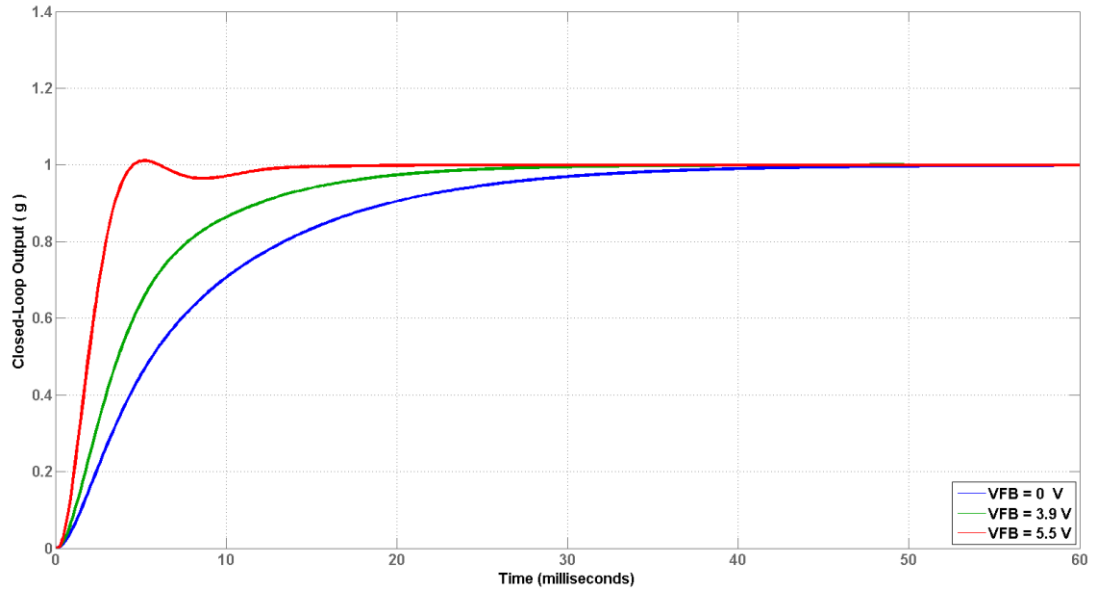


Figure 3.12: The step responses of the closed-loop system for three different cases of  $V_{FB}$  voltage with a unity-gain PI-controller.

As it can be seen in Figure 3.11-(b), the phase margins of the of the system is above  $45^\circ$  degrees for all three cases. By observing these margins and the step responses in Figure 3.12, it can be said that the system is currently over-damped causing a significant reduction in the closed-loop system bandwidth. So as the step-2 of the controller design approach, the P gain of the controller is increased until an acceptable amount of phase margin and overshoot is obtained from the system. After these two steps of design, the controller gain values and the zero location are decided as shown in Table 3.4.

Table 3.4: The controller parameters set after the two tuning steps applied on the system.

Controller Parameter	P	I	$f_z$ (Hz)
Value	6	1928	51

The stability margins of the system after the tuning step are demonstrated in Figure 3.13, and in Figure 3.14, the bode plots of the closed-loop system is presented demonstrating the bandwidth of the system.

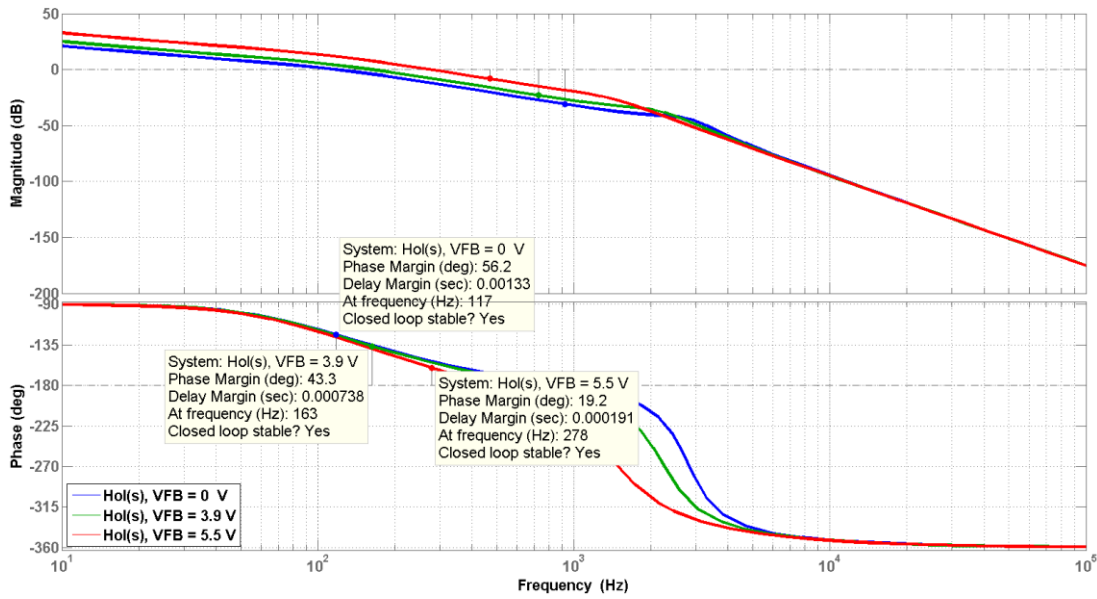


Figure 3.13: The bode plots of the open-loop system after the tuning of the PI-controller is completed. Note that the case where  $V_{FB}=5.5$  V is the worst case scenario for the stability of the system.

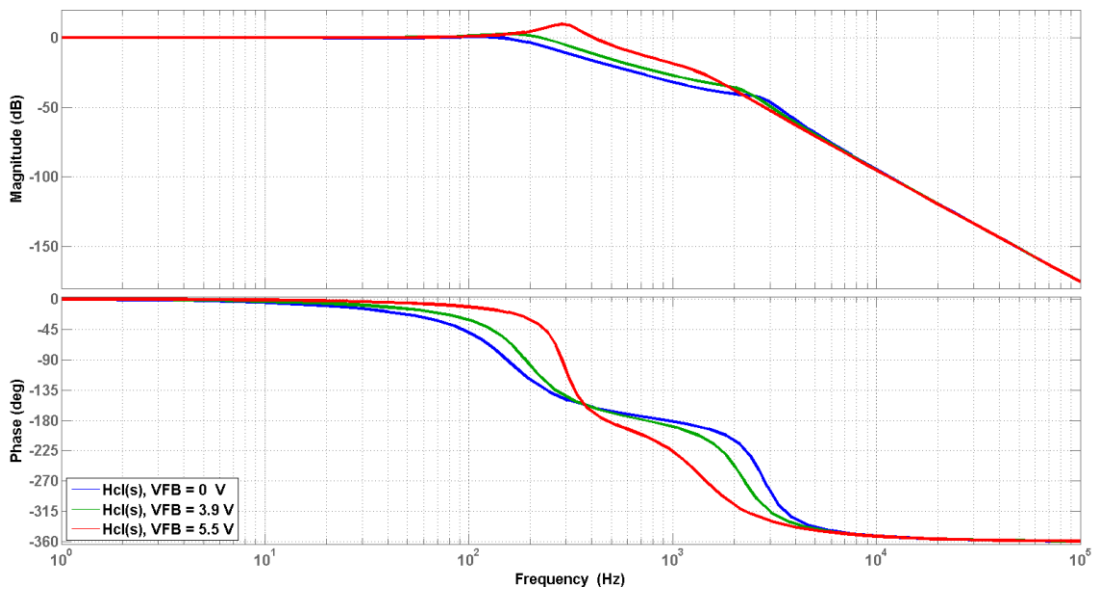


Figure 3.14: The demonstration of the closed-loop response of the system with the given controller parameters. It can be seen in the figure that the bandwidth of the system for all three cases is roughly above 100 Hz.

As demonstrated in Figure 3.13, the stability of the system is achieved in all three cases. Note that the phase margin of  $\sim 20^\circ$  for the worst case scenario is not usually an acceptable value for generic control systems. However, since that case is an extreme scenario and sustaining a  $45^\circ$  phase margin in that scenario would cause a significant loss in the bandwidth for the other cases, this configuration of the controller is decided to be acceptable. Note that the a  $45^\circ$  phase margin can be achieved in that scenario by reducing the P gain is desired.

In Figure 3.15, the step responses of the system is demonstrated. It must be noted that in the actual system, the *percent overshoot* value increases *gradually* as the feedback voltage increases eventually getting close to 60 % as shown in Figure 3.15. However, the *peak value* of the system response will not be as high as shown in the figure because of this gradual increase in the percent overshoot. So it can be said that the two responses in the figure, where the feedback voltage is 3.9 and 5.5 volts, are exaggerated. This claim can be verified by observing the step response obtained from the non-linear system model in Section 3.4.2, Figure 3.25.

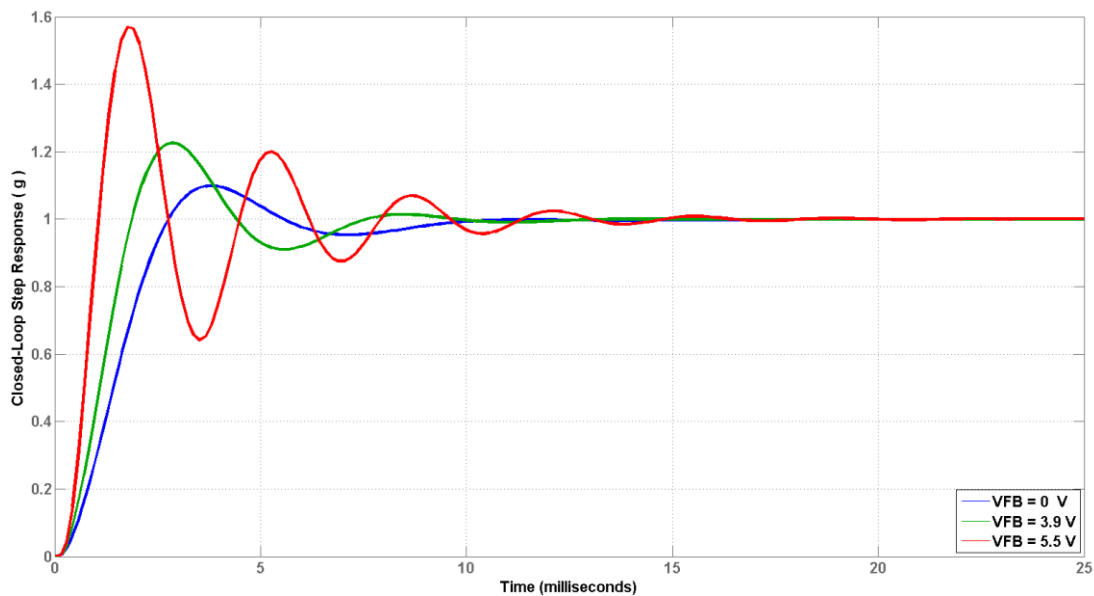


Figure 3.15: The step responses of the closed-loop system for all three different scenarios. Note that in the actual system, the peak values of the responses would not be as high as shown in this figure.

### 3.4. System Level Transient Simulations

After the design and the modelling of all the building blocks, and the controller design along with the stability analysis based on the linearized accelerometer model is complete, the transient simulations of the complete closed-loop accelerometer is run. These simulations are based on the non-linear model of the system for it offers a higher accuracy than the linearized system.

Prior to testing the implemented system in closed-loop, open-loop tests are conducted in order to verify that everything in the open-loop readout electronics works as expected. For this reason, even though the final system is a closed-loop accelerometer, open-loop simulations are also run and presented in the following sub-section followed by the closed-loop simulations in the next sub-section.

#### 3.4.1. Open-Loop Accelerometer

In Figure 3.16, the Simulink model used in the simulations in this sub-section is given.

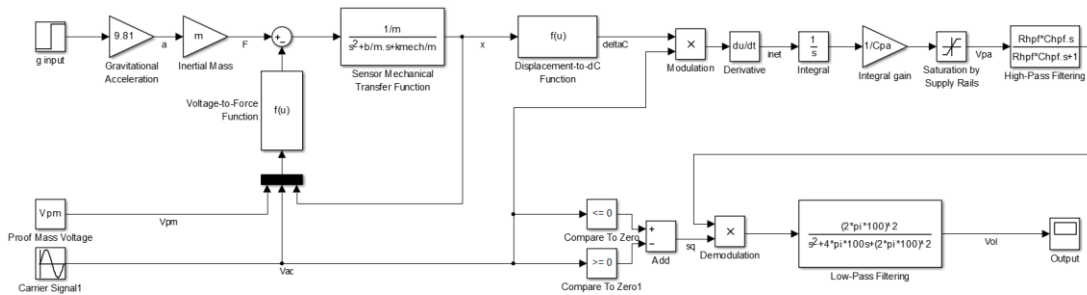


Figure 3.16: The non-linear model of the accelerometer which is used for the system-level simulations in open-loop configuration.

In Figure 3.17, unit step response of the accelerometer in open-loop configuration is shown. The estimated scale factor of the accelerometer can be found out using this simulation result. Note that due to the non-linearity, this scale factor is only acceptable for small acceleration inputs.

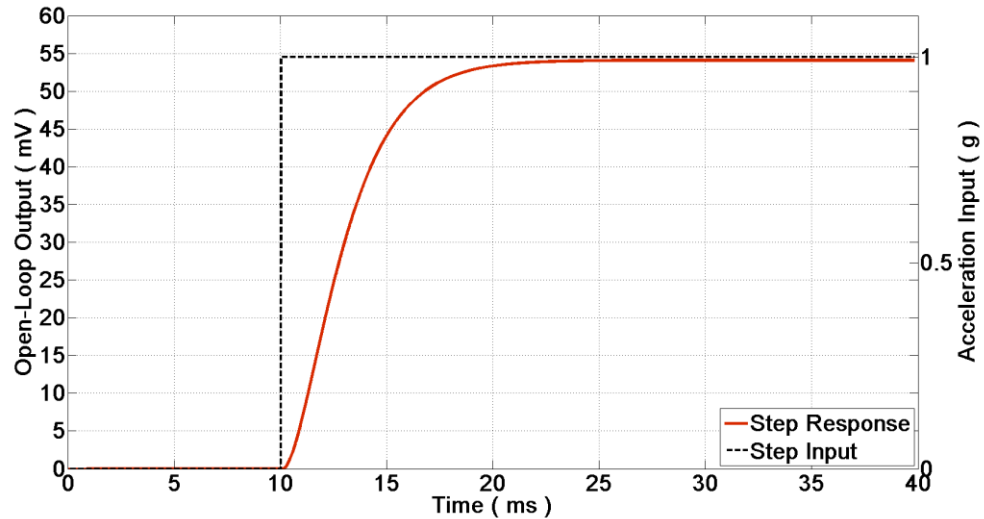


Figure 3.17: The step response of the accelerometer in open-loop configuration. The settled voltage output of the open-loop readout electronics shows the scale factor of the accelerometer is about 54 mV/g in open-loop configuration.

The factor that is limiting the range of the accelerometer in open-loop configuration is the maximum displacement before the proof mass enters pull-in state. Note that this maximum displacement value is approximately equal to the gap separation divided by three as a generally accepted fact, considering the proof mass is pulled in one direction by one of the electrodes. Even though this is not the same configuration as the proposed accelerometer's voltage feedback structure, a similar effect is present. In Figure 3.18, the pull-in case occurring in response to a ramp input is demonstrated. The magnitude of the acceleration input, high enough to displace the proof mass sufficiently for a pull-in situation, sets the operation range of the accelerometer. In this case, it is about 15 g. Figure 3.19 includes a demonstration of the open-loop accelerometer response in  $\pm 15$  g input range. The estimated linearity performance of the accelerometer is obtained from the data present in this figure.

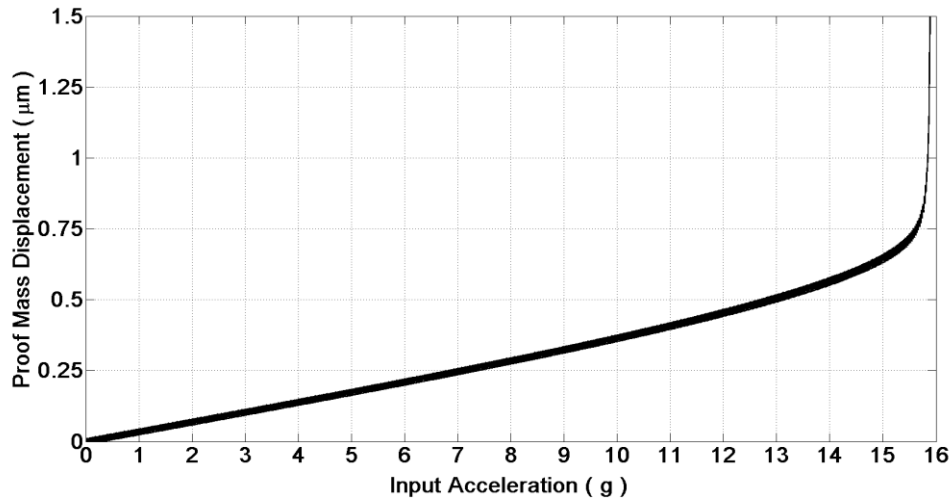


Figure 3.18: The demonstration of the pull-in occurring due to excessive amount of proof mass displacement into one direction in response to a ramp input. Note that if the proof mass voltage was not applied to the electrodes, the range would be higher at the cost of less readout gain thus the scale factor.

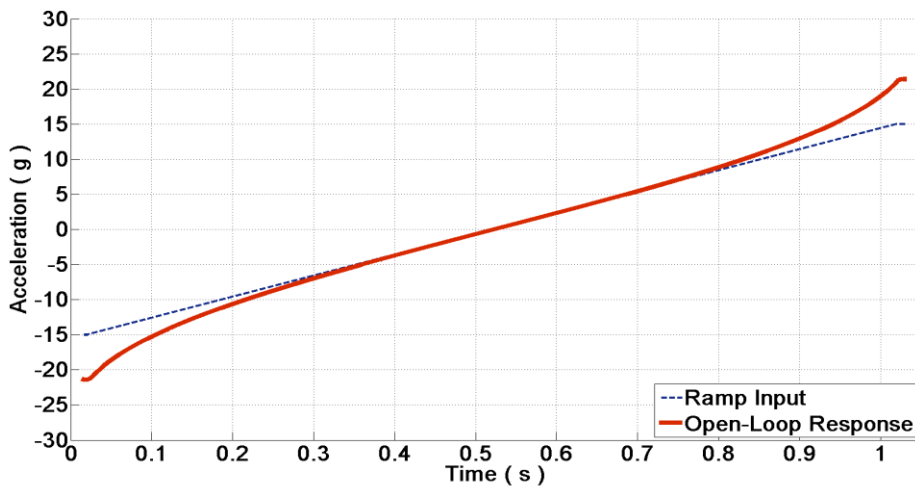


Figure 3.19: The ramp response of the accelerometer between -15 and +15 g. Notice the non-linearity due to the non-linear nature of the varying-gap electrode type structure of the sensing element.

Additionally, in Figure 3.20, the chirp response of the accelerometer is presented as a demonstration of the bandwidth of the accelerometer in open-loop configuration. Also in Table 3.5, the performance summary of the open-loop accelerometer is given.

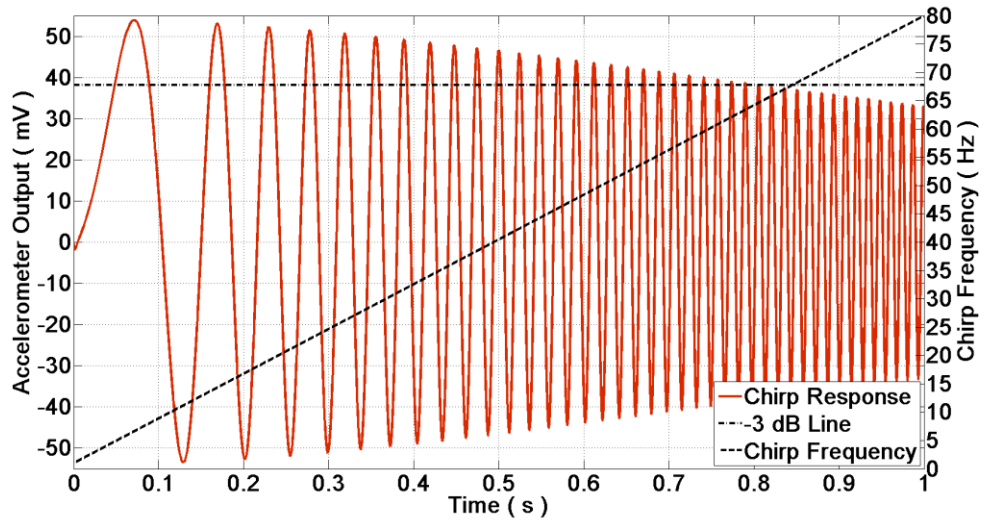


Figure 3.20: Simulated chirp response of the accelerometer in open-loop configuration. -3 dB frequency of the accelerometer in open-loop configuration can be observed to be around 65 Hz by this simulation result.

Table 3.5: Simulated performance summary of the accelerometer in open-loop configuration.

Property	Scale Factor	Full-Scale Range	Maximum Non-linearity	Bandwidth (-3dB Point)
Value	54 mV/g	$\pm 15$ g	21 %	65 Hz

### 3.4.2. Closed-Loop Accelerometer

Figure 3.21 demonstrates the Simulink model of the closed-loop accelerometer which is used to obtain the simulation results as presented in this sub-section.

In Figures 3.22-24, the unit step response; the ramp response in full-scale range; and the chirp response of the closed-loop accelerometer's non-linear model are presented respectively. Figure 3.22 additionally includes the plot demonstrating the change in the proof mass displacement during the application of a unit step input demonstrating the effect of force balancing. Finally Table 3.6 summarizes the performance expectations of the proposed system based on the simulation results.

Note that earlier in Section 3.3.2, it was claimed that the percent overshoot values are exaggerated by the linearized system models, and they would not be as high for high acceleration inputs unlike the linear model suggests. In Figure 3.25, a plot demonstrating the closed-loop accelerometer’s response to a high acceleration step input is presented as a demonstration. By this figure, it can be verified that the percent overshoot value is below 20 % unlike it is shown in Figure 3.15 for a case where the feedback voltage is around 3.9 V.

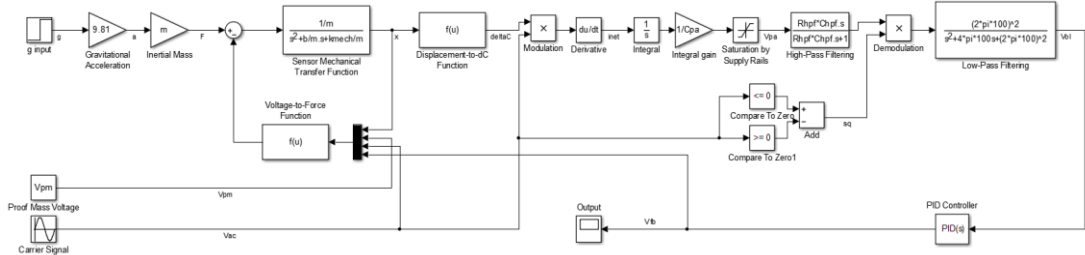


Figure 3.21: The non-linear model of the accelerometer which is used for the system-level simulations in closed-loop configuration.

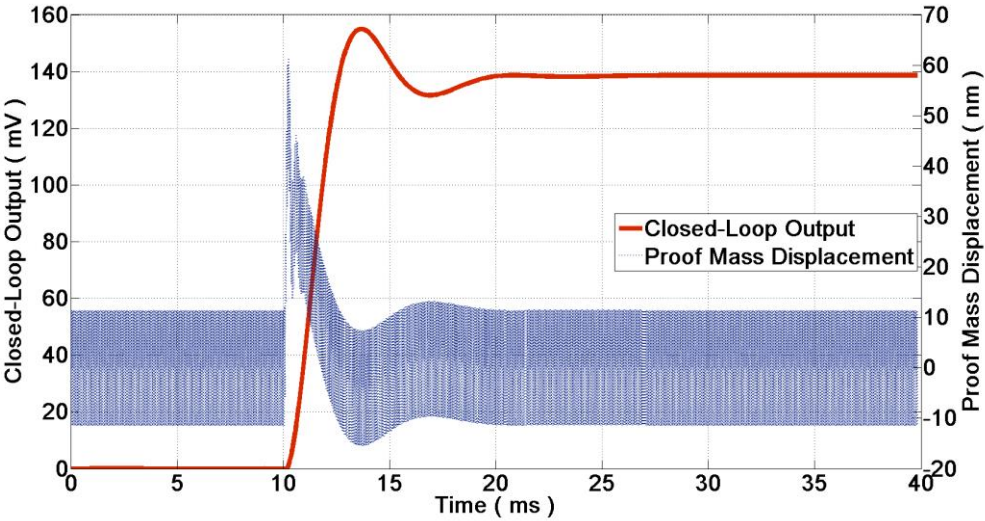


Figure 3.22: The simulated unit step response of the proposed closed loop accelerometer demonstrated along with the change in the proof mass displacement while the force balancing action takes place.

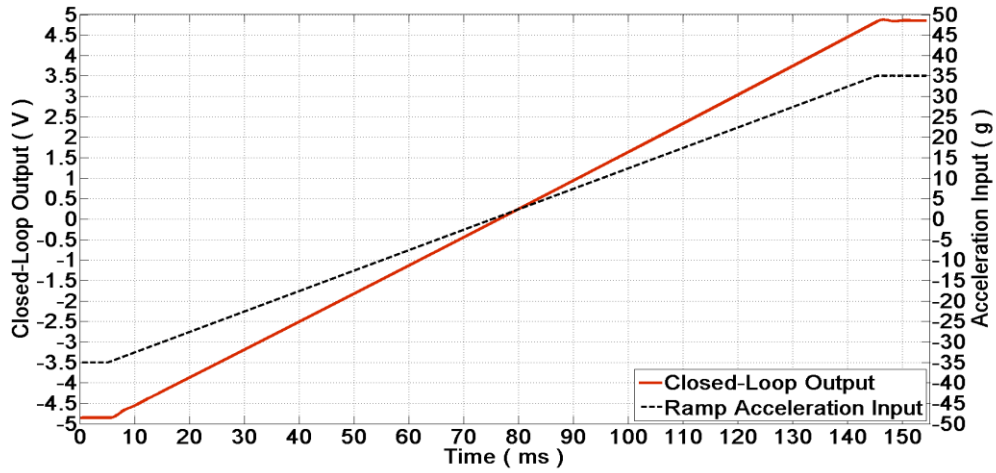


Figure 3.23: The ramp response of the proposed closed loop accelerometer in -35 to +35 g range.

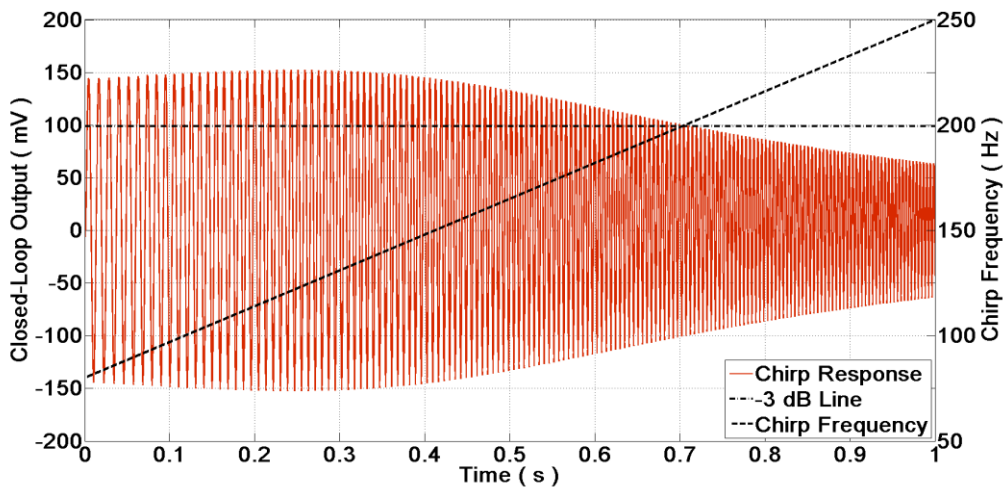
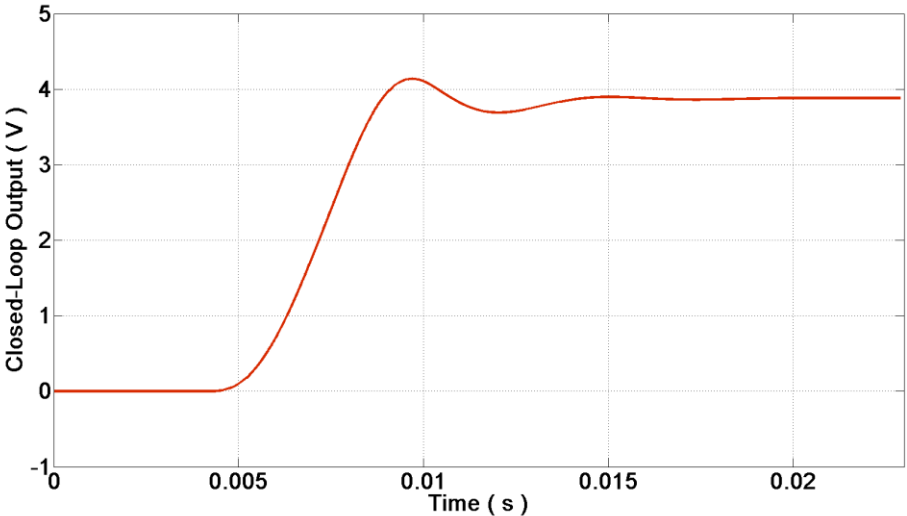


Figure 3.24: The chirp response of the proposed closed loop accelerometer demonstrating the operation bandwidth.

Table 3.6: Simulated performance summary of the proposed closed-loop accelerometer.

Property	Scale Factor	Full-Scale Range	Maximum Non-linearity	Bandwidth (-3dB Point)
Value	140 mV/g	$\pm 39$ g	0.0 %*	200 Hz

(\*): Note that the non-linearity of the closed-loop accelerometer model is 0 % as expected. Even though the system is modelled including all non-linear contributions to the loop, the model is still an ideal one excluding all imperfections that can occur both in circuit and the sensing element. Sensitivity mismatch between the two electrode capacitances, for example, is a non-linearity source that is not included in the model. The effect of sensitivity mismatch on system non-linearity is investigated in Chapter 6, Section 6.2.



*Figure 3.25: The response of the closed-loop accelerometer to a high-g step input. It can be observed by this figure that, the percent overshoot is not as high as suggested by the linear model as expected.*

**3.5. Summary and Conclusions**

In this chapter, the models created to simulate the proposed system are presented. The approach to design a linear model based on the non-linear model is introduced. By having both linear and non-linear high-accuracy models, the system could be simulated both in time and frequency domains prior to circuit implementation. Additionally, the methodology behind designing a system-specific PI-controller is introduced and discussed in detail with clear reasoning. By the end of the chapter, the accuracy of the PI-controller design method and the linearized model (compared to the non-linear

model) is justified with the system-level simulations run on the non-linear model of the proposed accelerometer.

Additionally, the superiority of a closed-loop accelerometer compared to an open-loop one is demonstrated with the transient simulation results: Only by closing the loop using a PI-controller; scale factor, bandwidth, linearity, and range performances of the accelerometer are shown to be improved.

In the next chapter, the steps taken to implement the proposed system in circuit-level are introduced.



## CHAPTER 4

### CIRCUIT-LEVEL DESIGN AND MODELLING

The linear and non-linear models of the proposed system are demonstrated and discussed in the previous chapter. In this chapter, the design procedure of the modelled system in circuit-level is presented, and the components that are picked to be used in the implementation of the system are also introduced respectively. Additionally, a behavioral model of the complete closed-loop system, which is implemented in SPICE simulation environment, is shown. The chapter begins with Section 4.1 in which the electrical circuit of the open-loop readout electronics presented. In Section 4.2, the PI-controller circuit and the topology used to generate the required waveforms to be fed to the electrodes are shown. In Section 4.3, the electrical model of the proposed system is demonstrated. Also, a behavioral model of the sensing element, which is yet again created in SPICE environment, is introduced. Section 4.4 gives detailed information on how the noise of the complete system is estimated, and in Section 4.5 the performance expectation based on calculations prior to implementation is summarized. The chapter ends with Section 4.6 with a brief summary and conclusions related with the circuit-level design.

#### **4.1. Design of the Electrical Blocks**

All of the circuitry realizing the proposed accelerometer is implemented using off-the-shelf discrete components. The component choice and the critical considerations about each building block are presented in the following sub-sections.

### 4.1.1. Front-End Electronics

In the implementation of the front-end electronics, the dual operational amplifier (OpAmp) AD8606ACBZ [33] by Analog Devices Incorporated (ADI) is used for its superior precision and noise performance. One of the OpAmps is used for pre-amplification, and the other is used as a voltage buffer. In Figure 4.1, the circuit schematic of the front-end electronics is given.

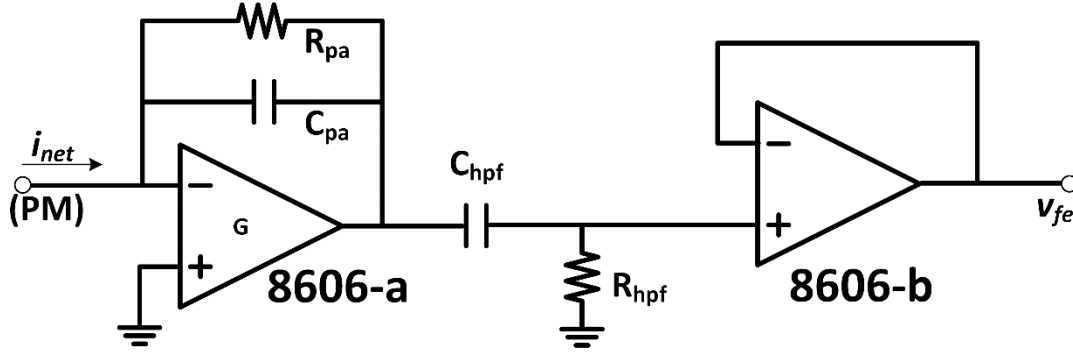


Figure 4.1: The circuit schematic of the front-end readout electronics composed of a pre-amplifier, a passive high-pass filter and a voltage buffer.

As it was discussed earlier in Chapter 2-Section 2.2.1, a capacitive transimpedance amplifier (TIA) is used as a pre-amplifier in the proposed system. However, in the implementation of the system, a feedback resistor,  $R_{pa}$ , is used in addition to the feedback capacitor,  $C_{pa}$ , which sets the capacitive gain of the amplifier. The reason for using the feedback resistor is because otherwise the inverting input of the OpAmp forms a high-impedance node (DC) in between the sensor electrode capacitances, the input of the OpAmp and the feedback capacitor. In this case the bias currents of the amplifier would cause the output to saturate.

The s-domain transfer function of the pre-amplifier in this case is:

$$G(s) = \frac{V_{pa}}{i_{in}} = -Z_{pa} = -\frac{R_{pa}}{1+s*C_{pa}*R_{pa}} \quad (4.1)$$

The same transfer function in jw notation is as follows:

$$G(jw) = -\frac{R_{pa}}{1+j*w*C_{pa}*R_{pa}} \quad (4.2)$$

If the angular frequency of the carrier signal,  $w_{ac}$ , and the values of the feedback passives are arranged such that

$$C_{pa}R_{pa}w_{ac} \gg 1 \quad (4.3)$$

then the magnitude response of the pre-amplifier at the vicinity of the carrier signal frequency can be approximated as

$$|G(jw)|_{w_{ac}} \cong -\frac{R_{pa}}{w_{ac} * C_{pa} * R_{pa}} \quad (4.4)$$

So it can be said that the transimpedance transfer function around the frequency of interest,  $w_{ac}$ , is

$$G(s) \cong -\frac{1}{sC_{pa}} \quad (4.5)$$

and capacitive amplification can be achieved even in the presence of a feedback resistor.

As for the high-pass filter, the transfer function in  $jw$  notation simply is:

$$H(jw) = \frac{jwR_{hpf}C_{hpf}}{1+jwR_{hpf}C_{hpf}} \quad (4.6)$$

Again, at the vicinity of the carrier frequency, if

$$C_{hpf}R_{hpf}w_{ac} \gg 1 \quad (4.7)$$

then,

$$|H(jw)|_{w_{ac}} \cong 1 \quad (4.8)$$

Meaning the pre-amplified readout voltage can be transferred through the high-pass filter without significant loss.

After the high-pass filtering stage, a voltage buffer is used in order to prevent any off-set voltages that might occur due to the current drawn by the demodulator following the front-end electronics stage.

According to the discussions above and taking the phase contributions into account, the passive component values of the front-end electronics are chosen as shown in

Table 4.1. Note that the component availability is another criteria in decision of these components.

Table 4.1: The passive components used in the implementation of the front-end electronics.

Component	$C_{pa}$	$R_{pa}$	$C_{hpf}$	$R_{hpf}$
Value	3.9 pF	10 M $\Omega$	10 nF	36.5 k $\Omega$

#### 4.1.2. Demodulator and Low-Pass Filter

The switching demodulator used in the implemented circuit is AD630 [34] by ADI. The die-level (unpackaged) version of this chip is used for it employs a very little surface area on the circuit board.

The low-pass filter and its passive component values are designed using the software FilterPro Desktop for the design of a single active element second order filter is a very straight-forward work considering there are several fundamental topologies to pick from. A Butterworth type filter in multiple-feedback configuration is used because the magnitude response of this topology is closer to the MATLAB model created prior to circuit design. The DC gain of the filter is set to be unity (0 dB) as in the model as well. In Figure 4.2, the implemented low pass filter topology is demonstrated.

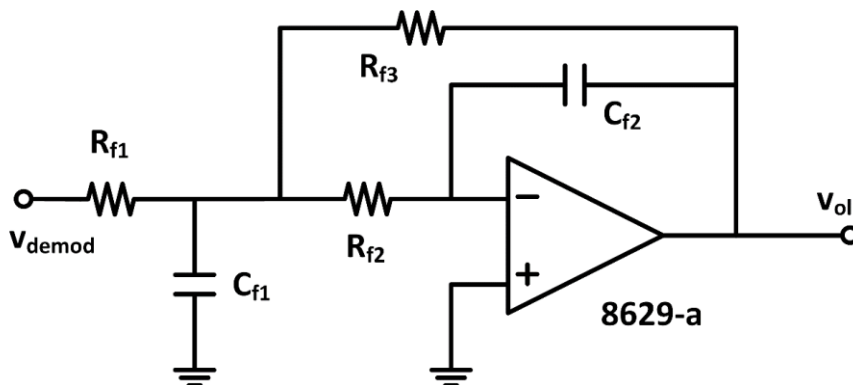


Figure 4.2: The multiple-feedback type, second-order Butterworth low-pass filter as used in the implementation of the proposed accelerometer.

AD8629ARMZ [35] by ADI is selected to be used with this filter. The reason for using this component is its superior drift performance. The drift performance is important during and after the low-pass filtering stage because the acceleration information is down-converted to the low-frequency band unlike it is during pre-amplification. Note that the AD8629 is a dual OpAmp, and the other amplifier inside is used to implement the PI-controller. In Table 4.2, the list of passive components used to implement the low-pass filter is given.

Table 4.2: The passive components used in the implementation of the low-pass filter.

Component	$R_{f1}$	$R_{f2}$	$R_{f3}$	$C_{f1}$	$C_{f2}$
Value	11.3 k $\Omega$	5.62 k $\Omega$	11.3 k $\Omega$	330 nF	100 nF

#### 4.1.3. PI-Controller

The second OpAmp inside the dual package used for the implementation of the low-pass filter is used to form the PI-controller of the circuit. The topology of the PI-controller used in the circuit is given in Figure 4.3. Note that details about single element PID-controllers can be found in [36].

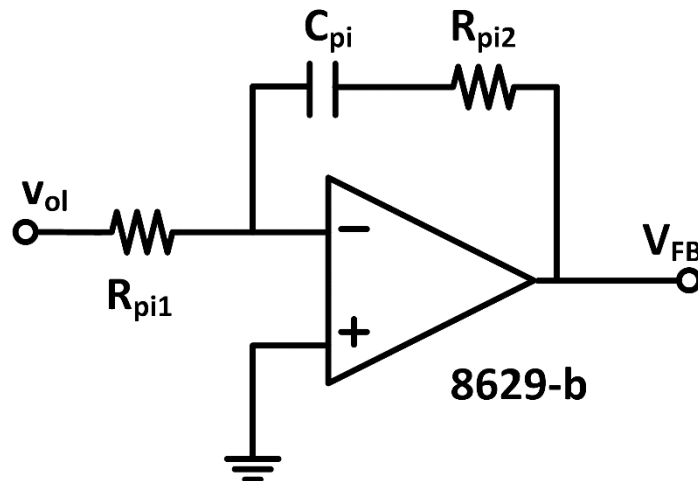


Figure 4.3: The topology of the PI-controller used in the implementation of the proposed circuit.

The transfer function of this circuit block can be written as follows:

$$C(s) = \frac{V_{FB}}{V_{OL}} = -\frac{1+sR_{pi,2}C_{pi}}{sR_{pi,1}C_{pi}} = -\left(\frac{R_{pi,2}}{R_{pi,1}} + \frac{1}{s}\right) \quad (4.9)$$

Considering that a PI-controller transfer function has the following generic form:

$$C(s) = P + \frac{I}{s} \quad (4.10)$$

Then the  $P$  and the  $I$  gains of the controller can be expressed with the passive component values as follows:

$$P = \frac{R_{pi,2}}{R_{pi,1}} \quad (4.11)$$

$$I = \frac{1}{R_{pi,1}C_{pi}} \quad (4.12)$$

According to the derivation above, and the controller parameter design steps in Chapter 3-Section 3.3.2, the values of the passive components to be used with the controller circuit are set as demonstrated in Table 4.3.

*Table 4.3: The passive components used in the implementation of the PI-controller.*

Component	$R_{pi,1}$	$R_{pi,2}$	$C_{pi}$
Value	52.3 k $\Omega$	309 k $\Omega$	10 nF

#### 4.1.4. Voltage Feedback Topology

The waveforms of the signals that are applied on the differential electrodes,  $E_p$  and  $E_n$ , of the sensing element are discussed earlier in Chapter 2-Section 2.4.1. These waveforms have the following form.

$$V_{E,p} = V_{PM} + v_{ac} + V_{FB} \quad (4.13)$$

$$V_{E,n} = V_{PM} - v_{ac} - V_{FB} \quad (4.14)$$

Considering the gain polarities of each building block, using the electrode waveforms as demonstrated above in Equations 4.13-14 causes a positive feedback case. In order

to correct the complete loop polarity, the waveforms are modified as shown in Equations 4.15-16 below. Note that such modification has no effect on the circuit operation at all but correct the loop's polarity.

$$V_{E,p} = V_{PM} - v_{ac} + V_{FB} \quad (4.15)$$

$$V_{E,n} = V_{PM} + v_{ac} - V_{FB} \quad (4.16)$$

In order to generate these waveforms, which are crucial for simultaneous real-time sensing and force-feedback, a high-precision dual instrumentation amplifier AD8222BCPZ [37] by ADI is used. This instrumentation amplifier has a reference input, *REF*, which off-sets the amplifier output by the amount of voltage applied on this terminal. This terminal is used to off-set each electrode voltage by  $V_{PM}$ . In Figure 4.4, the topology used to generate the required waveforms using 8222 is demonstrated.

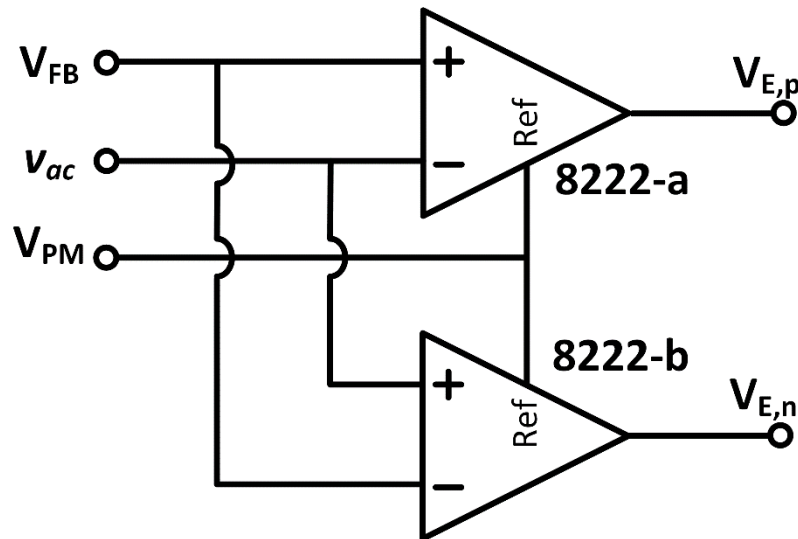


*Figure 4.4: The topology, constructed using two instrumentation amplifiers, which generates the electrode waveforms in order to achieve simultaneous sensing and feedback using a single set of differential electrodes.*

It must be noted that, waveforms  $V_{E,p}$  and  $V_{E,n}$  can be applied to either electrode interchangeably. The polarity of the complete loop will be preserved as long as the sign consistency between the carrier signal,  $v_{ac}$ , and the feedback voltage,  $V_{FB}$ , on the associated electrode waveform is maintained.

#### 4.1.5. Voltage Regulation

The operational amplifier used in the circuit allows a maximum of 5 V between the positive and the negative supply terminals. On the other hand, the output of the instrumentation amplifier should be able to output voltages up to 13.5 V considering the proof mass voltage, peak value of the carrier signal, and the maximum feedback voltage is added on top of each other by the instrumentation amplifier. For this reason, two different rail voltages are used within the circuit:  $\pm 15$  V and  $\pm 2.5$  V. The 15 V rail, as noted as *HVDD* and *HVSS*, are directly taken from a power supply. Whereas the 2.5 V rail, as noted as *VDD* and *VSS*, is generated through a dual supply voltage regulator LT3032 by Linear Technology Corporation. This low dropout regulator comes within an extremely compact DFN-14 package, and with its high noise performance it is a highly suitable chip to be used in the implementation of the proposed accelerometer.

The proof mass voltage is initially generated using a band-gap reference integrated circuit (IC), ADR4520 by ADI. However, later it is decided that the  $\sim 2$  V reference voltage at the output of this IC is too low for the accelerometer, and it incorporated a very large surface area on the circuit board. For these reasons, the 5.5 V proof mass voltage is directly fed to the circuit through the power supply, accompanied by decoupling capacitors. In Figure 4.5, the circuit diagram demonstrating the generation of all of the supply voltages is given. Note that this figure includes the passive component values as well. In this figure, all of the capacitances are in  $\mu\text{F}$ ; all of the resistances are in  $\text{k}\Omega$  units.

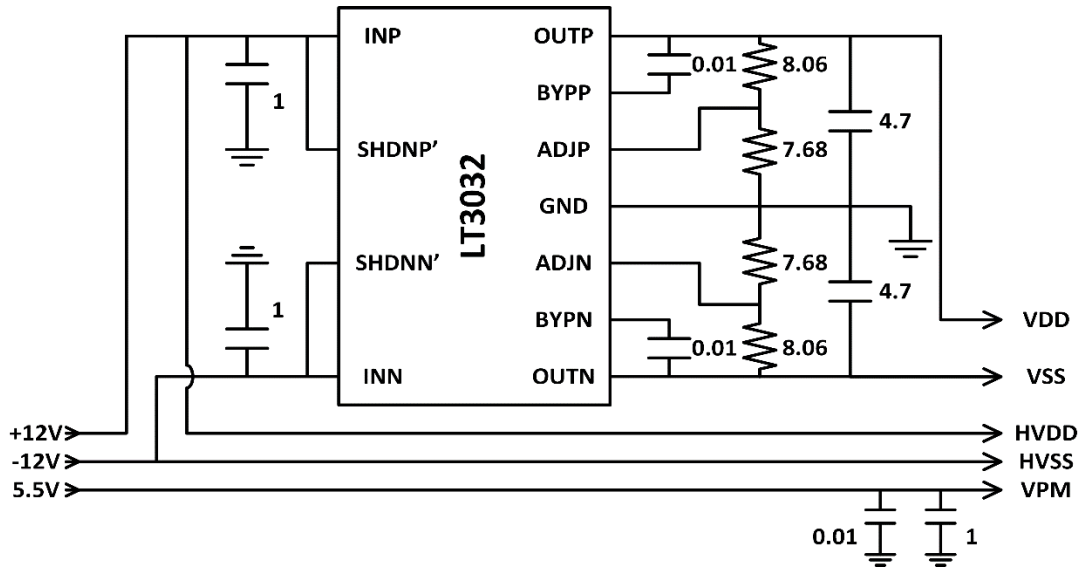


Figure 4.5: The supply network which is used to feed the proposed circuit. All of the capacitances are in  $\mu\text{F}$ ; all of the resistances are in  $\text{k}\Omega$  units.

## 4.2. SPICE Model

Apart from the simulations conducted using the MATLAB Simulink, an electrical model of the circuit is necessary for a final check prior to implementation. Along various electrical simulation environments, SPICE is chosen for the circuit is to be implemented using off-the-shelf discrete components whose SPICE behavioral models are readily supplied by the manufacturer. Additionally, the flexibility of SPICE allows the user to create behavioral models, such as the sensing element's as it is introduced in Section 4.2.4. In the following sub-sections, the circuit model created using LTSpice IV freeware by Linear Technology Corporation is presented along with simulation results.

The behavioral models of all the integrated circuits to be used in the circuit are either downloaded from the manufacturer's website or requested directly from the manufacturer via e-mail in sub-circuit script format. These scripts are linked with dedicated circuit symbols manually using LTSpice to be used in the simulations. In [38], [39], generating circuit components based on sub-circuit models in SPICE is explained in detail. The accuracy of the models are later verified after the first test results.

### 4.2.1. Front-End Electronics

In Figure 4.6, frequency response of the front-end electronics is demonstrated with the simulation circuit. Note that in this simulation circuit, a dummy capacitor,  $C_{dum}$ , equal to the feedback capacitor,  $C_{pa}$ , of the pre-amplifier is used. The reason for the use of such topology is because the trend of the voltage gain and the phase response from the carrier signal (electrode voltage) to the output of the front-end electronics gives a cleaner demonstration than the transimpedance gain from the pre-amplifier input current to the output voltage.

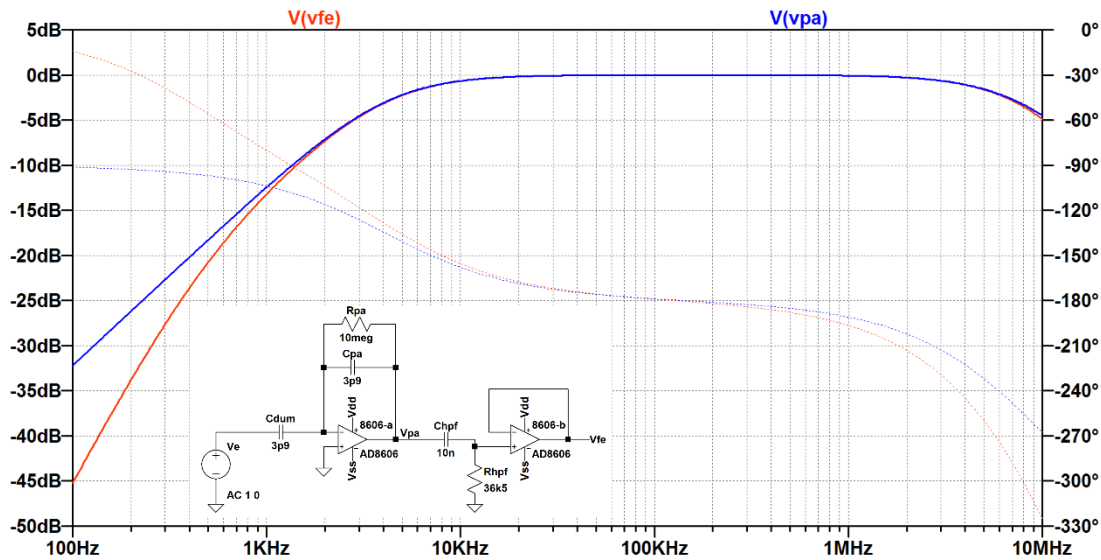


Figure 4.6: The SPICE circuit diagram of the front-end electronics and its frequency response.

As it can be seen in Figure 4.6, the amplification trend becomes capacitive after roughly 20 kHz, and it becomes perfectly capacitive at ~125 kHz with 0 dB gain and  $-180^\circ$  phase. After 1 MHz, the bandwidth of the OpAmp dominates the response. Considering this behavior, the initial frequency for the carrier signal is picked to be 125 kHz. However during the tests, it was observed that using a 20 kHz carrier signal improved the accelerometer performance, especially its noise floor. This is most probably caused by capacitive coupling within the circuit getting stronger at higher frequencies. Eventually, even though the phase and the gain behavior is not ideal at this frequency, the final tests are conducted based on a 20 kHz carrier signal.

#### 4.2.2. Demodulator and Low-Pass Filter

For the demodulation step, the actual behavioral SPICE model of the AD630 IC is downloaded as well. In Figure 4.7-a, a demonstration of this model is given. However, for an unknown reason, this model would cause the simulation time to increase incredibly, and no useful simulation data could be acquired using it. Because of this, a behavioral switching modulator is created in SPICE as shown in Figure 4.7-b and it is used throughout the simulations. Note that the dynamic behavior of the modulator is not modelled in this behavioral model. Considering this component is specifically used in RF applications, its pole locations are assumed to be beyond the dominant poles of the actual system and had no significant effect on the overall dynamic behavior of the loop.

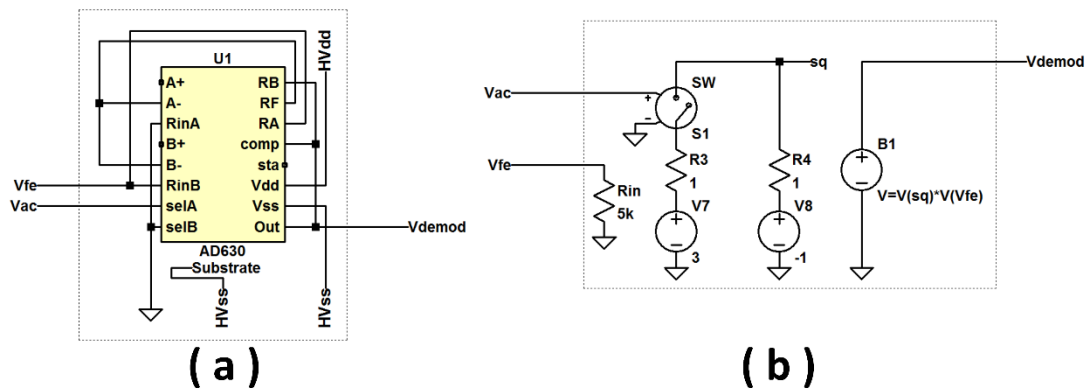


Figure 4.7: The behavioral model of the switching demodulator AD630 as supplied by the manufacturer, (a); and as created manually in SPICE, (b). ‘sq’ is a unit square wave generated based on the carrier signal,  $v_{ac}$ , and it is multiplied by the output of the front-end electronics,  $v_{fe}$ , to generate the demodulator output,  $v_{demod}$ .

Additionally in Figure 4.8, the simulation circuit and the frequency response of the low-pass filter used in the proposed system is demonstrated. As mentioned earlier, this is a very typical response and a very typical topology.

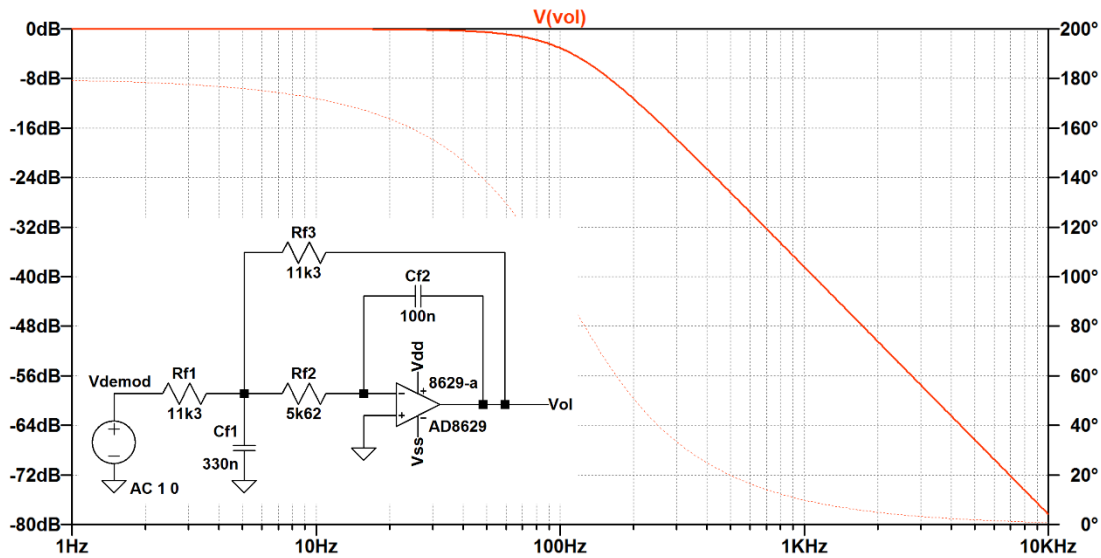


Figure 4.8: The simulation circuit and the frequency response of the low-pass filter used in the proposed system. -6 dB point of this second-order filter is slightly above 100 Hz.

### 4.2.3. PI-Controller

Unlike the ideal PI-controller which would have infinite DC gain, a practical controller has a DC gain limited by the open-loop gain of the operational amplifier it is constructed with. But either case, it can be said that the gain at very low frequencies is high-enough compared to 1 so that steady-state error can be assumed to be zero. In Figure 4.9, the simulation circuit and frequency response for the PI-controller used in the proposed system is demonstrated.

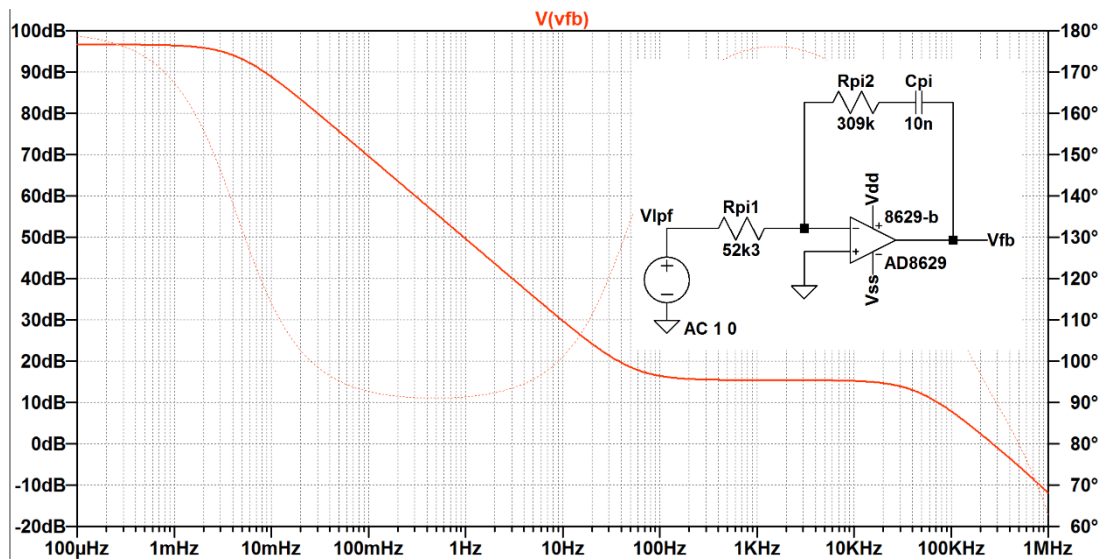


Figure 4.9: The simulation circuit and the frequency response of the PI-controller used in the proposed system. The DC gain of the block is limited by the open-loop gain of the OpAmp.

Another important consideration here is the phase contribution of the OpAmp at higher frequencies. The hasty reduction in the phase response after around 10 kHz can cause stability issues if not paid attention to. However in this case, the magnitude response of the system in the worst case scenario is known to go below 0 dB around 280 Hz (Chapter 3, Figure 3.13) which is in a safe region where the zero of the controller is still in charge of the phase response, and the controller can be used without any concerns about the stability.

#### 4.2.4. Behavioral Model of the Sensing Element

After the generation of the electrical blocks, an additional model of the sensing element is also created in SPICE environment. This way, all of the system can be simulated altogether within the same simulation environment with high electrical simulation precision. In Figure 4.10, the behavioral model of the sensing element is demonstrated along with its dedicated circuit symbol.

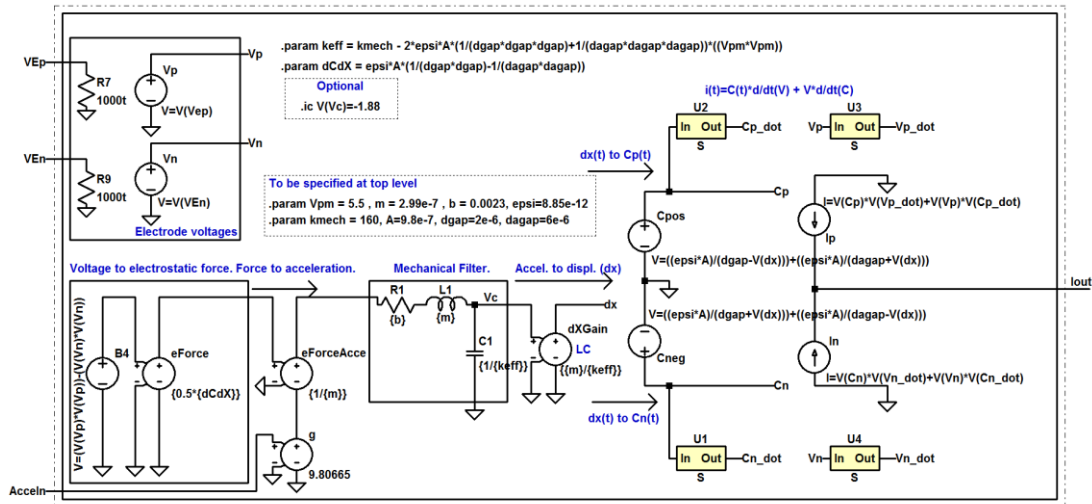


Figure 4.10: The behavioral model of the sensing element created in SPICE environment.

The capacitance behavior in this model is generated in a non-linear fashion, whereas the force relations are expressed with a constant sensitivity approach. So the model is neither highly accurate like the non-linear Simulink model, nor completely linearized like the linear model created again in Simulink; it can run with a sufficient amount of accuracy and still can be simulated in a very short simulation run-time. What must be noted that frequency domain analyses cannot be conducted using this model in SPICE; only transient analyses can be run.

The blocks *U1-4* are differentiation blocks created using 1 H inductors, simply taking the time-derivative of its input by a factor of 1. The model has 4 ports in total: ‘*VEp*’ and ‘*VEN*’ are the ports replacing the positive and the negative electrodes of the sensing element; ‘*AcceIn*’ is the port where the external acceleration is applied; and ‘*Iout*’ is the port outputting the net current leaking towards the pre-amplifier through the proof mass node.

#### 4.2.5. The Complete Accelerometer in SPICE

After all the constructional block models in SPICE environment are complete, the final simulations prior to implementation are run. In Figure 4.11, the final SPICE

circuit model of the proposed system is demonstrated. Note that the voltage regulator is not demonstrated in this circuit diagram.

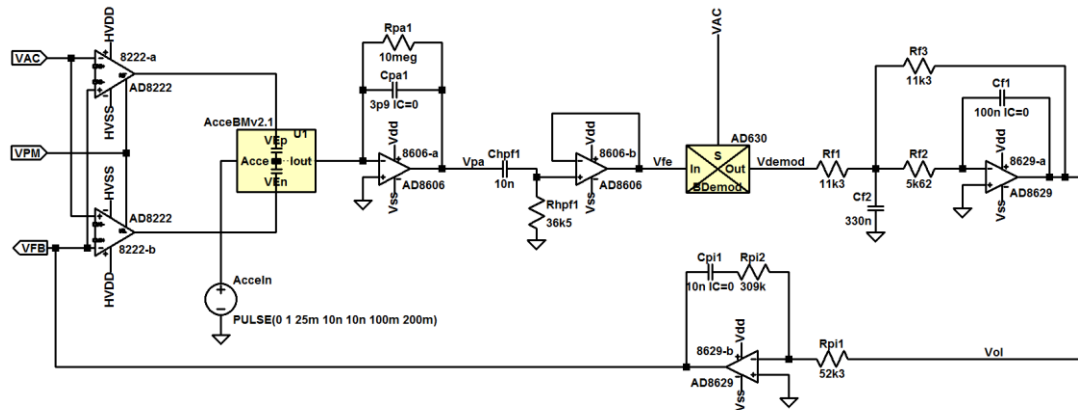


Figure 4.11: The SPICE simulation circuit of the proposed accelerometer.

As a demonstration of the functionality of this model and the consistency of all the models, the unit-g step response of all three models created are given in Figure 4.12. Note that these three models are the non-linear and linear models created in Simulink, and the SPICE circuit model.

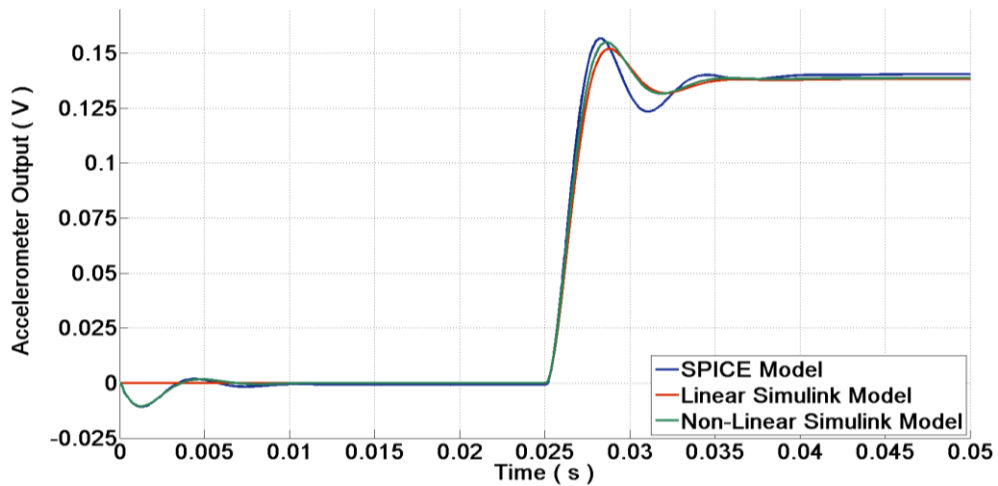


Figure 4.12: The demonstration of unit-g step responses of the Simulink and SPICE models in comparison. Note that a perfect fit between these responses are already not expected since certain simplifications are made dedicated to each model.

The demonstration of the SPICE simulation results is limited only with the step response for the step response of a system presents traces of complete dynamic and static behavior of it. Since all three models are consistent in their step responses, it is sufficient to present other only the step response of the SPICE model here.

### 4.3. Electromechanical Noise Analysis

In order to estimate the overall noise performance of the proposed system, each of the contributors are taken into account separately. The noise contributions of certain blocks are added together as either referred-to-input (RTI) or referred-to-output (RTO) noises in  $V/\sqrt{Hz}$  and  $N/\sqrt{Hz}$  units. Later, using the linear model as presented in Chapter 3-Figure 3.10, these specific noise sources are combined and referred to the input of the proposed system in  $g/\sqrt{Hz}$  units. In Figure 4.13, the major noise contributors in the circuit are demonstrated within the linear model of the accelerometer. In this figure,  $F_{n,brown}$  is the RTI Brownian noise of the sensing element;  $V_{n,fe}$  is the voltage equivalent noise generated by the overall front-end electronics;  $V_{n,mid}$  is the voltage equivalent noise of both RTI voltage noise of the PI-controller and RTO voltage noise of the low-pass filter combined.

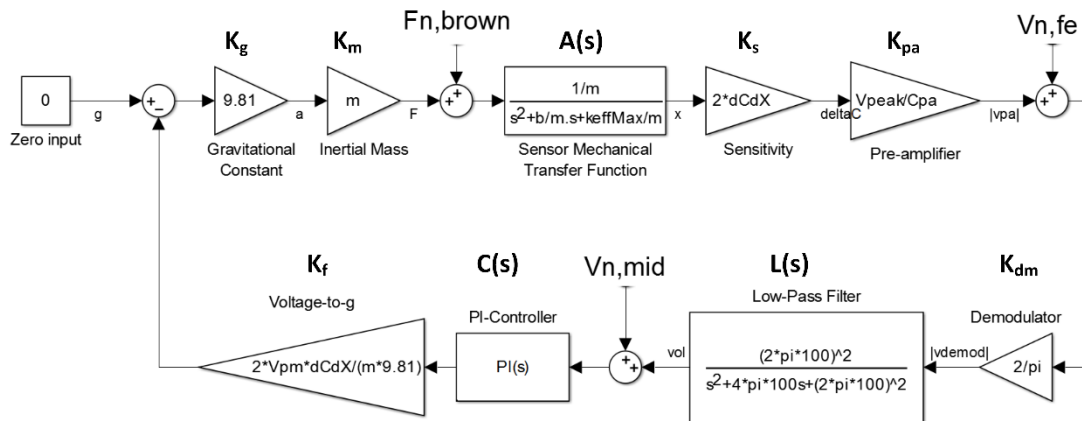


Figure 4.13: Major noise contributors of the proposed system demonstrated with the linearized closed-loop model.

The three major noise contributors can be referred to input of the complete closed-loop system in g-units using the gain of associated transfer functions in band of interest (DC-100 Hz). As an example, the transfer function used to refer the  $V_{n,mid}$  to the input of the closed-loop accelerometer is given below.

$$NG_{n,mid} = \frac{K_f C(s)}{1 + K_g K_m K_s K_{pa} K_{dm} K_f A(s) L(s) C(s)} \quad (4.17)$$

Note that considering the loop gain (the multiplication term in the denominator) is high enough, Equation 4.17 can be simplified as given in Equation 4.18 but such simplification is not used during the calculations for there are peaks in the magnitude responses affecting the gain values.

$$NG_{n,mid} \cong \frac{1}{K_g K_m K_s K_{pa} K_{dm} A(s) L(s)} \quad (4.18)$$

In Figure 4.14, the magnitude responses of these two noise gain transfer functions are demonstrated. Additionally in Table 4.4, each noise gain approximated as a constant, as used in the calculations, are presented.

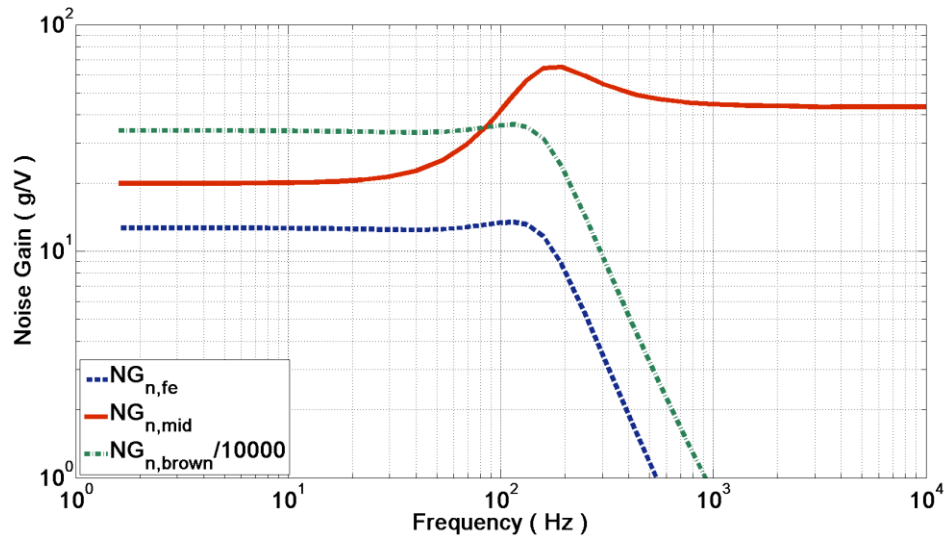


Figure 4.14: Noise gains referring the three major noise contributors to the input of the closed-loop accelerometer. As constant multipliers, maximum values of these frequency dependent gains are used.

Force-equivalent Brownian noise of the sensing element can be calculated using the following equation:

$$F_{n,Brown} = \sqrt{4k_B T b} \left( N/\sqrt{Hz} \right) \quad (4.19)$$

where ' $k_B$ ' is the Boltzmann constant in Joule per Kelvin; ' $T$ ' is the absolute temperature in Kelvins; and ' $b$ ' is the damping coefficient of the sensing element.

The investigation of the voltage-equivalent noise sources  $v_{n,fe}$  and  $v_{n,mid}$  is done in the following two sub-sections.

*Table 4.4: The three major noise contributors and the associated noise gain (NG\*) values to refer them to the input in g/√Hz units.*

Source	Description	Unit	NG*
$F_{n,brown}$	Brownian force equivalent noise generated by the sensing element	N/√Hz	$3.6 \times 10^5$
$V_{n,fe}$	Overall voltage equivalent output-referred noise of the front-end electronics	V/√Hz	13.5
$V_{n,mid}$	Combination of voltage equivalent output-referred noise of the low-pass filter and the input-referred noise of the PI-controller	V/√Hz	65.0

#### 4.3.1. Front-End Electronics

The output-referred voltage-equivalent noise of the front-end electronics is calculated using the circuit noise model given in Figure 4.15. Each of the noise contributors are assumed *white*, and referred to the output node,  $v_{fe}$ , after multiplication with the associated noise gains. Also note that the pre-amplifier is assumed to be operating as a pure capacitive amplifier and the high-pass filter has unity gain at the frequency of interest,  $w_c$ , which is the carrier frequency.

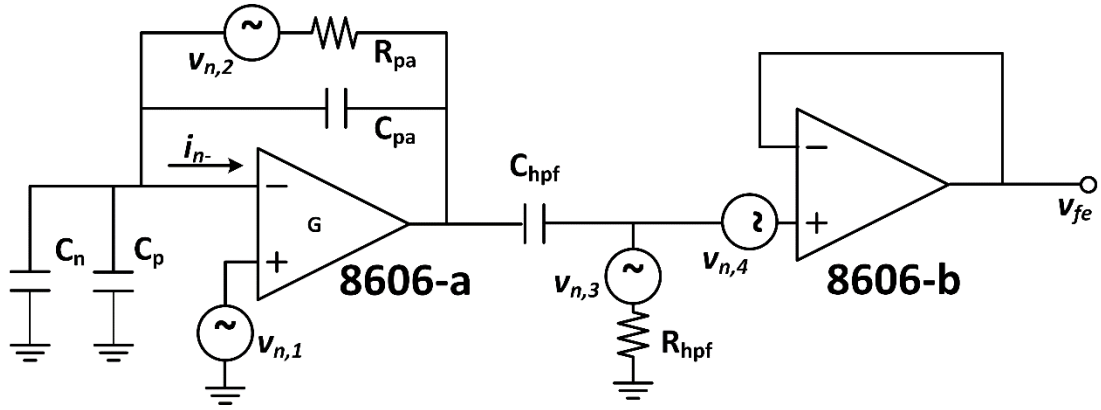


Figure 4.15: The electrical-noise circuit model of the front-end electronics.

In Table 4.5, the descriptions and the noise gains of each electrical noise source of the front-end electronics are given. The noise values of the active components are obtained from the component datasheet [33]. Note that  $C_p$  and  $C_n$  are the two electrode capacitances.

Total equivalent RTO voltage noise,  $v_{n,fe}$ , is calculated simply by square rooting the sum of squares of all the contributing RTO voltage noises.

Table 4.5: Noise sources of the front-end electronics and the associated noise gains.

Source	Description	Value	Noise Gain	RTO Noise (nV/ $\sqrt{\text{Hz}}$ )
$v_{n,1}$	Voltage noise of the pre-amplifier OpAmp	6.5 nV/ $\sqrt{\text{Hz}}$	$\frac{(C_p + C_n)}{C_{pa}}$	9.64
$v_{n,2}$	Thermal noise of the pre-amplifier feedback resistor	0.4 $\mu\text{V}/\sqrt{\text{Hz}}$	$\left  \frac{1}{j\omega R_{pa} C_{pa} + 1} \right _{\omega=\omega_c}$	91.10
$v_{n,3}$	Thermal noise of the high-pass filter resistor	24.6 nV/ $\sqrt{\text{Hz}}$	$\left  \frac{1}{j\omega R_{hpf} C_{hpf} + 1} \right _{\omega=\omega_c}$	0.55
$v_{n,4}$	Voltage noise of the buffer OpAmp	6.5 nV/ $\sqrt{\text{Hz}}$	1	6.50
$i_{n-}$	Inverting input current noise of the pre-amplifier OpAmp	10 fA/ $\sqrt{\text{Hz}}$	$\left  \frac{R_{pa}}{j\omega R_{pa} C_{pa} + 1} \right _{\omega=\omega_c}$	19.95
$v_{n,fe}$	Total equivalent RTO voltage noise	-	-	93.98

### 4.3.2. Low-Pass Filter and the PI-Controller

In Figure 4.16, the noise circuit model used to calculate the contribution of each noise source is demonstrated. Note that the low-pass filter capacitances are left as open-circuits since at the band of interest, they do not take any effect in the system operation.

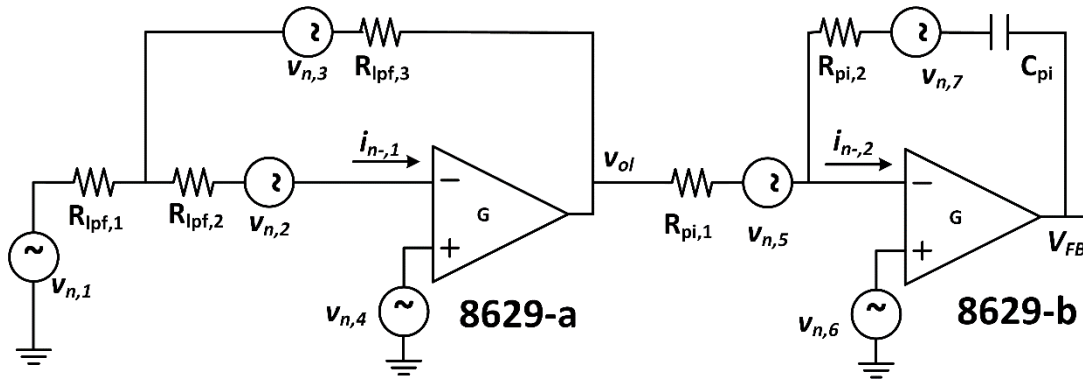


Figure 4.16: The electrical-circuit noise model of the low-pass filter and the PI-controller.

It must be noted that, the voltage equivalent noise contributions of both the low-pass filter and the PI-controller are referred to the output of the low-pass filter,  $v_{ol}$ , simply because it is simpler to refer the controller noise to its input. Additionally, the noise contribution of the PI-controller resistor,  $R_{pi,2}$ , is neglected since its noise gain is unity, and is very small compared to the scale factor.

In Table 4.6, noise gains (NG) of each noise source of the low-pass filter to refer them to the output; and the multiplication factors (MF) to refer the PI-controller noise components to its input are given.

Total equivalent voltage noise,  $v_{n,mid}$ , referred to the node,  $v_{ol}$ , is calculated simply by square rooting the summation of squares of all the contributing voltage noises.

Table 4.6: Noise sources of the low-pass filter and the PI-controller with the associated noise gains to refer to output (NG); and multiplication factors to refer to input (MF).

	Source	Description	Value	NG/MF	Referred Noise (nV/ $\sqrt{\text{Hz}}$ )
<b>Low-Pass Filter</b>	$v_{n,1}$	Thermal noise of the resistor $R_{lpf1}$	13.68 nV/ $\sqrt{\text{Hz}}$	$R_{lpf3}/R_{lpf1}$	13.68
	$v_{n,2}$	Thermal noise of the resistor $R_{lpf2}$	9.65 nV/ $\sqrt{\text{Hz}}$	$1 + R_{lpf3}/R_{lpf1}$	19.29
	$v_{n,3}$	Thermal noise of the resistor $R_{lpf3}$	13.68 nV/ $\sqrt{\text{Hz}}$	1	13.68
	$v_{n,4}$	Voltage noise of the OpAmp	22 nV/ $\sqrt{\text{Hz}}$	$1 + R_{lpf3}/R_{lpf1}$	44
	$i_{n,-1}$	Inverting input current noise of the OpAmp	5 fA/ $\sqrt{\text{Hz}}$	$R_{lpf2} + R_{lpf3}(1 - R_{lpf2}/R_{lpf1})$	0.05
<b>PI-Controller</b>	$v_{n,5}$	Thermal noise of the resistor $R_{pi1}$	29.43 nV/ $\sqrt{\text{Hz}}$	1	29.43
	$v_{n,6}$	Voltage noise of the OpAmp	22 nV/ $\sqrt{\text{Hz}}$	1	22
	$i_{n,-2}$	Inverting input current noise of the OpAmp	5 fA/ $\sqrt{\text{Hz}}$	$R_{pi1}$	0.26
	$v_{n,mid}$	Overall voltage equivalent noise at the node $v_{ol}$	-	-	63.50

### 4.3.3. Additional Noise sources

The two instrumentation amplifiers used in the feedback network (Figure 4.11) are noise sources as well. Each instrumentation amplifier's RTI voltage noise is calculated for unity gain configuration using the following formula as given in the datasheet [37]:

$$v_{n,ins} = \sqrt{8^2 + (75)^2} \text{ (nV}/\sqrt{\text{Hz}}) \quad (4.20)$$

Note that the input of the instrumentation amplifier is the output of the overall closed-loop system,  $V_{FB}$ . Thus, the input referred voltage noise of each instrumentation amplifier can be referred to the system input by division by the scale factor of the

closed-loop system. Considering there are two instrumentation amplifiers, the  $g$ -equivalent input referred noise contribution of these amplifiers are:

$$g_{n,ins} = v_{n,ins} * \frac{\sqrt{2}}{SF} (g/\sqrt{Hz}) \quad (4.21)$$

Additional considerations related with the feedback network are the noises fed to the system by the carrier signal and the proof mass voltage. The voltage noise of the function generator, through which the carrier signal is generated, is measured to be much smaller than other contributors, thus it is neglected. On the other hand, since the proof mass voltage is applied symmetrically onto the sensing element, any noise on it does not cause a net force noise on the proof mass and does not contribute to the noise performance. Also the noise contribution of the demodulator, AD630, is neglected.

#### 4.3.4. Overall Referred-to-Input Noise

After each noise source is investigated in detail in the previous sub-sections, they are summarized in Table 4.7 below.

Note that all of the calculations related with the noise are conducted using a MATLAB script. Due to notation simplifications and rounding, some insignificant inconsistencies in the values may be present.

*Table 4.7: The summary of the noise sources affecting the overall accelerometer and their  $g$ -equivalent values.*

Source	Description	Value	RTI Gain	RTI Noise ( $\mu\text{g}/\sqrt{\text{Hz}}$ )
$V_{n,mid}$	Equivalent noise of the low-pass filter and the PI-controller	63.50 nV/ $\sqrt{\text{Hz}}$	65.01	4.12
$F_{n,Brown}$	Brownian noise of the sensing element	6.17 pN/ $\sqrt{\text{Hz}}$	$3.62 \times 10^5$	2.23
$V_{n,fe}$	Equivalent noise of the front-end electronics	93.98 nV/ $\sqrt{\text{Hz}}$	13.55	1.26
$V_{n,ins}$	Input-referred, equivalent noise of the instrumentation amplifier	75.42 nV/ $\sqrt{\text{Hz}}$	10.22	0.77
$g_{n,total}$	Total input-referred, $g$ -equivalent noise of the closed-loop accelerometer	-	-	<b>4.92</b>

#### 4.4. Performance Estimation

In Table 4.8, the estimated performance of the accelerometer is summarized. The linearity performance estimation is not given for it is dominated by the symmetry of the sensor capacitances, which cannot be simulated or estimated. The scale factor (SF) is calculated for the electrical configuration parameters as introduced earlier. The velocity random walk (VRW) of the sensor is calculated by dividing the white noise (WN) level by  $\sqrt{2}$ . The estimated dynamic range (DR) is calculated for both the full-scale range (FSR, 78 g) and the half-scale range (HSR, 39 g).

*Table 4.8: The estimated performance summary of the proposed closed-loop accelerometer.*

<b>Property</b>	SF (mV/g)	FSR (g)	BW (Hz)	WN ( $\mu\text{g}/\sqrt{\text{Hz}}$ )	VRW ( $\mu\text{g}/\sqrt{\text{Hz}}$ )	DR, HSR (dB)	DR, FSR (dB)
<b>Value</b>	140	$\pm 39$	200	4.92	3.48	137	144

#### 4.5. Summary

In this chapter, the proposed system is transferred into electrical components from the mathematical models created in MATLAB. The realization of a system model in the circuit simulation tool, LTSpice, is demonstrated.

Moreover, the noise performance of the electromechanical system is estimated based on the actual components to be used in the implementation. This estimation is supported with a detailed noise analysis whose steps are introduced and discussed wholly. Even though the noise performance of the proposed accelerometer is to be affected by several other factors that cannot be modelled mathematically/electrically easily, the demonstration of the noise sources separately in a comparative manner gives a very good idea about the limits of the topology and the further improvements that can be made to improve the overall performance.

In the next chapter, the implementation of the proposed accelerometer and the test setups are introduced in detail.



## **CHAPTER 5**

### **IMPLEMENTATION AND TEST RESULTS**

In this chapter, the details related with the implementation and testing of the proposed accelerometer are introduced. In addition to the acceleration readout circuit, the peripheral circuitry, used either to improve the data acquisition quality or to give the test setup a rather more flexible essence, is also demonstrated with reasoning. Moreover, prior to introduction of the final test results which summarize the measured performance of the accelerometer, the tools used to enhance the test quality and efficiency are also demonstrated.

In Section 5.1, the realization of the proposed accelerometer using discrete components of surface-mount device (SMD) technology is presented with diagrams and the photograph of the implemented package. In Section 5.2, the design of the printed circuit board (PCB) which is used as an interface circuit assisting with the acquisition and supply connections is introduced. Also, demonstrations of additional measurement tools such as the data acquisition (DAQ) board or the Agilent VEE programs, are made. Section 5.3 shows how the readout circuit is tested for functionality before being interconnected with the sensing element; and in Section 5.4, an approach used to estimate the undercut values in both springs and the gaps of the sensing element is demonstrated. The final measurement results are presented in sub-sections dedicated to each test in Section 5.5. The chapter ends with Section 5.6 in which a brief summary of the chapter and the conclusions related with the measurement results are given.

## 5.1. Hybrid-Platform Package Implementation

As mentioned earlier, the proposed accelerometer is constructed using off-the-shelf, SMD discrete components. All of the integrated circuits (IC) and the passive components constructing the accelerometer are combined within a wide, 16-pin, dual in-line (DIL) metal package by Schott Corporation. Using a metal package for such an application is beneficial for it can be utilized as a Faraday’s cage given that it is connected to the ground. A very small PCB is designed and fabricated to be used within this package to interconnect all the electrical components. This PCB was manufactured at METU-MEMS Center using glass as the substrate, chromium and gold as the buffer and conductive material respectively. In Figure 5.1, the layout of this PCB is demonstrated with size information and the pin-out labels. Additionally in Table 5.1, the functions of the pins are listed.

*Table 5.1: The pin-out of the analog accelerometer package. Note that during closed-loop operation, pins ‘VFB’ and ‘PIOUT’ are connected to each other.*

Pin	Type	Description
HVDD	Input	+15 V supply
HVSS	Input	-15 V supply
GND	-	General ground
VAC	Input	Carrier signal input
VPM	Input	Proof mass voltage input
TSUP	Input	Temperature sensor supply
VFB	Input	Feedback voltage input
PIOUT	Output	PI-controller output
VDEMODO	Output	Demodulator output
VOL	Output	Low-pass filter output
TOUT	Output	Temperature sensor output

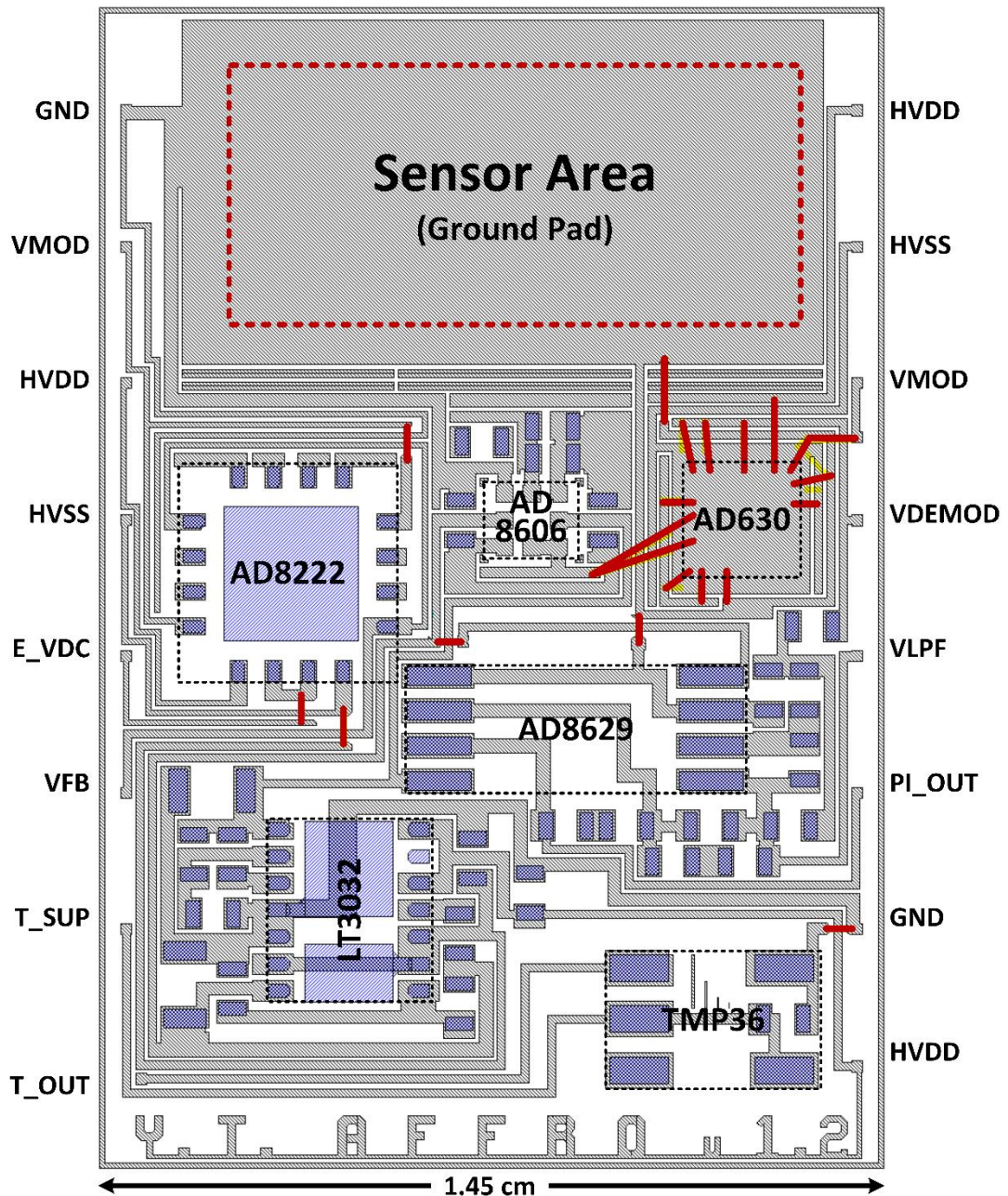


Figure 5.1: The glass-substrate PCB layout used to interconnect all the electrical components of the proposed analog accelerometer. Dashed lines show the components, red solid lines show the wirebonds. Overall board dimensions are 1.45x2.15 cm. Note that ‘AFFRO’ stands for ‘Analog Force-Feedback ReadOut.’

The integrated circuits and the 0402 and 0603 packaged passive components are hand-placed onto the substrate and fixated via their pads using Ablebond 8175

conductive epoxy. After the placement, the package is baked using Essemtec RO06Plus Reflow Oven at 130°C for one hour until the epoxy is fully cured. The epoxy is also applied manually by hand using an optical microscope. The sensing element is fixated in place by using carbon tape in order to be able to re-use the package with other sensors as desired. The missing connections on the metal routing; the connections of the chip-scale AD630; and the connections between the PCB and the package pads are made using Kulicke & Soffa manual wire-bonder. In Figure 5.2, a cross-sectional diagram showing the layers of the package is given. Also in Figure 5.3, a ready-to-run package is demonstrated.

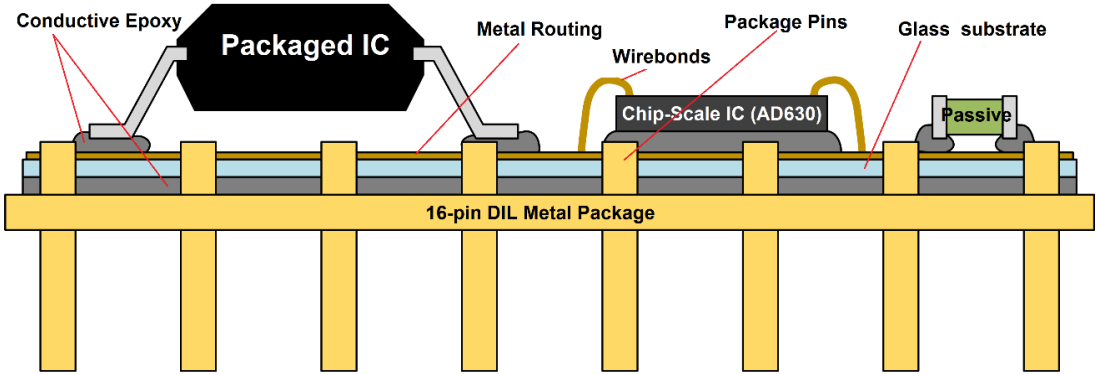


Figure 5.2: The cross-sectional diagram of the hybrid-platform package in which the proposed accelerometer is constructed.

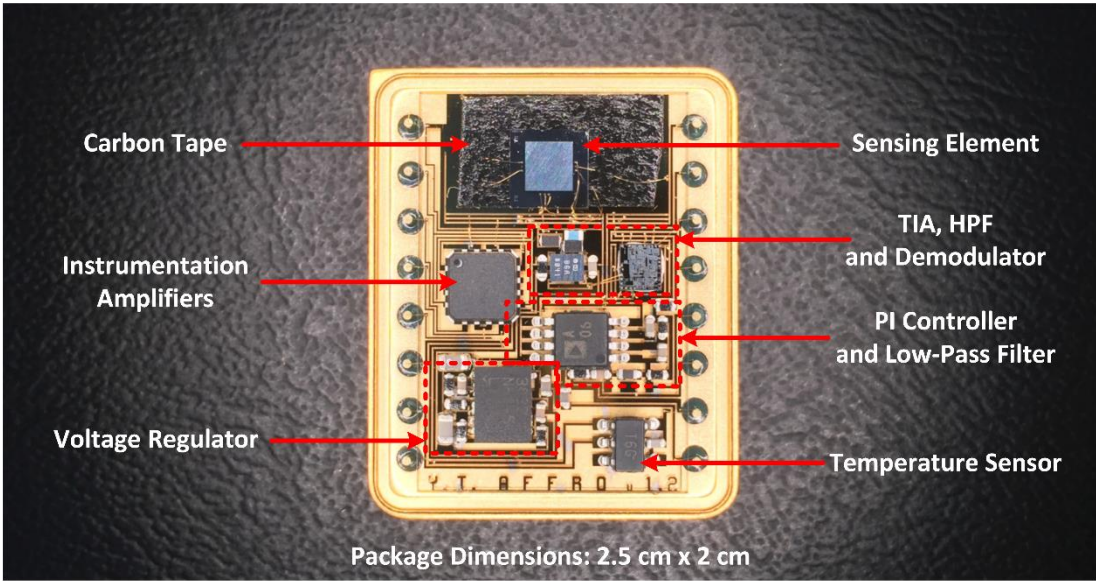


Figure 5.3: : A completed, ready-to-run analog accelerometer package.

As it also can be seen in Figures 5.1 and 5.3, in addition to the readout circuit and the sensing element, a temperature sensor (TMP36 by ADI, [40]) is also included inside the package as a utility component.

## 5.2. Interface Circuitry and Auxiliary Tools

Besides the analog closed-loop readout circuit as presented in detail in Chapter 4, additional circuitry and software are used during the tests. The reason for using such auxiliary tools is either to improve the acquisition quality or to increase the flexibility and efficiency of the test setup. In Figure 5.4, an overview of the core test circuitry is demonstrated in simplified blocks, and in the following sub-sections, the details about the additional tools are presented. Note that a passive (RC) band-pass filter is used to filter the output of the function generator rather than directly feeding it to the package. It is observed that this modification improved the data quality. Moreover, a output stage is used between the computer and the accelerometer package. This output stage, which is basically composed of a gain stage ( $\sim 30$  dB) configured in low-pass ( $\sim 250$  Hz) characteristics and a voltage buffer, is found extremely beneficial for measuring the noise performance of the accelerometer because it effectively suppresses the noise injected into the data from the DAQ board.

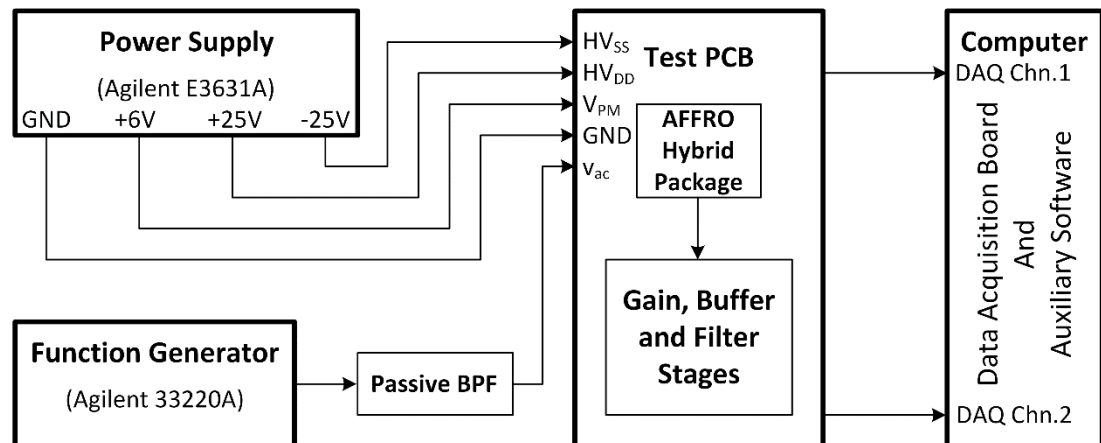


Figure 5.4: The overview of the core test setup which is used nearly for all the measurements.

### 5.2.1. Test PCB

Initial measurements of the implemented accelerometer are conducted using a pre-drilled circuit board. Shortly after these initial tests, it is decided that an interfacing PCB with proper by-passing and shielding is going to be beneficial as the first step to improve measurement quality. In Figure 5.5, the circuit layout of the double-sided test PCB, AFFROv1.1\_Test\_REV1, is given. Also in Figure 5.6, a picture of the manufactured PCB is demonstrated.

There are three two-state configuration switches on the test PCB. The first one selects whether the proof mass voltage is going to be fed to the package externally via a power supply or it will be generated by a voltage reference IC inside the package. The second switch sets the configuration of the readout circuit to either open- or closed-loop. And the last switch either includes the on-PCB output stage into the circuit or directly feeds the closed-loop output of the accelerometer to the BNC output connector on the PCB.

A grid of pads, intended to be used for the PI-controller passives, is also included on the PCB. This gives the user the freedom to be able to connect the PI-controller's passive components outside of the package with standard through-hole components. However this feature is almost never used for carrying the inverting input of the controller OpAmp outside the package for such connections caused the output data to deteriorate. Another feature of the PCB is the auxiliary dual OpAmp and the grid of pads placed around it. This section is added in case an extra amplifier is needed for some reason, and is used several times during the tests.

The increase in the quality of the measured data after this PCB is fabricated was obviously significant. Without any need for a revision in the PCB, this board is used for almost all of the tests where it was applicable.

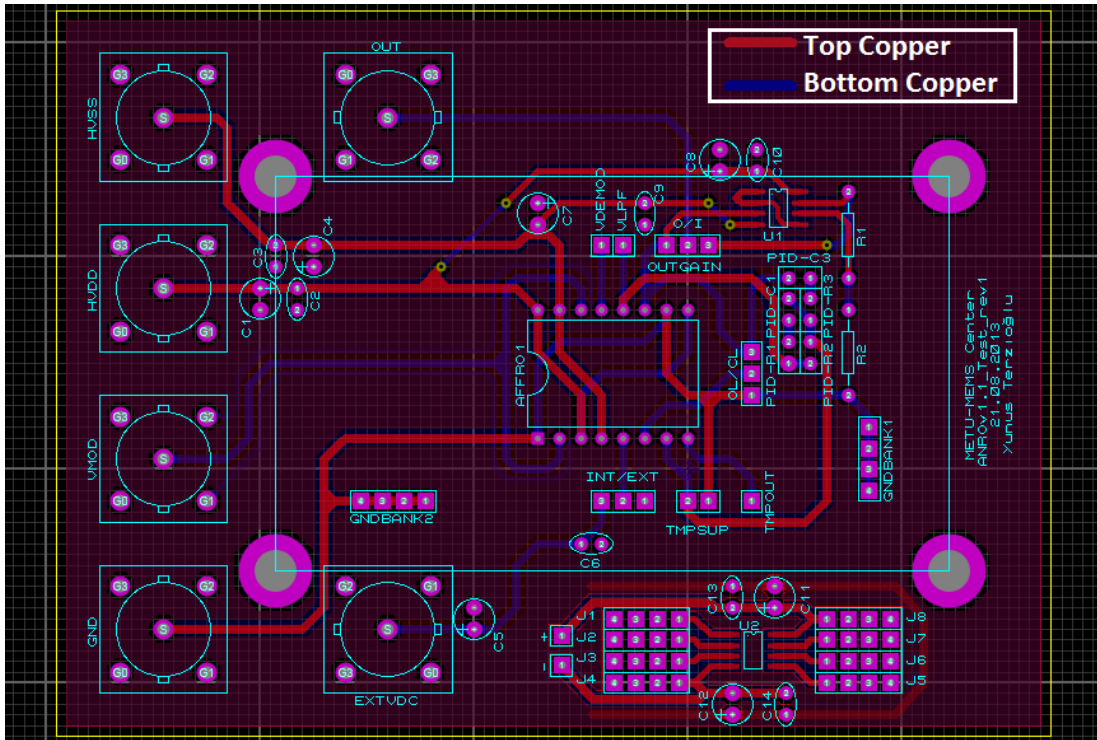


Figure 5.5: The circuit layout of the double-sided test PCB.

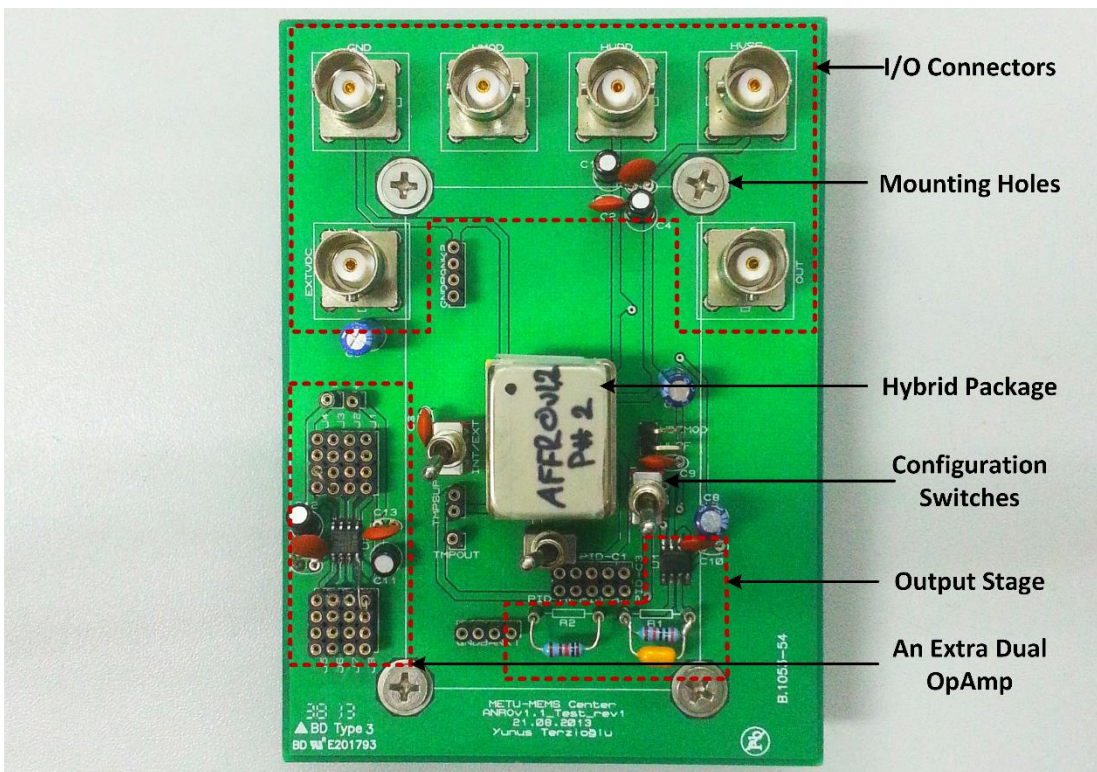


Figure 5.6: The manufactured double-sided test PCB.

### 5.2.2. Data Acquisition and Test Automation

A computer with a National Instruments PCI-4461 data acquisition (DAQ) board and LabView Signal Express software is used during the tests. The DAQ board has two analog input channels which are used in different configurations for different tests, and as the acquisition software, Signal Express is used.

In addition to the acquisition tools, Agilent VEE software is also used for test automation, and such automation is desired for the tests which would be extremely time-consuming otherwise. One of the situations where such software is found necessary occurred when the accelerometer is intended to be tested under various values of electrical configuration parameters to observe performance changes and try to find an optimum configuration. Note that these parameters are the proof mass voltage, the carrier signal amplitude and the carrier signal frequency. Another situation where the automation is used occurred during the bias repeatability tests (Section 5.5.5) which are, yet again, very long tests.

For the automation, the features of Agilent VEE, Signal Express, and the DAQ board are fused together. The first analog channel of the DAQ board is used for acquisition. The second one is used as a voltage trigger input fed by power supply driven by the VEE software which effectively controls the test flow. A Signal Express program is created for the acquisition such that every time a trigger is given through the second analog channel of the DAQ board, a new data log is created and data recording is started. And once the trigger input drops below a certain voltage (power supply shut down) recording stops and the log is saved. This way, loads of data is acquired easily, and by using dedicated MATLAB scripts the data is processed into an easily observable graphical form to monitor the accelerometer behavior. In Figure 5.7, the generic block diagram of the automated test setup used in the scope of this thesis is given. Additionally in Figure 5.8, the VEE program created to test the accelerometer under different values of proof mass voltage is given as a sample. In the very specific program as given in Figure 5.8, the proof mass values ranging from 5 V to 6 V is applied on the accelerometer with 0.1 V increments for 10 separate runs prior to which a 600 seconds of warm-up time is given to the device under test (DUT).

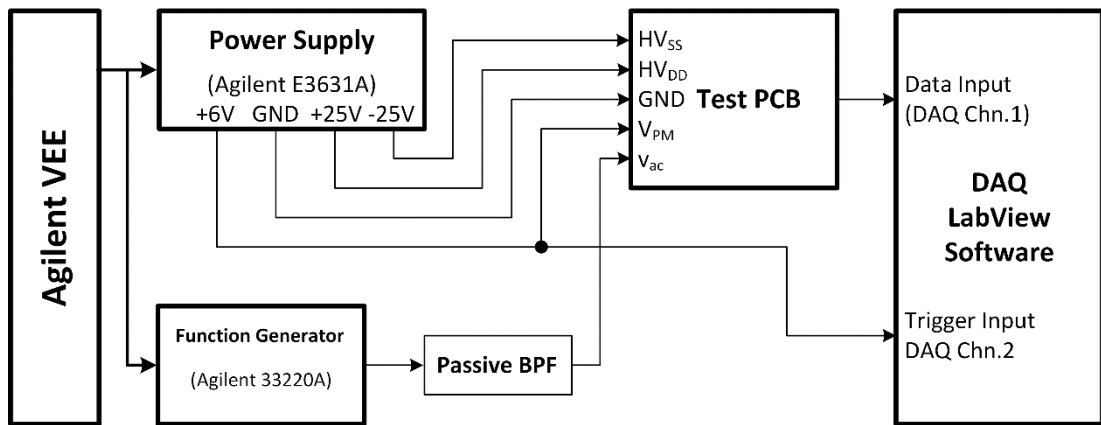


Figure 5.7: The generic block diagram of the automated test setup used in the scope of this thesis.

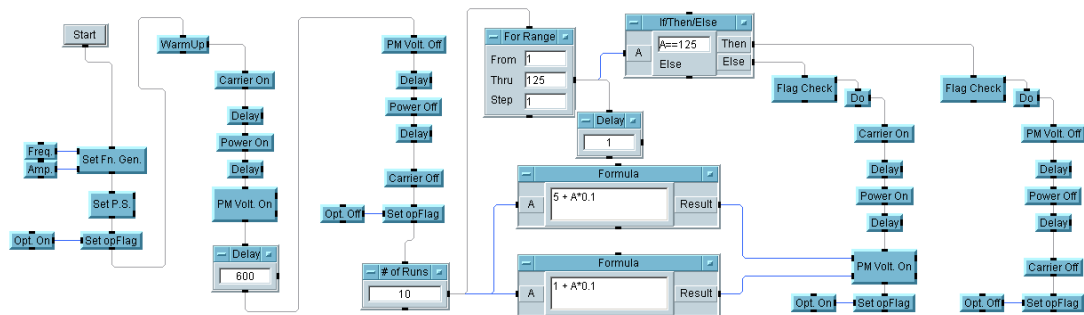


Figure 5.8: The Agilent VEE program created to test the accelerometer performance under different values of proof mass voltage.

### 5.2.3. Rotary Table

In order to apply acceleration inputs greater than  $\pm 1$  g and measure the linearity performance of the accelerometer, a rotation table by Ideal Aerosmith Incorporated is used. The accelerometer is fixed on the table such that sensitive axis of it is in line with the center of rotation. This way the centrifugal force exerted on the accelerometer is used to mimic applied acceleration. Note that during the tests conducted using the rotary table, the test PCB could not be used because the electrical connections between the outside and the rotary table is maintained by ribbon cables running on slip rings.

### 5.2.4. Shaker Table

The operation bandwidth of the accelerometer is measured using an LDS vibration table. A handy feature of this table is that it is driven in closed-loop using a reference piezoelectric accelerometer placed on the table. In order to be able to mount the test PCB onto the table, a size-adjustable PCB holding adapter is designed and machined out of stainless steel at METU-MEMS Research Center.

### 5.3. Circuit Functionality Tests

Prior to testing the complete accelerometer in closed-loop, the open-loop readout electronics of the readout circuit is tested without a sensor. A test capacitance of equal value of the pre-amplifier feedback capacitor is already placed inside the package. The AC carrier signal is applied to the pre-amplifier through this capacitance and the outputs of the demodulator and the low-pass filter is investigated using the package pins *VDEM* and *VOL* which are already placed for this specific reason. After the waveforms in these two nets are as expected based on the simulation results are verified using an oscilloscope, the output of the PI-controller is monitored to verify that it is saturated at the rail, bearing the opposite sign of the low-pass filter output voltage. In order to monitor other nets when needed, needle type probes are used to directly contact the metal routings on the glass PCB inside the package. The circuit configuration in which the functionality of the open-loop readout electronics is tested is demonstrated in Figure 5.9.

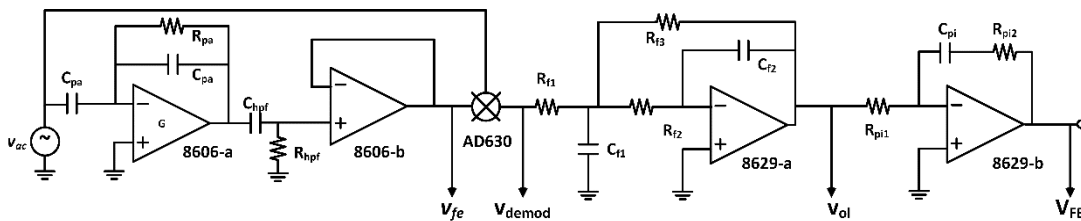


Figure 5.9: The circuit configuration in which the functionality of the open-loop readout electronics is tested.

#### 5.4. Sensor Undercut Characterization

During the fabrication, the geometrical details of the sensing elements might change compared to the design values due to probable fabrication imperfections. One of the common defective issues causing imperfections is the *undercut*. The undercuts taking place during the fabrication steps result in the widening of the capacitive gap separations and thinning of the suspending springs. Both of these effects alter the dynamic and the static properties of the sensing element compared to the design values. The changes in these properties are critical especially for closed-loop systems for they result in changes in critical system parameters such as loop gain. For that reason, in order to estimate the variations in the device geometry, two very fundamental tests are usually utilized: Resonance tests and CV measurements.

The resonance frequency of the sensor can simply be formulated with the following equation:

$$w_r = \sqrt{\frac{k_{eff}}{m}} \quad (5.1)$$

where ' $w_r$ ' is the resonance frequency in rad/s; ' $k_{eff}$ ' is the effective spring constant; and ' $m$ ' is the inertial mass. Thus, based on this test, the parameters affecting the effective spring constant values can be estimated based on the resonance tests, considering the change in the inertial mass is insignificant.

During the CV measurement, the proof mass is pulled in either direction by using an actuating voltage,  $V_a$ , and the capacitance of either electrode,  $C_{elec}$ , is measured simultaneously for every value of the actuating voltage. Eventually a plot with  $V_a$  in x-axis and  $C_{elec}$  in y-axis is obtained. The relation between this two axes is based on the actuation principles as discussed earlier in Chapter 2, and it is basically governed roughly by an equation in the following form:

$$C_{elec} = \frac{\epsilon A}{d - \left( \frac{0.5 \frac{dC}{dx} V_a^2}{k_{eff}} \right)} \quad (5.2)$$

where ' $\epsilon$ ' is the permittivity of air; ' $A$ ' is the overlap area of the parallel-plate capacitor; ' $d$ ' is the plate separation; and ' $dC/dx$ ' is the capacitance sensitivity. Thus,

based on this measurement, the parameters affecting the sensor sensitivity and the effective spring constant can be extracted.

One issue related with the undercuts is the possibility that the actual undercut values for the springs and the capacitive gap separations are different than each other due to geometry differences in the associated regions of the sensing element. Considering such a case is present, the sensitivity and the effective spring constant of the sensing element will be functions of two different parameters: the spring undercut and the gap undercut. Solving the mathematical equations governing resonance frequency value and the capacitance of an electrode for a given amount of actuation together, the undercut values of the springs and the capacitive gaps can be extracted separately based on the results of these two tests using a software such as MATLAB.

In scope of this thesis, an alternative method for estimating the undercut values is developed. In this method, instead of using resonance and CV tests, pull-in voltage and the open-loop scale factor of the accelerometer using the proposed readout circuit is measured and utilized to estimate the undercuts separately. Note that these tests are relatively easier to conduct compared to the other resonance and CV tests.

The pull-in voltage is measured by increasing the *proof mass voltage* gradually until the effective spring constant drops below zero and the sensor pulls in, and the proof mass voltage at this point is recorded. The pull-in point can be determined by observing the current drawn from the supply that the proof mass voltage is fed from. This current should normally be almost zero, and greater than zero for pull-in condition.

The open-loop scale factor is simply measured by recording the open-loop readout electronics output ( $v_{ol}$ ) in plus and minus 1 g; subtracting both output voltage values from each other; and dividing by two in order to get the scale factor in V/g units. Note that in this measurement, no proof mass voltage is applied on the sensing element in order to exclude spring softening from the equations.

Even though the undercut values of the sensing element used with the proposed accelerometer are negligibly small, this method is used for some other sensors that the

readout circuit is operated with earlier. For demonstration of this method, a *case study* based on an *arbitrary sensing element* is given below.

At the first step of this method, after the voltage,  $V_{k=0}$ , that causes the effective spring constant to drop below zero is recorded, a 3D plot using mathematical expression for the effective spring constant on a mesh-grid composed of the spring and gap undercuts is drawn. The equation for this surface is given below as functions of spring and gap undercuts;  $u_s$  and  $u_g$  respectively.

$$k_{eff}(u_s, u_g) = k_{mech}(u_s) - \frac{2\epsilon AV_{k=0}}{(d_g(u_g))^3 + (d_{anti-g}(u_g))^3} \quad (5.3)$$

The intersection of the surface governed by Equation 5.3 with the zero plane is calculated using a MATLAB sub-script coded specifically for this purpose. The intersection line gives the possible solution pairs of spring and gap undercuts satisfying the measured pull-in voltage. In Figure 5.10, this solution line and the effective spring constant surface is given.

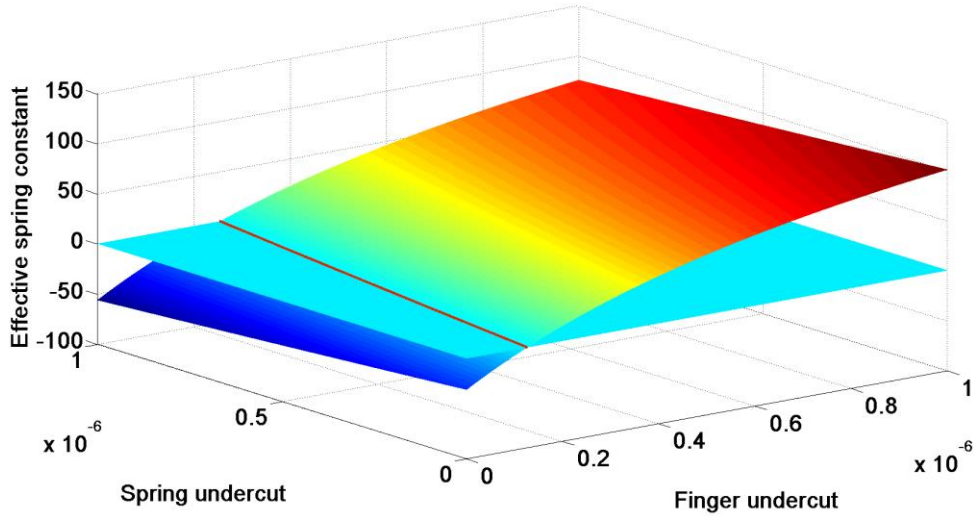


*Figure 5.10: Case study Step 1: The surface governed by the effective spring constant equation as a function of spring and gap undercut values. The solution line in accordance with the measured pull-in voltage is the intersection of this surface with the zero plane.*

As the second step, another 3D plot using mathematical expression for the open-loop scale factor on a mesh-grid composed of the spring and gap undercuts is drawn. The equation for this surface is given below as functions of spring and gap undercuts.

$$SF_{ol}(u_s, u_g) = 9.81m \frac{1}{k_{mech}(u_s)} \left( 2 \frac{dc}{dx}(u_g) \right) V_{peak} \frac{1}{C_{pa}} \frac{2}{\pi} \quad (5.4)$$

The derivation of Equation 5.4 can be made using the linear model given in Chapter 3, Figure 3.10.

The intersection of the surface governed by Equation 5.4 with the constant plane of the measured open-loop scale factor gives the possible solution pairs of spring and gap undercuts. In Figure 5.11, this solution line and the scale factor surface is given.

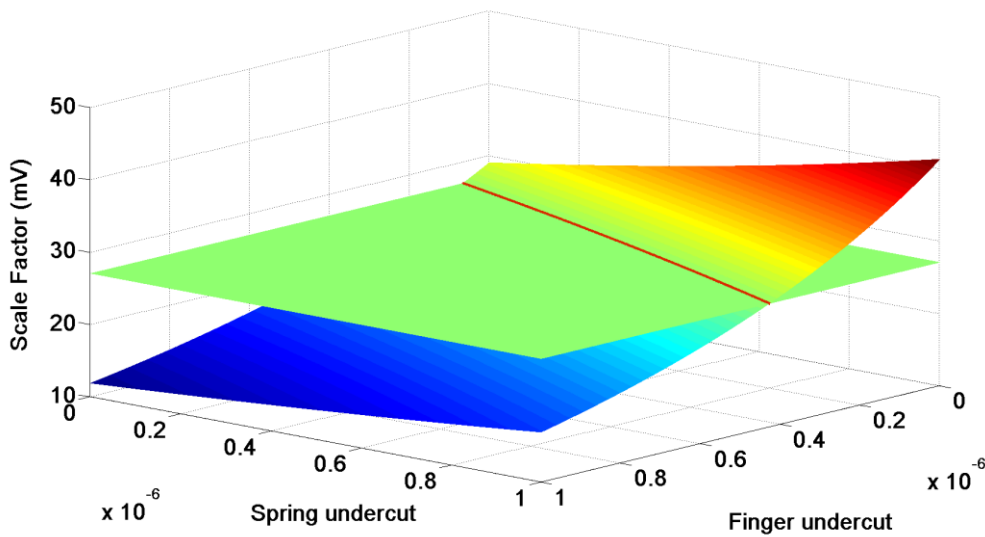


*Figure 5.11: Case study Step 2: The surface governed by the open-loop scale factor equation as a function of spring and gap undercut values. The solution line is the intersection of this surface with the constant plane of measured scale factor.*

In the third and final step of this method, the 2D projections of the solution lines in Figures 5.10-11 are plotted in the same figure, and the intersection of these two lines

gives the solution pair for the spring and gap undercut values satisfying the measurement results of the pull-in and scale factor tests. In Figure 5.12, this final plot is demonstrated.

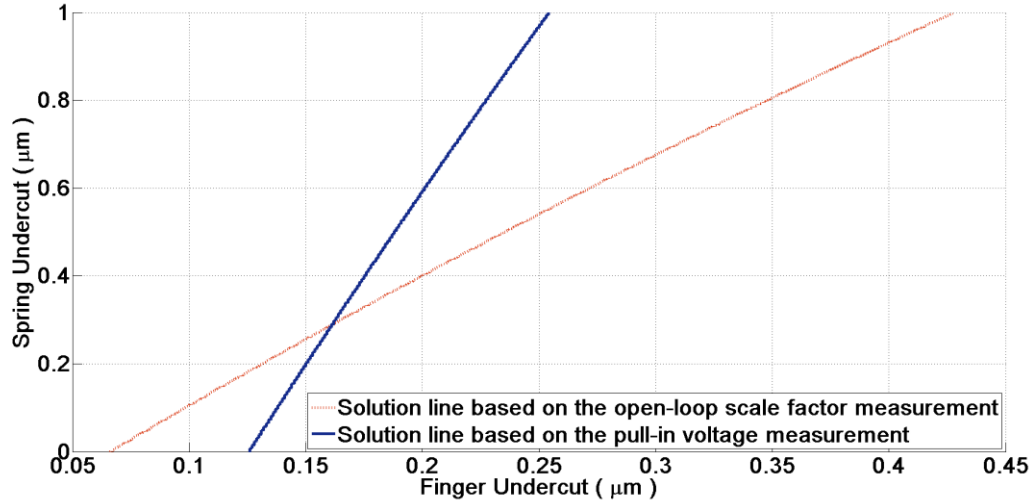


*Figure 5.12: Case study Step 3: The two solution lines obtained from the first two steps of the undercut estimation case study. The intersection of both lines gives the solution pair of spring and finger undercut values.*

As it can also be seen in Figure 5.12, the gap widening is around 0.16 µm and the spring thinning is around 0.29 µm for this specific case study.

A similar approach can also be applied to the results of the resonance and CV tests in order to estimate the gap and the spring undercuts with an even higher precision, and having estimated these two values separately, the complete system can be modelled with much higher accuracy.

## 5.5. Test Results

In the following sub-sections, the important details about the tests conducted on the proposed closed-loop accelerometer and the related figures are presented if any. All of the test results are presented together in Table 5.3 in Section 5.6, Summary and Conclusions. The detailed definitions of the measured performance parameters are described in detail in the IEEE standards given in references [5].

### 5.5.1. Power-Up

A specific power-up sequence is used to start operating the accelerometer. Firstly, the carrier signal is applied, followed by the application of the rail voltages. Finally, the proof mass voltage is increased gradually from 0 V to 5.5 V. In some power-up scenarios where this sequence is not followed, it is seen that the accelerometer pulls in. Even though such incident occurred rarely, it has been observed that if the power-up sequence is followed directly, the accelerometer powered up properly every time. Note that this routine can possibly be overcome by using a low-pass filter between the circuit and the proof mass voltage source allowing the applied voltage to increase gradually, but the issue is not investigated in detail.

Apart from the power-up sequence, the settling time of the proposed accelerometer should also be taken into account. In Figure 5.13, normalized output of the closed-loop accelerometer after power-up is demonstrated.

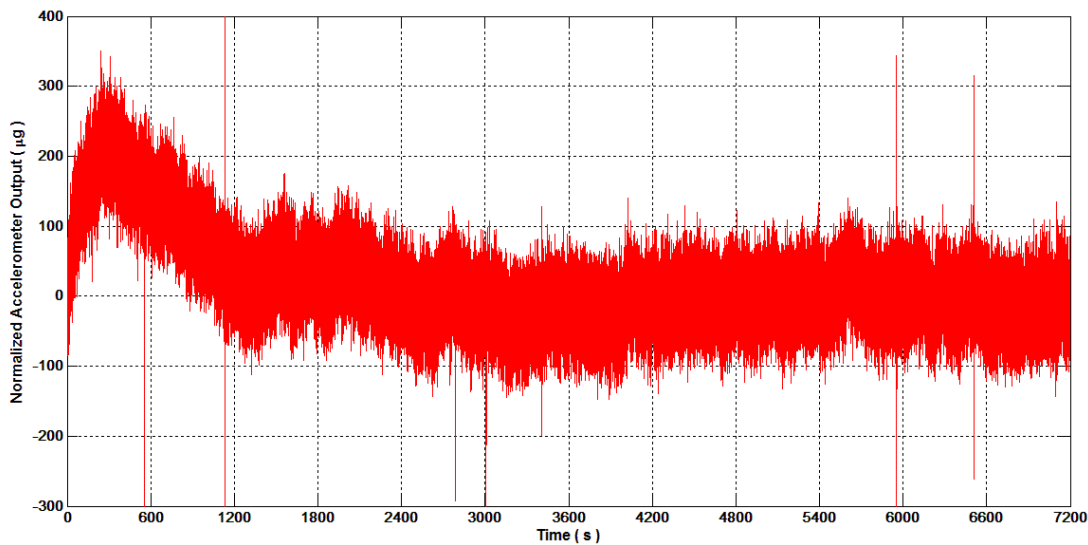


*Figure 5.13: The normalized output behavior of the closed-loop accelerometer shortly after power-up. It takes around 20 minutes before the system settles in its nominal operation point.*

As it also can be seen in Figure 5.13, it takes around 20 minutes before the system settles in its nominal operation point. During this 20-minute period, called the

*warm-up*, data collected from the accelerometer is not reliable, and should not be used for any sort of analysis.

### 5.5.2. Scale Factor, Off-set and Range

The scale factor of the proposed accelerometer is measured by using the output of the accelerometer in + and –1 g conditions. After ~10 seconds of data is collected in both positions, it is averaged to constant values. Then the scale factor in V/g is calculated using the following formula:

$$SF = \frac{v_{out,+1g} - v_{out,-1g}}{2} \quad (5.5)$$

The reason that 0 g output of the accelerometer is not used for this measurement is because the sensing element is much more sensitive to placement errors around 0 g position than  $\pm 1$  g positions. The percent error given 1° of placement error for 0 and 1 g positions can be calculated by the following equations:

$$e_{pc,1g} = \frac{|SF \cdot \sin(90) - SF \cdot \sin(89)|}{SF} * 100 \cong 0.015 \quad (5.6)$$

$$e_{pc,0g} = \frac{|SF \cdot \sin(0) - SF \cdot \sin(1)|}{SF} * 100 \cong 1.74 \quad (5.7)$$

Considering the fact demonstrated by Equations 5.6 and 5.7, the 0 g off-set output of the accelerometer is also calculated using the + and –1 g outputs of the accelerometer using the formula given below.

$$OS = \frac{v_{out,+1g} + v_{out,-1g}}{2} \quad (5.8)$$

The measured scale factor is around 156 mV/g for 5.5 V of proof mass voltage with a ~47 mV of zero-g off-set. Even though the accelerometer could not be tested at such high acceleration inputs because of the maximum allowed rotation speed of the rotary table is not sufficient, the range of the accelerometer can be estimated using the scale factor as:

$$R_{est} = \frac{5.5}{\pm 0.156} \cong \pm 35 g \quad (5.9)$$

### 5.5.3. Linearity

The linearity performance of the accelerometer is measured using the rotary table. After the accelerometer is placed in an orientation such that the centrifugal force acts as a positive g input, rotation speed of the table is increase in a step-by-step manner until the maximum possible rotation speed is achieved. Later the accelerometer is removed and replaced in the opposite orientation to measure linearity in negative g input. This replacement cannot be exact in terms of sensitive axis orientation. Because of this, positive and negative linearity performances are demonstrated separately.

Moreover, the distance from the center of rotation is different in both orientations, the magnitudes of centrifugal force with respect to the rotation speed are different. Because of this, the step sizes and the maximum input g values are also different for positive and negative linearity measurements.

In Figure 5.14, the linearity test results are demonstrated. Also in Figure 5.15, the deviation of the output from an ideal line for the given scale factor is shown.

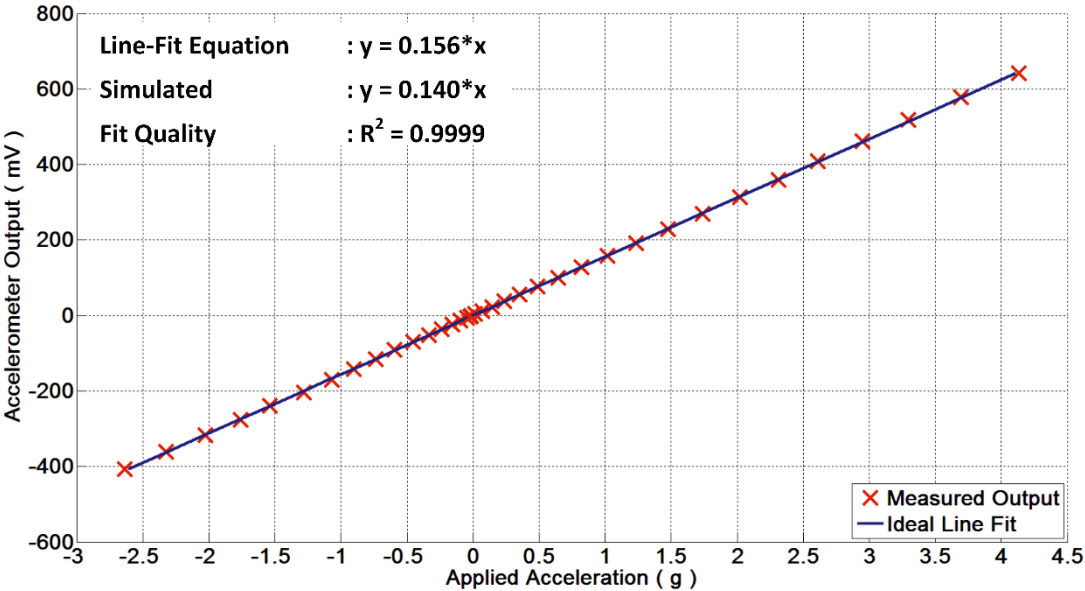


Figure 5.14: The linearity performance of the accelerometer demonstrated with an ideal line-fit for the given scale factor.

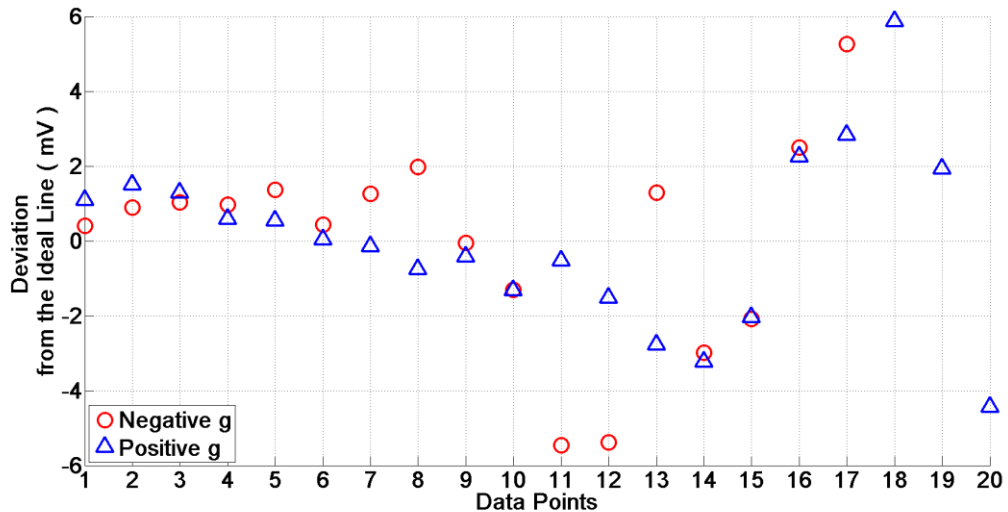


Figure 5.15: The deviation of the output of the accelerometer from the ideal line-fit at each point of linearity measurement.

The maximum deviation from the ideal line-fit is divided by the estimated range in order to calculate the maximum non-linearity. In Table 5.3 the calculated linearity performance is given.

#### 5.5.4. Velocity Random Walk and Bias Instability

There are various methods for characterizing the noise performance of an accelerometer [41]. Among these methods, Allan Variance analysis is used for it is a very standard and neat method to determine the velocity random walk (VRW) and bias instability (BI) performances of an inertial sensor. The details about this analysis can be found in [42].

In order to use in Allan Variance analysis, a 2-hour-long data is collected from the accelerometer. During this time, the accelerometer is placed in 0-g position and kept stationary. This data is collected at night time because the external noise sources such as cars passing or people walking in the corridors are much less then. Moreover, several media such as sand and sponges are used in order to insulate the test PCB from outer vibration sources. However it is observed that the results are best if the PCB is directly placed on 4 bolts that are fixed onto the board through mounting holes.

After the acquisition is complete, the freeware AlaVar 5.2 is used for the post processing. In Figure 5.16, the Allan Deviation plot of the data collected from the proposed accelerometer is given with the markers demonstrating the VRW and BI performances.

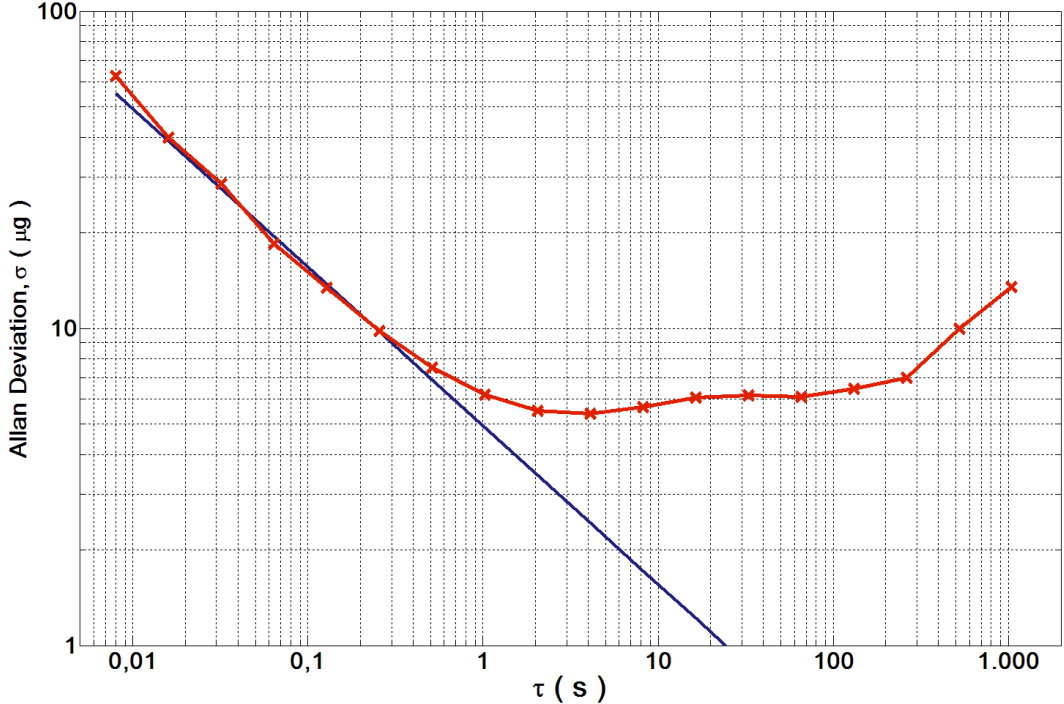


Figure 5.16: The Allan Deviation plot of the 2-hour-long data collected from the proposed accelerometer demonstrated along with the -0.5 sloped line fit.

**5.5.5. Bias Repeatability**

In order to determine the bias repeatability, the accelerometer output is collected for 15 minutes and the package is shut-down to cool for 20 minutes while the sensor rests stationary in 0 g position. After this sequence is done for 5 times, the deviation of the averages of each data set with respect to the reference reading is calculated to obtain the bias repeatability performance of the sensor. Note that the reference reading is taken as the first of five measurements. Each run of the bias repeatability measurements takes around 3 hours, and several runs are conducted. Because of that, an automated test setup as described in Section 5.2.2 is utilized. In Table 5.2, one set

of bias repeatability data collected from the proposed accelerometer is demonstrated, and its result is evaluated in the ‘Standard Error’ column.

*Table 5.2: The evaluation of bias repeatability performance of the proposed accelerometer.*

<b>Bias Error 1</b>	<b>Bias Error 2</b>	<b>Bias Error 3</b>	<b>Bias Error 4</b>	<b>Bias Error 5</b>	<b>Standard Error</b>
0 mg	-0.19 mg	-0.09 mg	0.27 mg	0.37 mg	<b>0.20 mg</b>

## **5.6. Summary and Conclusions**

In this chapter, the implementation steps of the proposed accelerometer is presented in detail. In addition, the test setups for certain measurement such as the bandwidth measurement and the auxiliary tools used in these setups are demonstrated with reasoning. The step for verification of the readout circuit functionality, and an analytical method used to characterize the imperfections in the fabricated sensing element is also introduced. Finally, the test measurement results based on the presented setups and tools are demonstrated and the critical details about each measurement are discussed in separate sub-sections.

The measurement results showed that the simplicity of the readout circuit has paid off. By using linear and non-linear models of the proposed accelerometer with sufficient amount of model detailing, the performance of the implemented accelerometer is found very close, almost spot-on, to the simulated models of the proposed system. In Table 5.3, both simulated and measured performance summary of the proposed accelerometer is given in a comparative manner.

In the following chapter, further applications realized using the proposed accelerometer are presented, highlighting the adaptability of the readout circuit.

Table 5.3: Simulated and measured performance summary of the proposed accelerometer.

Parameter	Simulated	Measured	Unit
Warm-Up Time	NA	1200	s
Scale Factor	140	156	mV/g
0 g Off-Set	0	0.3	g
Range*	±39	±35	g
Non-Linearity	0 %	0.5 %	-
Bias Repeatability	NA	0.2	mg
Bandwidth	200	-	Hz
Velocity Random Walk	3.48	4.9	μg/√Hz
Bias Instability	-	5.4	μg
Dynamic Range (MR)	123	120	dB
Dynamic Range* (FSR)	144	140	dB
Dynamic Range* (HSR)	137	134	dB

\* : Value is estimated by calculations

MR : Measured range (6.9 g)

FSR : Full-scale range (70 g)

HSR : Half-scale range (35 g)

## CHAPTER 6

### FURTHER APPLICATIONS USING AFFRO

One of the main motivations behind the implementation of the proposed accelerometer readout circuit is to have a circuit that is flexible enough to be used for various applications related with acceleration sensing, and to be easily adaptable to be used with different sensor structures. In this chapter, two applications realized using the proposed analog force-feedback readout circuit (AFFRO) are presented demonstrating flexible nature of the system.

In Section 5.1, the use of AFFRO to realize a multi-axis accelerometer incorporating a single-proof mass sensing element in order to sense acceleration in two axes [43]. In Section 5.2, not only the use of AFFRO for acceleration sensing in z-axis (out-of-plane) is demonstrated, but also a novel method for sensing acceleration differentially using two types of different electrode topologies is presented [44].

#### **6.1. A Single-Proof Mass, Two-Axis Accelerometer**

In many accelerometer applications such as inertial measurement units (IMU), a multi-axis (usually three) accelerometer is used. Realization of such an accelerometer can be accomplished using a sensing element incorporating one proof mass for acceleration sensing in each axis [11], [16]. In some other applications, [14], a single proof mass is utilized for sensing in all the axes. This approach, compared to a multi-proof mass accelerometer, results in a higher sensor performance: The effective sensitivity per chip area is enhanced; and since the complete chip area is assigned to a single proof mass, input referred g-equivalent Brownian noise is reduced with the utilization of a higher inertial mass. The problem with such accelerometers is the

phenomenon referred as *cross-axis sensitivity* [45]. The cross-axis sensitivity can simply be explained as the acceleration input in one axis affecting the readout output in any other axis.

Using the AFFRO, a two-axis accelerometer with very low cross-axis sensitivity using a single-mass sensing element can be achieved. The theory behind such achievement is by splitting the readout of each axis in frequency domain. In Figure 6.1, the block diagram of the implemented two-axis accelerometer using AFFRO is presented.

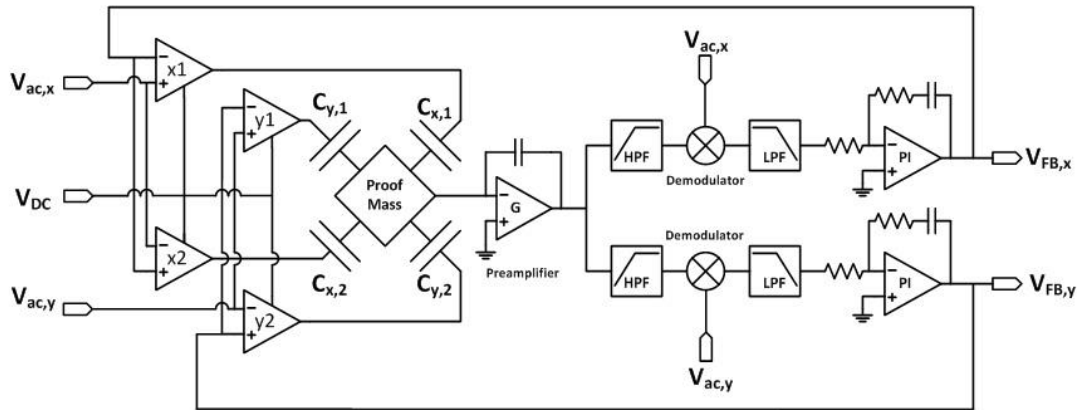


Figure 6.1: The block diagram of the two-axis accelerometer using the proposed accelerometer readout circuit.

In Figure 6.1,  $C_{x,1-2}$  and  $C_{y,1-2}$  are the differential electrode capacitances sensitive in x- and y-axis respectively. The electronic blocks for the readout in each axis is exactly the same with the proposed readout circuit with a common pre-amplifier for both axes.

One source of cross-axis sensitivity is a result of device topology, and it can be easily visualized by observing the sensing element model as given in Figure 6.1: Considering an acceleration in x-axis is applied, the capacitances of the x-axis electrodes will change following the basics behind the varying-gap capacitor. However, it can also be seen that the y-axis electrode capacitances change as well due to the varying-overlap type of sensitivity of y-axis electrodes in response to accelerations in x-axis. Considering the proposed readout circuit is operated in closed-loop, this cross coupling

source is not an issue to be concerned about. Because by closed-loop operation, the proof mass virtually never moves its rest position at the center.

As it can be seen in the block diagram, the readout currents of both axes are transferred to the pre-amplifier on the same net. The frequency splitting property of this topology gets important because of this issue. By applying carrier signals  $V_{ac,x}$  and  $V_{ac,y}$  at different frequencies to the capacitances of the different axes, the readout currents flowing towards the front-end electronics are separated in terms of frequency. The output of the front-end electronics (output of the high-pass filters) are the same for both readout loops. However, by demodulation at the corresponding carrier signal frequency, the readout voltages that are not related with the axis of interest are filtered out. Eventually at the output of the low-pass filters of each axis readout loop, only the data associated with the corresponding axis can be obtained. The effect of demodulation can be observed using the equations presented in Chapter 2, Section 2.2.2. By using these equations, it can also be observed that increasing the frequency difference between the two carrier signals results in an increase in the separation quality, and thus a reduction in the cross-axis sensitivity.

This readout concept is proven to work with measurement results. The sensing element used in the scope of this thesis had already readily available y-axis electrodes as shown in Chapter 2, Figure 2x1. This electrode set of the sensing element is utilized to implement the demonstrated two-axis accelerometer. During the tests, the same readout circuit parameters are used as in the single-axis case with only a different electrical configuration parameters which are the proof mass voltage, carrier signal amplitude and frequency. Note that 110 and 120 kHz carrier signals are used for the two axes. In Figure 6.2, the data collected simultaneously from the two-axis accelerometer during a full circular rotation is demonstrated. Note that during this rotation, xy-plane of the accelerometer is placed vertically with respect to ground and it is rotated along z-axis.

In Figure 6.2 the scale factors of each axis can be observed. Note that it is slightly different than the single-axis case because of different electrical configuration parameters.

The cross-axis sensitivity of both axes are measured below 1.5 % of the scale factor value as described in detail in [43].

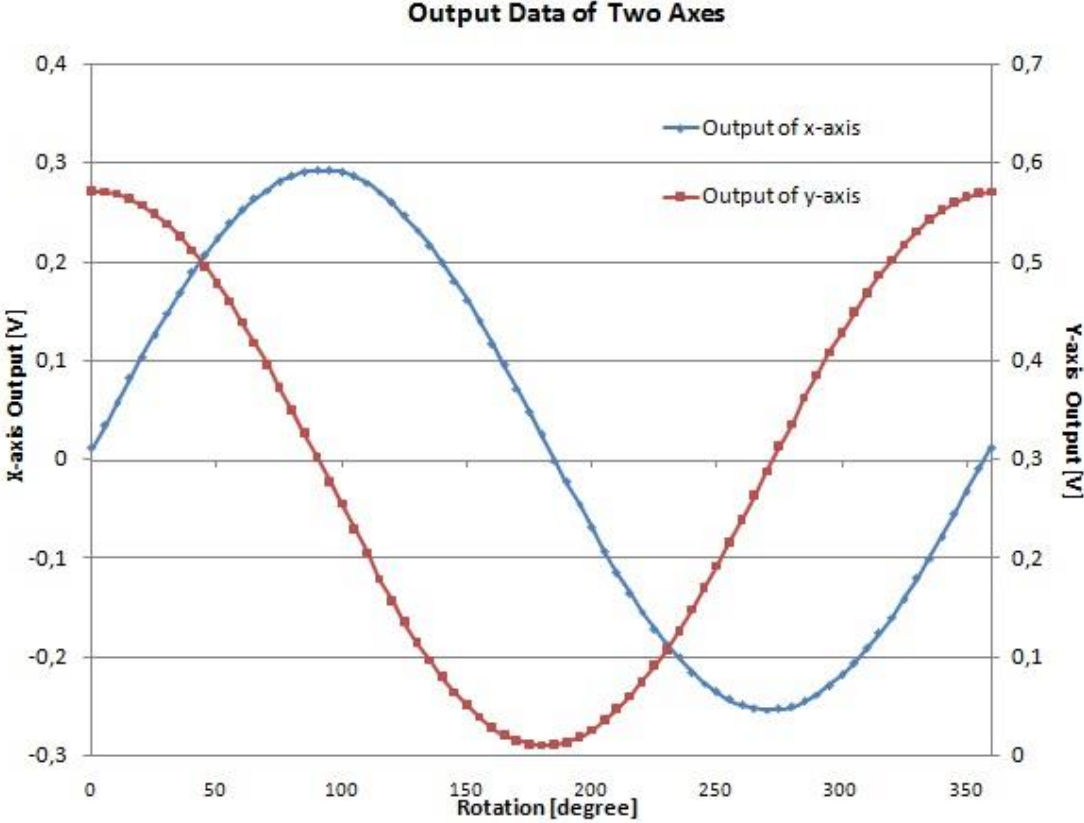


Figure 6.2: The data collected from the two-axis accelerometer through a full circular rotation where the xy-plane of the accelerometer is set vertical to the ground and the rotation is along z-axis [43].

**6.2. An Out-of-Plane Accelerometer and a New Concept of Hybrid Electrodes**

The demand for the multi-axis accelerometers is highlighted in the previous sub-section. In such systems, apart from sensing the acceleration in either lateral axis, sensing in out-of-plane (z-axis) brings out additional challenges due to the nature of the micro-fabrication. These challenges include the placement of differential sensing electrodes both below and above the suspended proof mass in order to maintain system linearity, [46], [47]; or fabrication of asymmetrical sensor structures, [48], [49], [50],

in order to achieve differential acceleration sensing in z-axis. However, all such methods require extra process steps, and therefore, additional fabrication difficulties and costs. Moreover, such steps are usually harder to deal with compared to the difficulties related with lateral sensing electrode sets because of the planar topology of the capacitive accelerometers incorporating comb fingers.

The sensing element used in scope of this thesis has comb finger type lateral electrodes for sensing in x- and y-axis. Additionally, it has an electrode placed beneath the proof mass forming a varying gap capacitor in z-axis. Either set of lateral electrodes combined with the z-electrode in order to mimic a set of differential capacitors sensitive along z-axis. However, the sensitivity of the lateral electrode capacitances are indecisive along z-axis while the proof mass in in rest position. As a solution to this problem and subsequently to be able to use the two different types of electrodes for differential sensing, the proof mass is intentionally pulled down towards the z-electrode. This way, the lateral comb finger type electrodes can be used as *varying overlap* type of variable capacitances with a well-defined sensitivity. In Figure 6.3, a diagram demonstrating the cross-sectional view of the sensing element during this kind of an operation is given.

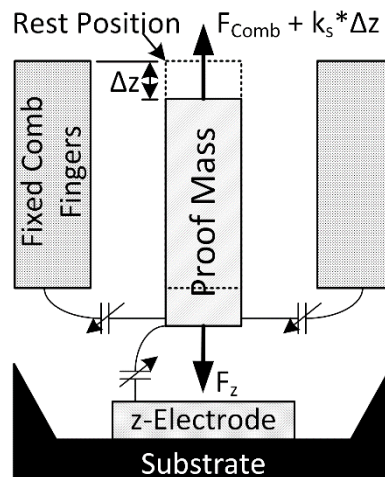


Figure 6.3: The cross-sectional view of the sensing element where the lateral comb type electrodes are used to form a differential capacitance pair with the vertical z-electrode placed beneath the proof mass [44].

As it can be seen in Figure 6.3, the comb fingers attached to the proof mass has a sensitivity along z-axis, behaving as a varying overlap type of electrode capacitor, and in combination with the z-electrode, a pair of differential electrodes can be electrically created by pulling the proof mass down slightly. This pulling force is intuitively created by the proof mass voltage applied on the sensing element. Since at rest position the comb fingers exert zero electrostatic force on the proof mass along z-axis, the proof mass is bound to be pulled down by the z-electrode until the force balance between the spring loading in z-axis, the electrostatic force by comb electrode, and the electrostatic force by the z-electrode is achieved. In Figure 6.4, the circuit diagram demonstrating the application of this method using AFFRO is demonstrated.

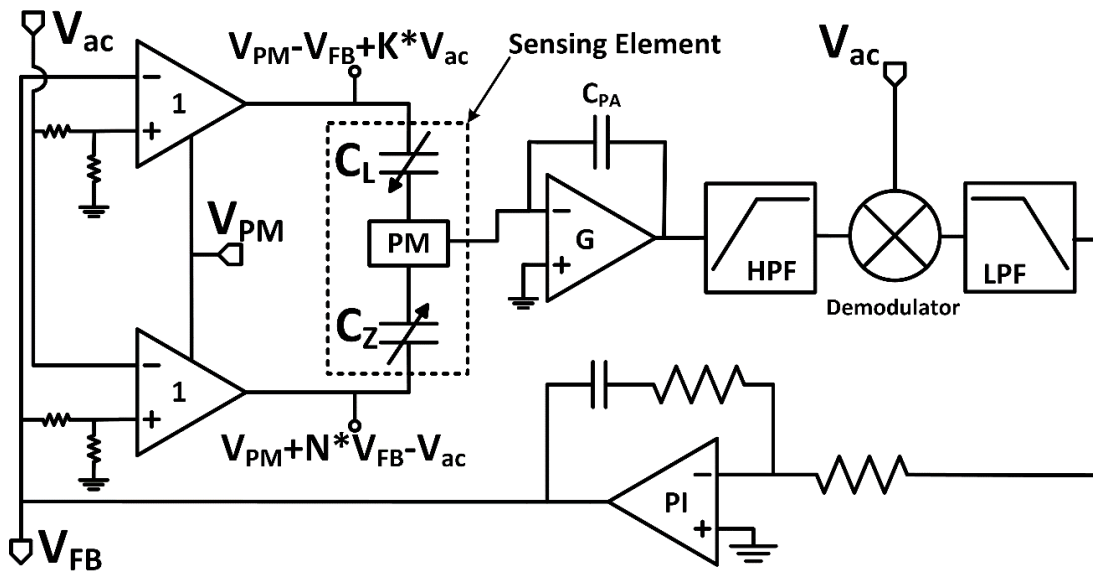


Figure 6.4: The use of AFFRO with the hybrid electrodes concept to sense acceleration in out-of-plane axis [44].

There is one major problem with this method: It is practically very hard to match both the capacitance values and the sensitivities of the two differential capacitances at the point where the mass is pulled down to (Q-point). Since what the AFFRO tries to do is to match the two differential capacitances' values by closed-loop operation, not being able to match them at the Q-point causes a high zero g off-set which is not desired. A high zero g off-set also causes the Q-point's position to change as well and might cause pull-in. Also the difference in the sensitivities of the two electrodes causes

non-linearity in the accelerometer response. This non-linearity can simply be observed by the force-equilibrium expressions given below.

$$F_z + ma = F_{comb} + k_s \Delta z \quad (6.1)$$

$$0.5 \frac{dC_z}{dz} (V_{PM} + V_{FB})^2 + ma = 0.5 \frac{dC_L}{dz} (V_{PM} - V_{FB})^2 + k_s \Delta z \quad (6.2)$$

$$ma = \frac{dC_L}{dz} V_{PM} V_{FB} - \frac{dC_z}{dz} V_{PM} V_{FB} + \overbrace{0.5 \left( \frac{dC_L}{dz} - \frac{dC_z}{dz} \right) V_{FB}^2}^{F_{nl}} + (\dots) \quad (6.3)$$

Normally, in order to ensure linear operation, the relation between the input acceleration, ‘ $a$ ’, and the output voltage, ‘ $V_{FB}$ ’, should be correlated with each other with multiplication by a *constant* value. However, as shown in Equation 6.3, the force contribution  $F_{nl}$  is a source of non-linearity for the case where the two differential capacitances has different sensitivities.

At the desired Q-point, the comb electrode of the sensor has a higher capacitance but a lower sensitivity compared to the vertical z-electrode. In order to compensate for these differences, carrier signal applied on the comb electrode is attenuated by a factor of ‘ $K$ ’, while the feedback voltage applied on the vertical electrode is attenuated by a factor of ‘ $N$ ’ as shown in Figure 6.4. These attenuations are achieved through resistive division in the corresponding inputs of the instrumentation amplifiers. This way, the AC readout currents flowing through both electrodes at the Q-point are equalized and the circuit is tricked as if the two capacitors are of equal size. Similarly, the sensitivity difference between the two electrodes are compensated by simply applying less feedback voltage to one electrode compared to the other. Attenuation factors can be formulated as below.

$$K = \frac{C_{z,Q}}{C_{L,Q}} \quad (6.4)$$

$$N = \frac{dC_{L,Q}/dz}{dC_{L,z}/dz} \quad (6.5)$$

The proposed method for realizing an out-of-plane accelerometer is implemented and its operation is verified using AFFRO. In Figure 6.5, the results of the linearity

measurement test conducted on this accelerometer is demonstrated. Additionally, the noise performance of this out-of-plane accelerometer is shown in Figure 6.6.

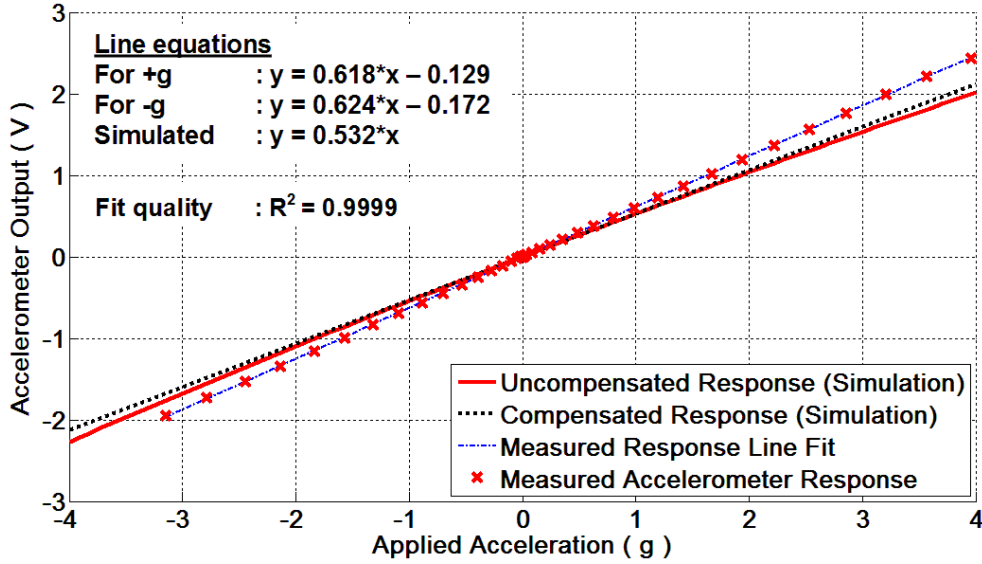


Figure 6.5: The linearity performance of the implemented out-of-plane accelerometer presented along the simulation results.

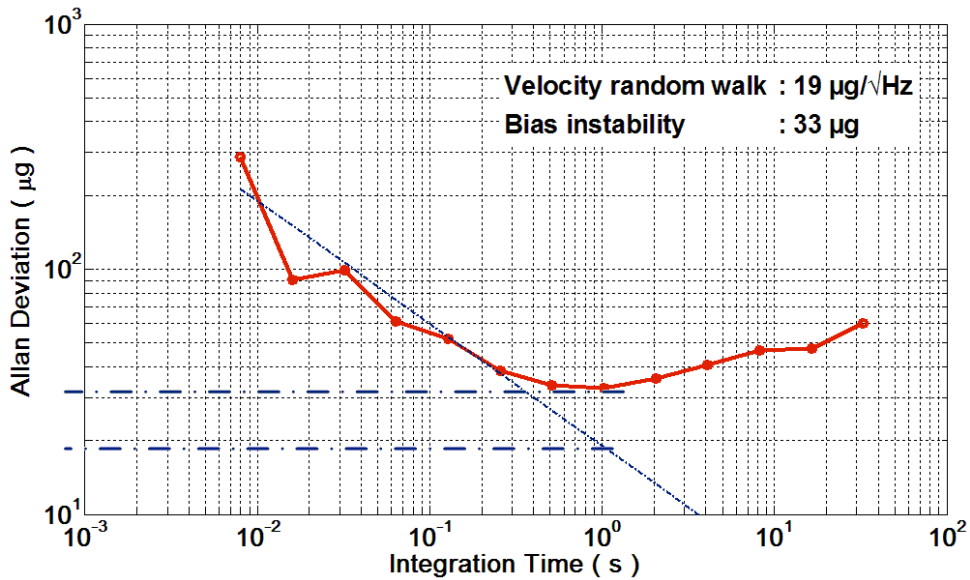


Figure 6.6: The noise performance of the implemented out-of-plane accelerometer.

### **6.3. Summary**

In this chapter, two different multi-axis accelerometer applications using the proposed analog accelerometer readout circuit are presented as a demonstration of the of the adaptability of the circuit. Additionally, a novel method, in which the proposed readout circuit is used for out-of-plane acceleration sensing, is presented. It is shown that that by using such a sensing approach, differential acceleration sensing in z-axis can be achieved using a sensing element with less mechanical design and fabrication complexities.

The functionality of the proposed applications are demonstrated in this chapter as well. Even though only the measurements which are directly related with the corresponding application is presented, it should be noted that the accelerometer performance can be estimated prior to implementation using the behavioral models created for the single-axis accelerometer. The accuracy of the models are verified by the measurement results in single-axis, it can be said that they will also work for these two applications since besides the structural differences between the systems, the equations identifying operation of the systems are the same in all three cases: single-axis, two-axis, and z-axis.



## CHAPTER 7

### CONCLUSIONS AND FUTURE WORK

A high performance closed-loop analog readout circuit is presented in this thesis. The detailed analysis of the design, implementation, and the test results of the proposed accelerometer are demonstrated in the previous chapters. Moreover, the adaptability of the readout circuit is demonstrated with two multi-axis accelerometer applications in Chapter 6. The conclusions of this study are summarized in the following list:

- The proposed feedback topology, which enables the readout and feedback tasks to be carried out simultaneously using only one set of differential electrodes, has been proven functional. This topology is not only functional, but also helps to separate the feedback voltage from the front-end electronics almost completely by capacitive decoupling. This way, the risk of saturation in the front-end electronics due to the feedback voltage is completely eliminated.
- By using the proposed continuous time interface, the residual motions of the proof mass are kept at a minimum thanks to the low-pass filter behavior of the sensing element. Moreover, since the feedback and readout signals are continuous time signals, the need for switching between tasks or digitization of the feedback signal has been avoided. Eventually, the impulse type voltages and currents affecting the sensing element have also been avoided, which yet again reduces the mass residual motions and also reduces the circuit complexity.
- It is seen that the operation range and the scale factor of the accelerometer can be tuned by only manipulating the proof mass voltage in such readout circuit. By reducing the proof mass voltage, the scale factor of the system can be increased and the operation range can be reduced. Even though such action

causes the overall loop gain to reduce and degrade the noise performance, the loop gain can be compensated back to the same level by increasing the amplitude of the carrier signal. Such versatility enables the use of the proposed accelerometer in different applications with different range-related requirements without making any changes in the sensing element.

- Three different models for the proposed accelerometer are created. First of these models was used to simulate the complete system in time-domain using ideal components. The second one is again created using ideal components but it was created for frequency-domain simulations, and the investigation of the loop stability. The last model is an electrical behavioral model, and non-ideal electrical component models as supplied by the IC manufacturers have been used in order to both simulate the overall system in time-domain and to verify that IC non-idealities did not cause any errors in the accelerometer operation. The functionality and the accuracy of all three models were verified with respect to each other and the measurement results. The simplicity of the proposed readout circuit was also a beneficial factor for creation of high-accuracy simulation models.
- The white noise level of the readout circuit is kept below  $10 \mu\text{g}/\sqrt{\text{Hz}}$  as desired. The measured noise performance is slightly above the estimated noise performance. This is mostly due to the simplifications made in the formulas, neglected noise sources, and external sources. Such difference was already expected, and it can be said that the assumptions made during the performance estimation steps are appropriate.
- The linearity performance of the proposed accelerometer matched the expectations eliminating the non-linear behavior of the sensing element itself. This verifies the closed-loop operation is achieved, and the proof mass's motion is restrained at its rest position as aimed.
- The multi-axis compatibility of the proposed readout circuit is verified with the measurement results in which acceleration is sensed in two axes simultaneously with a single-mass type sensing element. Moreover, a new concept for detecting out-of-plane acceleration is introduced and implemented using the proposed readout circuit.

The study presented in this thesis showed that proposed readout circuit can be used to realize a versatile, high performance accelerometer with very low circuit and design complexity as demonstrated in detail in the previous chapters with calculations, simulation models, and measurement results. With further research, both the performance and the applicability of the proposed accelerometer can be improved. Some of this possible further work are listed below:

- One of the main concerns related with the closed-loop accelerometers is the shock recovery. If the accelerometer cannot recover itself from a shock, its applicability is reduced tremendously. Even though the readout circuit is insensitive high acceleration inputs and does not get saturated with shock, overall system should be tested in a controlled environment for shock response characterization. It might ultimately be necessary to use shock bumpers in the sensing element which would prevent the electrodes to short circuit under the effects of high acceleration inputs.
- During the implementation of the accelerometer in this study, a hybrid platform package is used as demonstrated in Chapter 5. Such circuit platform offers a very good accelerometer performance since the circuit is completely buried inside a Faraday's cage and very high quality off-the-shelf integrated circuits can be used during the implementation. However, manufacturing such an accelerometer can be considered expensive in terms of both costs and time. Manufacturing cost can significantly be reduced by designing an application specific integrated circuit (ASIC) in case the proposed accelerometer is intended to be manufactured in volume. The drawback of such an ASIC would be the reduction in the adaptability of the readout circuit, since an ASIC would most probably be designed for a specific range of sensing element parameters. Another alternative for the implementation of the proposed circuit is to design a small scale PCB using active and passive components of preferably larger packages. Even though this would not reduce the fabrication costs of the accelerometer, the effort required to manufacture each readout circuit can be reduced significantly. Moreover, such circuit would be much more robust and can be used over and over with different sensors with minimal risk of damaging the circuit. With a PCB incorporating a well-designed routing and shielding,

the performance of the hybrid platform package can be repeated without significant degradation, and the readout circuit would still offer a good plug-and-play platform for research and characterization of different types of sensing elements.

- The proof mass voltage is fed to the accelerometer directly through the power supply. If this voltage is generated through a low-drift and low-noise voltage reference, the bias instability and the velocity random walk performances of the accelerometer can be improved.
- The temperature sensitivity of the proposed accelerometer is not characterized in scope of this thesis. When it comes to the applicability of this sensor in real life, temperature sensitivity of the implemented system bears a critical role, and it should definitely be characterized and tried to be compensated. The accelerometer output bias change with respect to the temperature variations can be compensated by manipulating the non-inverting input bias of the low-pass filter in the loop according to the environment temperature. Given that a linear relation between the accelerometer output bias and the environment temperature is existent, this compensation can easily be done using a linear temperature sensor and a simple interface circuit.

## REFERENCES

- [1] J. Bouchaud, "High Value MEMS Market Overview," 12 May 2011. [Online]. Available: [http://cmp.imag.fr/conferences/dtip/dtip2011/ppt/DTIP\\_high-valueMEMS\\_iSuppli\\_handout.pdf](http://cmp.imag.fr/conferences/dtip/dtip2011/ppt/DTIP_high-valueMEMS_iSuppli_handout.pdf). [Accessed 29 August 2015].
- [2] J. Eloy, "MEMS Industry Evolution: From Devices to Function," 2010. [Online]. Available: [http://semiconwest.org/sites/semiconwest.org/files/JC%20Eloy.Yole\\_.pdf](http://semiconwest.org/sites/semiconwest.org/files/JC%20Eloy.Yole_.pdf). [Accessed 29 August 2015].
- [3] K. Lightman, "MEMS and Sensor Trends," 2013. [Online]. Available: [http://c.ymcdn.com/sites/www.memindustrygroup.org/resource/collection/A1DAAF83-11BC-4D42-A98F-BF250C325EE8/MEMS\\_and\\_Sensor\\_Trends\\_-\\_Smaller\\_Faster\\_and\\_Available\\_to\\_the\\_Mass\\_Market.pdf](http://c.ymcdn.com/sites/www.memindustrygroup.org/resource/collection/A1DAAF83-11BC-4D42-A98F-BF250C325EE8/MEMS_and_Sensor_Trends_-_Smaller_Faster_and_Available_to_the_Mass_Market.pdf). [Accessed 29 August 2015].
- [4] Yole Development, "MEMS Markets Status of the MEMS Industry 2015," 2015. [Online]. Available: [http://www.i-micronews.com/images/Flyers/MEMS/Yole\\_Status\\_of\\_the\\_MEMS\\_Industry\\_April\\_2015\\_web.pdf](http://www.i-micronews.com/images/Flyers/MEMS/Yole_Status_of_the_MEMS_Industry_April_2015_web.pdf). [Accessed 29 August 2015].
- [5] IEEE Aerospace and Electronic Systems Society, "IEEE Standard for Inertial Sensor Terminology Std 528-2001," IEEE, 2001.
- [6] ST Microelectronics, "High-performance ultra-low-power 3-axis accelerometer with digital output for industrial applications," in *IIS328DQ Technical Datasheet*, 2015.
- [7] Y. Dong, P. Zwahlen, A. M. Nguyen and J. M. Rudolf, "High Performance Inertial Navigation Grade Sigma-Delta MEMS Accelerometer," in *IEEE/ION Position Location and Navigation Symposium (PLANS)*, Indian Wells, 2010.
- [8] Analog Devices Incorporated, "Precision  $\pm 5$  g, Dual Axis, High Temperature iMEMS Accelerometer," in *ADXL206 Technical Datasheet*, 2011.
- [9] S. W. Yoon, N. Yazdi, J. Chae, N. C. Perkins and K. Najafi, "Shock Protection Using Integrated Nonlinear Spring Shock Stops," in *19th IEEE International Conference on Micro Electro Mechanical Systems (MEMS 2006)*, Istanbul, 2006.

- [10] N. Yazdi, F. Ayazi and K. Najafi, "Micromachined Inertial Sensors," *Proceedings of the IEEE*, vol. 86, no. 8, pp. 1640-1659, August 1998.
- [11] J. Chae, H. Kùlah and K. Najafi, "A Monolithic Three-Axis Micro-g Micromachined Silicon Capacitive Accelerometer," *Journal of Microelectromechanical Systems*, vol. 14, no. 2, pp. 235-242, April 2015.
- [12] J. Wu, G. K. Fedder and R. Carley, "A Low-Noise Low-Offset Capacitive Sensing Amplifier for a 50- $\mu\text{g}/\sqrt{\text{Hz}}$  Monolithic CMOS MEMS Accelerometer," *IEEE Journal of Solid-State Circuits*, vol. 39, no. 5, pp. 722-730, May 2004.
- [13] C. Lu, M. Lemkin and B. E. Boser, "A Monolithic Surface Micromachined Accelerometer with Digital Output," *IEEE Journal of Solid-State Circuits*, vol. 30, no. 12, pp. 1367-1373, December 2012.
- [14] M. A. Lemkin, M. A. Ortiz, N. Wongkomet and B. E. Boser, "A 3-axis Force Balanced Accelerometer Using a Single Single Proof-Mass," in *9th International Conference on Solid-State Sensors and Actuators (Transducers '97)*, Chicago, 1997.
- [15] O. Aydın and T. Akın, "A Bulk-Micromachined Fully-Differential MEMS Accelerometer with Interdigitated Fingers," in *IEEE Sensors Conference*, Taipei, 2012.
- [16] S. Tez, U. Aykutlut and T. Akın, "A Bulk-Micromachined Three-Axis Capacitive MEMS Accelerometer on a Single Die," *Journal of Microelectromechanical Systems*, vol. PP, no. 99, p. 1, 7 August 2015.
- [17] A. Selvakumar, F. Ayazi and K. Najafi, "A High Sensitivity z-Axis Torsional Silicon Accelerometer," in *International Electron Devices Meeting (IEDM '96)*, San Francisco, 1996.
- [18] Colibrys, "High Performance Open Loop Accelerometer for Space Applications," Colibrys, [Online]. Available: <https://escies.org/download/webDocumentFile?id=59863>. [Accessed 29 August 2015].
- [19] J. Wu and R. Carley, "Electromechanical  $\Delta\Sigma$  Modulation with High-Q Micromechanical Accelerometers and Pulse Density Modulated Force Feedback," *IEEE Transactions on Circuits and Systems*, vol. 53, no. 2, pp. 274-287, February 2006.
- [20] R. Kepenek, İ. E. Ocak, H. Kùlah and T. Akın, "A  $\mu\text{g}$  Resolution Microaccelerometer System with a Second-Order  $\Sigma\text{-}\Delta$  Readout Circuitry," in *PhD Research in Microelectronics and Electronics (PRIME 2008)*, Istanbul, 2008.
- [21] L. Aaltonen, P. Rahikkala, M. Saukoski and K. Halonen, "Continuous Time Interface for a  $\pm 1.5$  g Closed-Loop Accelerometer," in *IEEE International*

*Conference on Integrated Circuit Design and Technology (ICICDT '07)*, Austin, 2007.

- [22] M. Yüçetaş, A. Kalanti, J. Salomaa, L. Aaltonen and K. Halonen, "An Analog Closed-Loop SC Accelerometer Interface for a Capacitive High-Q Sensor Element," in *Conference on Ph.D. Research in Microelectronics and Electronics (PRIME '10)*, Berlin, 2010.
- [23] Y. Terzioğlu, S. E. Alper, K. Azgin and T. Akın, "A Capacitive MEMS Accelerometer Readout with Concurrent Detection and Feedback Using Discrete Components," in *IEEE/ION Position, Location and Navigation Symposium (PLANS 2014)*, Monterey, 2014.
- [24] T. L. Grigorie, "The Matlab/Simulink Modeling and Numerical Simulation of an Analogue Capacitive Micro-Accelerometer. Part 1: Open Loop," in *International Conference on Perspective Technologies and Methods in MEMS Design (MEMSTECH 2008)*, Polyana, 2008.
- [25] "Mathematical Modeling and Numerical Simulation of the Detection Unit in a Miniaturized Capacitive Accelerometer," in *International Conference on Applied and Theoretical Electricity (ICATE 2012)*, Craiova, 2012.
- [26] A. Soma and A. Ballestra, "Design of Test Structures for Reduced Order Modeling of the Squeeze Film Damping in MEMS," in *International Semiconductor Conference*, Sinaia, 2006.
- [27] Z. Zhou and X. Wang, "Analysis of Squeeze-Film Air Damping of Thick Perforated Plate in MEMS Device," in *IEEE International Conference on Nano/Micro Engineered and Molecular Systems (NEMS 2011)*, Kaohsiung, 2011.
- [28] S. Sönmezoğlu, "A High Performance Automatic Mode-Matched Gyroscope," in *M.Sc. Thesis*, Middle East Technical University, September 2012.
- [29] Analog Devices Incorporated, "Op Amp Applications Handbook," *Technical Handbook*, pp. 257-283, 2005.
- [30] M. E. T. University, "Capacitive Sensors," *EE610 Lecture Notes*, pp. 8-13.
- [31] K. J. Astrom and T. Haggund, "Revisiting the Ziegler–Nichols Step Response Method for PID Control," *Journal of Process Control*, vol. 14, no. 6, pp. 635-650, 2004.
- [32] T. Haggund and K. J. Astrom, "Revisiting the Ziegler-Nichols Tuning Rules for PI Control - Part II The Frequency Response Method," *Asian Journal of Control*, vol. 6, no. 4, pp. 469-482, 2004.

- [33] Analog Devices Incorporated, "AD8605/AD8606/AD8608 Precision, Low Noise, CMOS, Rail-to-Rail, Input/Output Operational Amplifiers," *Technical Datasheet*, 2013.
- [34] Analog Devices Incorporated, "AD630 Balanced Modulator/Demodulator," *Technical Datasheet*, 2015.
- [35] Analog Devices Incorporated, "AD8628/AD8629/AD8630 Zero-Drift, Single-Supply, Rail-to-Rail Input/Output Operational Amplifier," *Technical Datasheet*, 2014.
- [36] V. Michal, C. Prémont, G. Pillonet and N. Abouchi, "Single Active Element PID Controllers," in *20th International Conference on Radioelektronika (RADIOELEKTRONIKA 2010)*, Brno, 2010.
- [37] Analog Devices Incorporated, "AD8222 Precision, Dual-Channel Instrumentation Amplifier," *Technical Datasheet*, 2010.
- [38] J. H. Mikkelsen, "LTspice - An Introduction," 12 October 2005. [Online]. Available: [http://kom.aau.dk/~hmi/Teaching/LTspice/restrict/LTspicedoc/LTspice\\_guide.pdf](http://kom.aau.dk/~hmi/Teaching/LTspice/restrict/LTspicedoc/LTspice_guide.pdf). [Accessed 29 August 2015].
- [39] Linear Technology, "LTspice IV User Manual," [Online]. Available: <http://ece.colorado.edu/~mathys/ecen1400/pdf/scad3.pdf>. [Accessed 29 August 2015].
- [40] Analog Devices Incorporated, "TMP35/TMP36/TMP37 Low Voltage Temperature Sensor," *Technical Datasheet*, 2015.
- [41] V. Vukmirica, I. Trajkovski and N. Asanovic, "Two Methods for the Determination of Inertial Sensor Parameters," *Scientific Technical Review*, vol. 60, no. 3-4, pp. 27-33, 2010.
- [42] N. El-Sheimy, H. Hou and X. Niu, "Analysis and Modelling of Inertial Sensors Using Allan Variance," *IEEE Transactions on Instrumentation and Measurement*, vol. 57, no. 1, pp. 140-149, 2008.
- [43] T. Köse, Y. Terzioğlu, K. Azgın and T. Akın, "A Single Mass Two-Axis Capacitive MEMS Accelerometer with Force Rebalance," in *IEEE International Symposium on Inertial Sensors and Systems (ISISS 2015)*, 2015.
- [44] Y. Terzioğlu, T. Köse, K. Azgın and T. Akın, "A Simple Out-of-Plane Capacitive MEMS Accelerometer Utilizing Lateral and Vertical Electrodes for Differential Sensing," *Submitted for Publication*, 2015.
- [45] H. Tavakoli and E. A. Sani, "A New Method for Eliminating Cross Axis Sensitivity in Two Axis Capacitive Micromachined Accelerometers," in *The*

*21st Iranian Conference on Electrical Engineering (CCECE 2013)*, Mashhad, 2013.

- [46] S. Tez and T. Akm, "Fabrication of a Sandwich Type Three Axis," in *IEEE Sensors Conference*, Baltimore, 2013.
- [47] F. Han, B. Sun, L. Li and G. Ma, "A Sensitive Three-Axis Micromachined Accelerometer Based on an Electrostatically Suspended Proof Mass," in *IEEE Sensors Conference*, Baltimore, 2013.
- [48] J. M. Darmanin, I. Grech, J. Micallef, E. Gatt, O. Casha and A. Briffa, "Design Consideration for Three-axis MEMS Accelerometers Using an Aysmmetric Proof Mass," in *IEEE EUROCON Conference*, Zagreb, 2013.
- [49] J. Wang, Z. Yang and G. Yan, "A Silicon-on-Glass Z-Axis Accelerometer with Vertical Sensing Comb Capacitors," in *The 7th IEEE International Conference on Nano/Micro Engineered and Molecular Systems (NEMS 2012)*, Kyoto, 2012.
- [50] T. Tsuchiya and H. Funabashi, "A Z-Axis Differential Capacitive SOI Accelerometer with Vertical Comb Electrodes," in *The 17th IEEE International Conference on Micro Electro Mechanical Systems (MEMS 2004)*, Maastricht, 2004.